Solid State Ionics 430 (2025) 116995

Contents lists available at ScienceDirect

Solid State Ionics

journal homepage: www.elsevier.com/locate/ssi

Ionic nanoarchitectonics for electronic information devices[☆]

Kazuya Terabe [a,*], Takashi Tsuchiya [a], Tohru Tsuruoka [a], Hirofumi Tanaka [b,c], Ilia Valov [d,e], James K. Gimzewski [f,g], Tsuyoshi Hasegawa [h]

[a] *Research Center for Materials Nanoarchitectonics (MANA), National Institute for Materials Science (NIMS), 1-1 Namiki, Tsukuba, Ibaraki 305-0044, Japan*
[b] *Research Center for Neuromorphic AI Hardware, Kyushu Institute of Technology, 2-4 Hibikino, Wakamatsu, Kitakyushu 807-0805, Japan*
[c] *Graduate School of Life Science and Systems Engineering, 2-4 Hibikino, Wakamatsu, Kitakyushu 807-0805, Japan*
[d] *Research Centre Juelich, PGI-7, Wilhelm-Johnen-Str., 52425 Juleich, Germany*
[e] *Institute of Electrochemistry and Energy Systems, Bulgarian Academy of Sciences, acad. G. Bonchev str. 10, 1113 Sofia, Bulgaria*
[f] *Department of Chemistry and Biochemistry, University of California Los Angeles (UCLA), Los Angeles, CA 90095, USA*
[g] *California NanoSystems Institute, University of California Los Angeles (UCLA), Los Angeles, CA 90095, USA*
[h] *Faculty of Science and Engineering, Waseda University, 3-4-1 Okubo, Shinjuku-ku, Tokyo 169-8555, Japan*

ARTICLE INFO

Keywords:
Solid-state ionics
Ionic nanoarchitectonics
Atomic switch
Neuromorphic device
Artificial synapse
Physical reservoir
Nanoionics

ABSTRACT

Today's scientific and technological growth relies on rapid advances in electronic information technologies. Semiconductor devices such as transistors are essential to these technologies, and they are constantly being improved by being made smaller and more integrated. However, there is a concern that these improvements may slow down in the near future. Thus, creating new types of devices that can overcome the problems and/or enhance the capabilities of traditional semiconductor devices has become an important challenge. In particular, solid-state ionic devices can potentially meet this challenge. In this review, we describe the design of such devices using ionic nanoarchitectonics techniques that locally control ion conduction and electrochemical behavior in ion conductors and mixed conductors. In addition, we describe solid-state ionic devices developed for electronic information technology as well as the electrical, magnetic, optical, and brain-inspired neuromorphic functionalities of these devices.

1. Introduction

Electrical conduction in solids arises from the movement of charged particles in an applied electric field. The charged particles that move in a solid are called charge carriers and they include electrons, holes (vacancies left by electrons), ions, and vacancies (vacancies left by ions). Electronics is a field that studies phenomena associated with the movement of electrons and holes in solids and applies their properties to the operation of devices. In particular, electronic information equipment consists of electronic devices based on semiconductors, in which the charge carriers are electrons or holes. Solid-state ionics, on the other hand, is a field that studies phenomena associated with the movement of ions and vacancies in solids and applies their properties to the operation of devices [1]. Solid-state ionic devices, such as fuel cells and all-solid-state batteries, are widely used in environmental and energy equipment. There is also a type of material called a mixed conductor in which both electrons and ions move. Mixed conductors are used in the electrodes of fuel cells and solid-state batteries and in electrochemical sensors.

Today's electronic information technology depends heavily on semiconductor devices such as transistors. These devices enable the computing and memory functions that have improved every year by their being made smaller and more integrated - a trend known as Moore's Law. However, as process sizes have decreased to the nanoscale and even to the atomic scale, there is concern that the performance of semiconductor devices will slow down in the near future. This concern is due to the inherent limitations of miniaturization and the physical operation of conventional semiconductor devices and has motivated interest in creating new devices that can be used in future electronic information technology. Here, solid-state ionic devices, which exploit the movement of ions in solids, may be potentially useful. These devices work on the basis of completely different principles than those of current semiconductor devices and are expected to not have their limitations.

In the 1970s, Sanyo Electric Co., Ltd. developed electrochemical

---

[☆] This article is part of a Special issue entitled: 'Solid State Ionics 100' published in Solid State Ionics.

[*] Corresponding author.
E-mail address: TERABE.Kazuya@nims.go.jp (K. Terabe).

https://doi.org/10.1016/j.ssi.2025.116995
Received 14 May 2025; Received in revised form 24 July 2025; Accepted 5 August 2025

devices known as “memoriods” that used solid-state ionics technology to store moving ions as electrical potential [2,3]. They were used as timers in portable radios. However, as semiconductor devices improved, these ionic devices were phased out because they were large and slow, requiring many ions to move during use. Recent advances in nanotechnology have overcome these limitations by making it possible to control the movement of ions at the nanoscale. [4]. As a result, nanoscale solid-state ionic devices (nanoionic devices) have re-emerged as a new generation of electronic information devices. This resurgence was triggered by the invention of nanoionic-based atomic switches and other resistive switches that work by controlling ion transport and electrochemical reactions at the nanoscale [5–8]. Many resistive switches operate by causing nanoscale conductive filaments to form and disappear through the transport of metal or oxide ions and redox reactions in response to the application of a voltage [9,10]. Unlike the volatile resistive switching operation of semiconductor transistors, these resistive switches exhibit non-volatile switching operation, making them promising for low-power non-volatile memory applications. Inspired by the invention of these switches, researchers have started to develop various solid-state ionics based electronic information devices with diverse functions. These developments involve skillfully exploiting the properties arising from local ion transport and electrochemical phenomena in various ion conducting materials and mixed conducting materials. In recent years, with the rapid development of artificial intelligence (AI) technology, the creation of neuromorphic devices that mimic brain functions has become active in the development of solid-state ionic devices in the field of electronic information [11]. Meanwhile, the development of AI and other functional devices using soft materials and liquids with ionic conductivity, is also advancing rapidly. Ionic liquids, which can utilize a variety of ion species, demonstrate excellent bonding properties at heterogeneous interfaces with functional materials, enabling the realization of efficient functional performance. Soft materials such as ion-conductive gels and polymers are expected to be used in flexible devices suitable for parts that move or deform. Further detailed information on the development of devices using these ion-conductive liquids, gels, and polymers can be found elsewhere [12–15].

This review begins with an introduction to ionic nanoarchitectonics, a technique that controls local ion transport and electrochemical reactions within solids. This technique is essential for creating solid-state ionic devices for enhancing electronic information technology. Building on this technique, we present the operating principles and performance evaluations of solid-state ionic devices, including non-volatile atomic switches, synapse devices, reservoir devices, and visual devices that mimic the functions of brain neurons. Furthermore, we also showcase numerous solid-state ionic devices with diverse properties and functions, including those exhibiting electrical, optical, and magnetic characteristics. Next, we will explain atomic layer deposition (ALD), a process that enables the production of high-quality, ultra-thin films essential for ionic nanoarchitectonics. Finally, we will discuss future prospects for solid-state ionic devices in the field of electronic information.

2. Solid-state ionic devices through ionic nanoarchitectonics

Solid-state ionic devices for electronic information technology work by controlling ion transport and electrochemical phenomena within solids on the nanoscale and atomic scale through the application of an external voltage [16]. By skillfully manipulating the structural, chemical and physical properties at interfaces between ion conductors and functional materials using ions of different sizes, valences and chemical affinities, researchers have created interesting properties and functions that cannot be achieved in electronic devices that operate by electron transport. Here, we will collectively refer to the techniques that exploit localized ion transport and electrochemical phenomena to create various properties and functions as ionic nanoarchitectonics [17,18]. Fig. 1 illustrates the structure and operating principle of a typical solid-state ionic device, where an ion conductor or mixed conductor material is sandwiched between electrodes. By applying an appropriate voltage of the correct polarity and magnitude between the electrodes, it is possible to control the transport of cations, anions or electrons within the ion conductor or mixed conductor, as well as the associated electrochemical phenomena. These electrochemical phenomena include the formation and disappearance of conductive metal filaments between electrodes (metal and functional materials) through redox reactions of metal ions, the formation and disappearance of electric double layers at the interface between ion conductors and electrodes arising from the movement of cations or anions, and the insertion and desorption of cations or anions with the electrode. By exploiting the various properties derived from these electrochemical phenomena, solid-state ionic devices can be created with functions and levels of performance unattainable in conventional electronics devices.

Ionic nanoarchitectonics techniques have been used to develop several ionic devices that exploit various electrochemical phenomena in their operation. Representative device structures and operating principles are illustrated in Fig. 2. The device shown in Fig. 2 (a) has a layered structure in which an ion conductor or mixed conductor is sandwiched between electrodes. When a voltage of positive or negative polarity is applied between the electrodes, ion transport and electrochemical reactions occur, resulting in the formation and disappearance of a nanoscale conductive filament within the ion conductor or mixed conductor. By controlling the formation and disappearance of the conductive filament, a resistance changing function is realized. This principle of operation has led to the development of quantized conductance (QC)

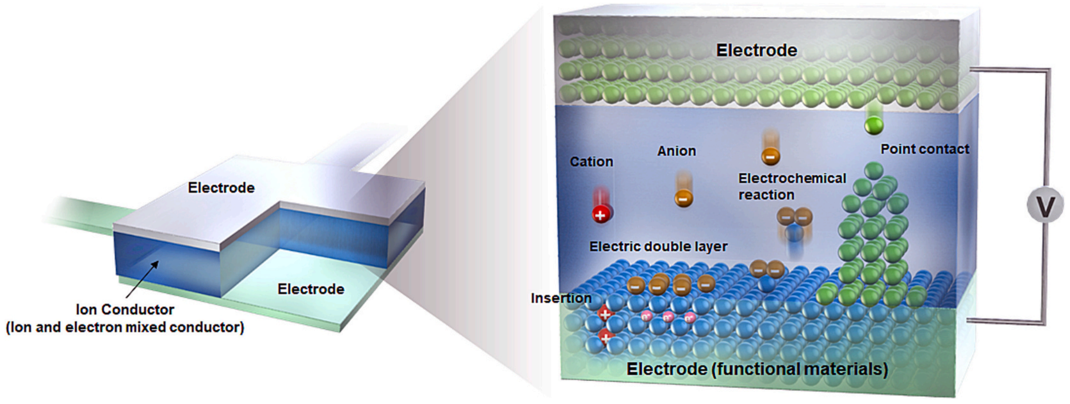

Fig. 1. Creation of solid-state ionic devices by using ionic nanoarchitectonics to create various properties and functions by exploiting localized ion transport and electrochemical phenomena. Reprinted with permission from Ref. 18. Copyright (2022) Wiley-VCH GmbH.

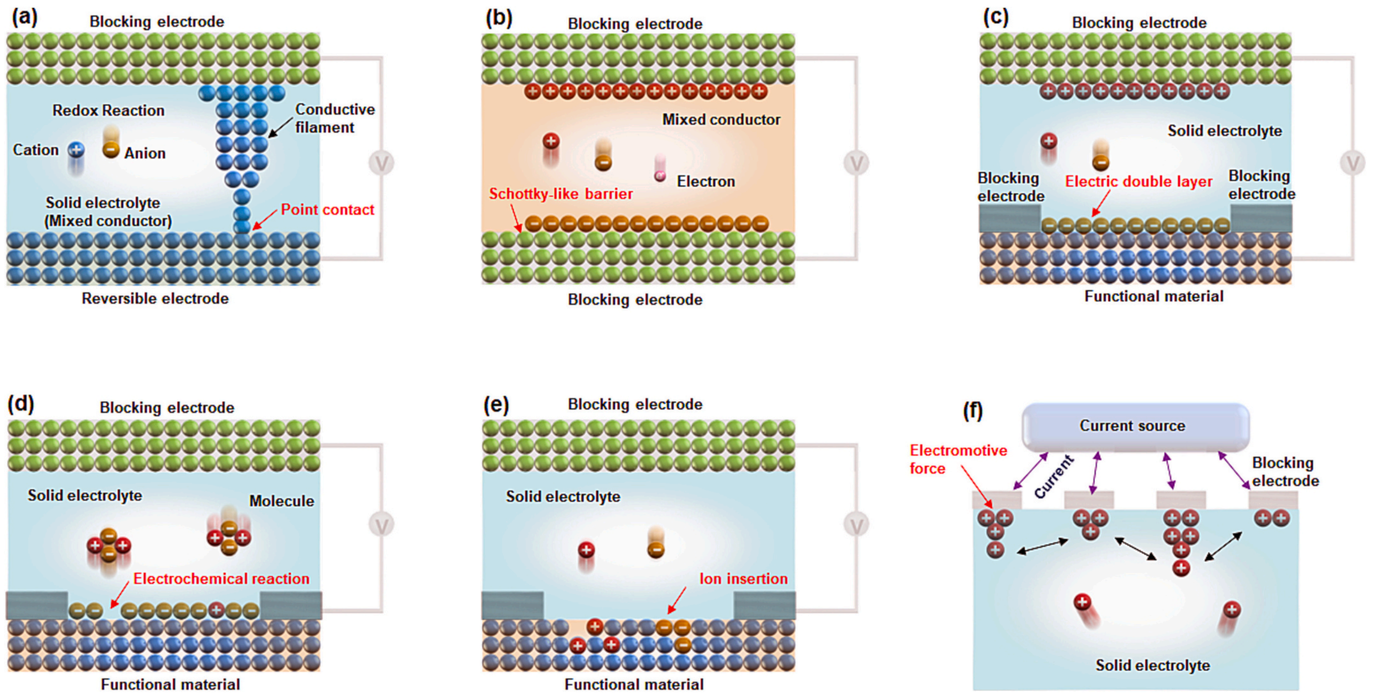

Fig. 2. Device structures and operating principles of ionic nanarchitectonics for controlling (a) a conductive filament, (b) a Schottky-like barrier, (c) an electronic double layer, (d) electrochemical reaction, (e) ion insertion, (f) electromotive force. Reprinted with permission from Ref. 18. Copyright (2022) Wiley-VCH GmbH.

atomic switches, non-volatile memory, artificial synapses, and radiation-resistant switches. The device shown in Fig. 2 (b) has a layered structure consisting of a mixed conductor and inert electrodes made from, e.g., platinum (Pt). When a voltage of positive or negative polarity is applied between the electrodes, positively or negatively charged ions in the mixed conductor move towards the interface with the electrode, thereby modulating the Schottky-like barrier formed at the interface. By exploiting this sort of modulation, a variable diode can be created that changes its rectifying characteristics. The device shown in Fig. 2 (c) has a transistor structure with three electrodes (gate, drain and source) and an ion conductor laminated on a functional material. By applying a voltage of positive or negative polarity to the gate electrode, ions in the ion conductor move, causing an electrical double layer to form or disappear at the interface with the functional material. The properties of the functional material, such as its electrical resistance, superconducting transition temperature, and capacitance, can be modulated by controlling the charge injected from the electrical double layer. The devices shown in Figs. 2 (d) and 2 (e) are also transistor structures, with three electrodes and an ion conductor stacked on a functional material. In the device shown in Fig. 2 (d), application of a gate voltage of appropriate polarity and magnitude induces an electrochemical reaction between the surface atoms of the functional material and ions moving through the ion conductor. By exploiting this electrochemical phenomenon, it is possible to desorb surface atoms of the functional material into the ion conductor or, conversely, to adsorb mobile ions from the ion conductor onto the surface of the functional material. In the device shown in Fig. 2 (e), the application of an appropriate gate voltage of the correct polarity and magnitude causes mobile ions to be inserted into or extracted from the functional material. The devices in Figs. 2 (c), (d) and (e) have the same three-terminal structure and operate by applying a gate voltage, but their functional materials, type of ion conductor, and the polarity and magnitude of the applied gate voltage differ. The device in Fig. 2 (f) has numerous inactive electrodes arranged on the surface of the ion conductor. By passing a current from a power source across the electrodes, the electrodes separate ions from the ion conductor material and the ions collect on their surfaces. This gives rise to a potential difference depending on the number of ions collected at each electrode, which in turn allows the collected ions to be counted by measuring the potential. This electrochemical phenomenon can be used to make memory functions for information learning and storage and decision-making functions. The solid-state ionic devices shown in Fig. 2 have layered structures similar to those of conventional semiconductor devices, so they can be fabricated with the same manufacturing processes and integrated with semiconductor devices. The remainder of this paper will describe representative examples of the ionic devices illustrated in Fig. 2 (a more comprehensive review can be found elsewhere [18]). In addition, Section 4.2.1 presents unique solid-state ionic devices with non-layered structures, for example, ionic devices that work by controlling ion transport and electrochemical reactions at many point contacts formed by nanoparticles or nanowires made from ion conductors or mixed conductors and deposited on a substrate.

3. Atomic switches

Atomic switches and resistive switches have been realized in the form of a layered structure sandwiching ion conductors or mixed conductors between electrodes, as shown in Fig. 2 (a). Both types of switch primarily use the transport of cations, such as metal ions, or anions, such as oxide ions, and redox reactions to control the formation and disappearance of conductive filaments [9,10]. In particular, atomic switches control the contact between the conductive filament and the electrode at the nanoscale or even at the atomic scale, where they exhibit not only resistance-change switching properties but also QC properties [19,20]. Fig. 3 shows two types of atomic switch that can be fabricated using silver sulfide (Ag_2S), a mixed conducting material in which silver (Ag) ions and electrons move, as the device material. The two device structures are a simple layered gapless type (Fig. 3(a)) and a gap type with a tunnel-current gap between the electrode and the mixed conducting material (Fig. 3(b)). The electrode materials for the gapless switch are Ag and Pt. The Ag electrode acts as a reversible electrode where redox reactions take place on its surface and also acts as a source of Ag ions for the Ag_2S. The Pt electrode is an inert electrode. By applying a suitable voltage of the correct polarity and magnitude between the Ag and Pt electrodes, Ag ions from the Ag_2S move towards the Pt electrode and

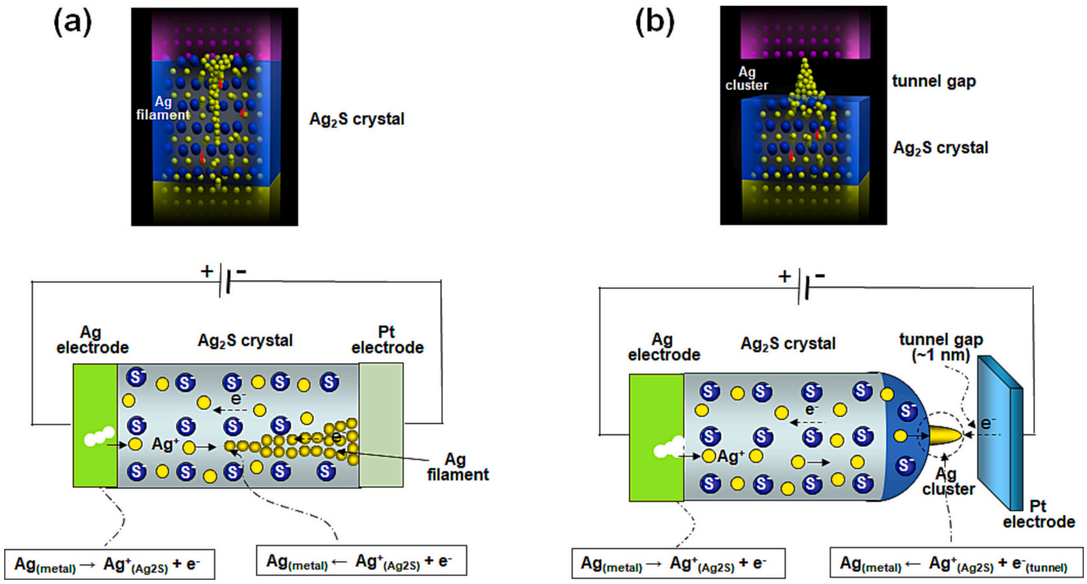

Fig. 3. Illustration of (a) gapless-type and (b) gap-type atomic switches based on silver sulfide (Ag_2S), a mixed conductivity material in which silver (Ag) ions and electrons move.

reduction reactions on the Pt electrode generate a cluster consisting of Ag atoms. Continued application of a voltage causes the Ag cluster to grow within the Ag_2S until it finally comes into contact with the Ag electrode. If the polarity of the applied voltage is then reversed, the oxidation reaction of the Ag filament breaks the contact between the Ag filament and the Ag electrode. By precisely controlling the applied voltage, the contact point between the Ag filament and the Ag electrode can be controlled from the nanoscale down to the atomic scale, thereby enabling not only on/off resistance-change switches but also QC switches with different electronic conduction states. The gap type of switch has a gap of about 1 nm between the Ag_2S and Pt electrodes. When a voltage is applied between the electrodes, a tunnel current flows through the gap. This tunnel current causes a cluster of Ag atoms to form within a very narrow region through the reduction reaction of the Ag ions in the Ag_2S. Therefore, the gap type of switch can relatively easily control the formation of atomic-scale point contact and the resulting QC.

The gap type of atomic switch was initially developed by using scanning tunneling microscopy (STM) in experiments to control ion motion and electrochemical reactions at the atomic scale [21]. Subsequent devices not requiring STM rested upon the use of microfabrication

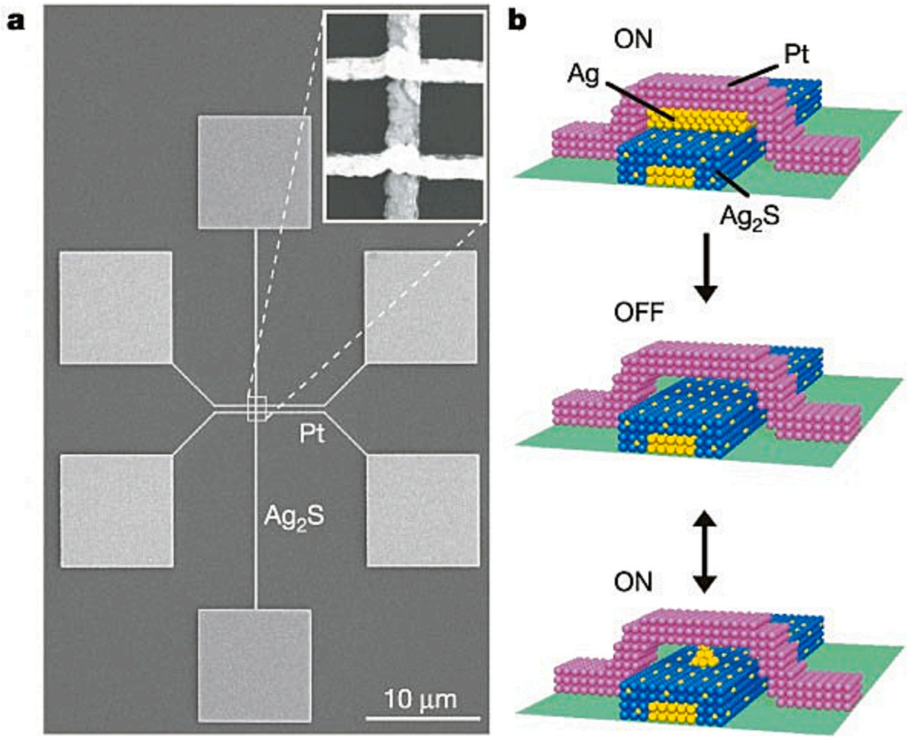

Fig. 4. (a) SEM image of a gap-type atomic switch. Two switches are formed at the crossing points of the 150-nm-wide Ag_2S wire and the two 100-nm-wide Pt wires. (b) Schematic diagrams of the atomic switch. As-formed switched-on state (top), switched-off state (middle) and switched-on state after the initial switching-off process (bottom). Reprinted with permission from Ref. 22. Copyright (2005) Springer Nature.

techniques commonly used to make semiconductor devices [22]. A scanning electron microscope (SEM) image of such an atomic switch is shown in Fig. 4 (a), and schematic diagrams of the device structure and its switching operation are shown in Fig. 4 (b). Here, a crossbar structure is formed by stacking Ag wire (electrode), Ag_2S wire, Ag film, and Pt wire (electrode), where the Ag film has a thickness of about 1 nm. When a positive voltage is applied to the Pt electrode, the Ag film undergoes an oxidation reaction, converting Ag ions, which dissolve into the Ag_2S matrix, and causing film to disappear. A 1-nm gap thus forms between the Pt electrode and the Ag_2S wires. In that gap, a tunnel current flows and the electrical resistance is in the range of several tens of mega-ohms (off-state). Next, a negative voltage is applied to the Pt electrode, and tunneling electrons flow from the Pt electrode to the Ag_2S wire. Above certain threshold current and voltage conditions, Ag ions within the Ag_2S are reduced and a cluster of Ag atoms grows on the surface. In addition, the Ag cluster forms a bridge between the Pt electrode and the Ag_2S wire, resulting in a significant reduction in electrical resistance to several kilo-ohms to tens of ohms (on-state). When the polarity of the voltage applied to the Pt electrode is reversed, the Ag bridge breaks and disappears by oxidation, with the Ag ions dissolving back into the Ag_2S. In other words, the gap type works by controlling the formation and disappearance of the Ag bridge in the tunnel current gap through the polarity of the applied voltage. In addition to Ag_2S, atomic switches using Cu_2S, a mixed conductor of Cu ions and electrons, have also been confirmed. For non-volatile memories, the speed of switching is a critical issue. The atomic switch works solely through the movement of ions from the nanoscale to the atomic scale, enabling sufficiently fast operation. Experiments have found that the speed increases exponentially with increasing applied voltage, with switching frequencies up to at least MHz order. Considering the speed of ion movement between crystal lattices, GHz-order operation is estimated to be possible.

Gapless atomic switches are currently being developed for integration into field programmable gate arrays (FPGAs) [23–25]. FPGAs are cutting-edge semiconductor chips that allow users to freely reconfigure circuits, and they are attracting attention for role in the development of technologies such as the Internet of Things (IoT) and AI. Conventional FPGAs use semiconductor transistors to switch circuits. By comparison, FPGAs based on atomic switches, which are smaller in area than transistors, would have a smaller chip area. In addition, because the wiring between logic cells would be shorter, it is estimated that the total power consumption of the chip could be reduced to about a quarter. Furthermore, the atomic switch is non-volatile, so no power is needed for it to retain data. Therefore, intermittently used equipment, such as IoT devices, can be turned off when not in use to reduce power consumption. In addition, while conventional semiconductor devices may experience data corruption when exposed to radiation, an atomic switch, which operates by generating and extinguishing the metal filament, does not exhibit such malfunctions. As a result, FPGAs equipped with atomic switches are suitable for use in artificial satellites that operate in outer space and are directly exposed to strong radiation in that environment [26]. Furthermore, FPGAs equipped with atomic switches show low performance drift over a wide temperature range from −55 °C to 150 °C and are highly resistant to supply voltage fluctuations [27]. Recently, there has been a growing demand for switches that can operate at extremely low temperatures for quantum computing circuits. Here, stable non-volatile resistance switching has been demonstrated at 4 K, making the atomic switch a promising candidate for controlling quantum bits at extremely low temperatures [28]. Table 1 shows a performance comparison between the gapless atomic switch (also known as nanobridge) and other types of switches, such as flash memory. In terms of operating voltage, durability, retention time, switching speed, and other characteristics, the atomic switch is equivalent to or superior to other switches [29].

3.1. *Quantized Conduction (QC) in Atomic Switches*

Atomic switches are not merely switches; they also have intriguing applications to QC, multivalued memory, logic gates, and even artificial synapses. Quantized conduction was discovered by using an STM to control ion movement and electrochemical reactions on the atomic scale through application of precise voltages with positive or negative polarity [21].

In a gap type of atomic switch with a Ag electrode/Ag_2S/tunnel gap/Pt electrode structure, when a relatively small voltage is applied to the Pt electrode, a Ag protrusions grows slowly and forms an ultra-fine point contact with the Pt electrode. This atomic scale point contact enables QC to emerge and makes it possible to construct a multi-value memory [22]. As shown in Fig. 5, the memory consists of a 1 × 2 array of crossbar structures (Ag electrode/Ag_2S/tunnel gap/Pt electrode), with an atomic switch formed at each of the cross points. The two switches can be made

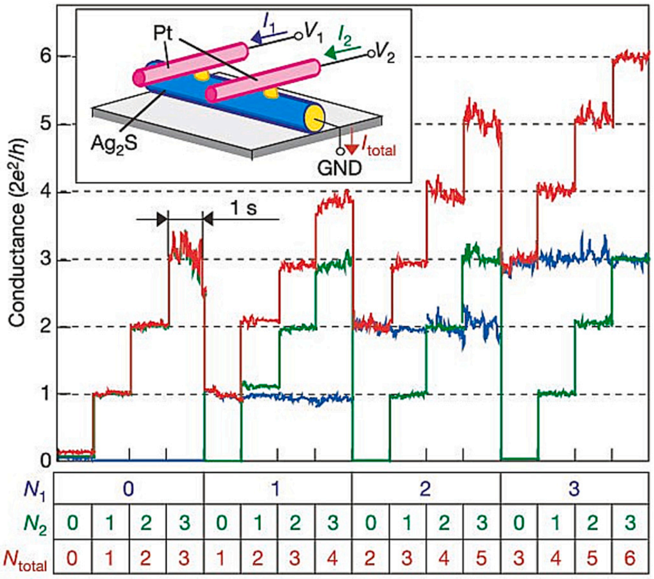

Fig. 5. Changing the QC states of individual channels independently from $N = 0$ ($\times\ 2e^2/h$) to 3 ($\times\ 2e^2/h$). 50-ms-long pulsed bias voltages of 200 mV (from 0 to 1), 100 mV (from 1 to 2), 80 mV (from 2 to 3) and − 260 mV (from 3 to 0) were applied. Reprinted with permission from Ref. 22. Copyright (2005) Springer Nature.

Table 1
A performance comparison between a gapless-type atomic switch and other types of switch.

	Flash Memory	ReRAM	MRAM	PCM	FeRAM	Atomic Switch (NanoBridge)
Scaling limit	~28 nm	<10 nm	<10 nm	<10 nm	<10 nm	<10 nm
Operating temperature	-40–150 °C	-40–150 °C	-40–150 °C	0–85 °C	-40–125 °C	−269–150 °C
Retention	>10 years	>10 years	>10 years	>10 years	>10 years	>10 years
On/Off ratio	~10^4	10–10^4	1.5–2	10^2–10^4	10^2–10^3	10^4–10^5
On resistance	10^2–10^3 W	10–10^3 W	<10^2 W	10–10^2 W	–	10^2–10^3 W
Write voltage	>5 V	<3 V	<1.5 V	<3 V	<3 V	<2 V
Endurance	10^5	10^5–10^8	10^{15}	10^6–10^9	10^{10}	10^3
Operation time	<15 ns	<7 ns	–	–	–	<15 ns

to exhibit QC in different states by precisely controlling the applied voltage. Here, quantum conductance is represented by a quantum number that is obtained by dividing the electrical conduction by the fundamental unit of QC ($G_0 = 2e^2/h$), where e is the elementary charge and h is the Planck constant. In a state where QC is observed, applying a pulsed voltage of appropriate polarity causes the state of the point contact to change, thereby allowing the quantum number state to be switched arbitrarily. The experimental results in Fig. 5 show that 16 possible states (4 × 4) can be obtained by connecting two atomic switches each with four states ranging in quantum number from 0 to 3. This functionality enables the development of multi-state memories.

To understand the fundamental physicochemical processes involved in constructing an atomic point contact exhibiting QC, it is important to see how fast an atomic switch can be operated by using ion transport in solid electrolytes and electrochemical reactions at the electrolyte surface/interface. Here, STM is a powerful tool for investigating the microscopic processes at the atomic scale and can also be part of an atomic switch. The switching time from the OFF state to the ON state was measured for an atomic switch consisting of Fe-doped $RbAg_4I_5$ film evaporated on a Ag substrate and a Pt tip of an STM [30]. $RbAg_4I_5$ is naturally a superionic conductor of Ag ions, but its electronic properties change to those of a mixed conductor of Ag ions and electrons when it is doped with Fe. Fig. 6 (a) shows the typical current-time characteristics measured under application of a constant small voltage to the Pt tip, which was initially set 1 nm from the $RbAg_4I_5$ surface. In time domain (1), no current appeared at a positive voltage of +100 mV, because no reduction of Ag ions took place on the surface. Then, a negative voltage of −100 mV was applied to the Pt tip at t_2, but the current remained at almost zero up to t_3. In time domain (2), no Faradaic reaction occurred. After t_3, the current increased rapidly in time domain (3), indicating that a Ag filament started to form through a reduction process induced by tunneling current. At t_4, the filament short-circuited the tunnel gap (1 nm) and the conductance reached the value of a single atomic point contact, $1G_0$. In time domain (4), the filament became larger so that the current further increased to above $2G_0$. Finally, in time domain (5), the current reached the maximum value limited by the external resistor that was inserted in series with the measurement system.

The switching time t_s is defined as the time needed to make a single atomic point contact G_0 after applying a negative voltage, that is, $t_s = t_4 - t_2$. t_s can further be equated as $t_s = t_n + t_g$, where $t_n = t_3 - t_2$ is the nucleation time and $t_g = t_4 - t_3$ is the time of nucleus growth. Fig. 6 (a) clearly indicates that region (2) mainly contributes to t_s, thereby implying the conclusion of $t_s \sim t_n$. Thus, critical nucleus formation of Ag on the $RbAg_4I_5$ surface is rate limiting. According to the atomistic model of electrocrystallization, for applied cathodic potentials Df (< 0) higher than kT/e, t_s is given by:

$$t_s = t_0 exp\left[\frac{(N_c + \alpha)e\Delta\phi}{kT}\right] \tag{1}$$

where t_0 is a constant, Nc is the number of atoms constituting the critical nucleus, α is the transfer coefficient, k is Boltzmann constant, and T is temperature [31]. Fig. 6 (b) plots t_s as a function of applied voltage on a semi-logarithmic scale. Here, t_s decreases exponentially with increasing applied voltage, and its slope is clearly separated into two regions: voltage range (1) between −75 and − 300 mV and voltage range (2) between −300 and − 600 mV. The corresponding reciprocal slopes $b1$ and $b2$ are calculated to be 21 and 125 mV, respectively. From Eq. 1 with the measurement temperature of $kT/e = 25$ mV, the parameter $(N_c + \alpha)$ is estimated to be 1.25 in voltage range (1) and 0.2 in voltage range (2). In voltage range (2), Df is sufficiently larger than kT/e and thus $N_c = 0$ and $a = 0.2$ are obtained. Using this value of a, $N_c = 1$ is obtained in voltage region (1). When $N_c = 1$ each Ag atom generated on the $RbAg_4I_5$ surface is a nucleus of the new phase, while $N_c = 0$ indicates that the empty nucleation site acts as the critical nucleus and a single Ag atom generated represents the supercritical cluster of the new phase. These results indicate that the nucleation behavior of metal atoms on the solid electrolyte plays an important role in determining the switching characteristics.

Like the gap type, gapless atomic switches can also exhibit QC; here, the atomic point contact of a conducting filament is formed without using tunneling currents. These devices have simple structures consisting of solid electrolytes or mixed conductors sandwiched between electrochemically active and inert electrodes [32]. QC based on the transport of metal ions or oxygen ions has been observed in various inorganic materials, such as Ta_2O_5 [33,34], ZnO [35], HfO_2 [36,37], SiO_2 [38], GeS_2 [39], AgI [40], and AgInSbTe [41]. Figs. 7 (a) and 7 (b)

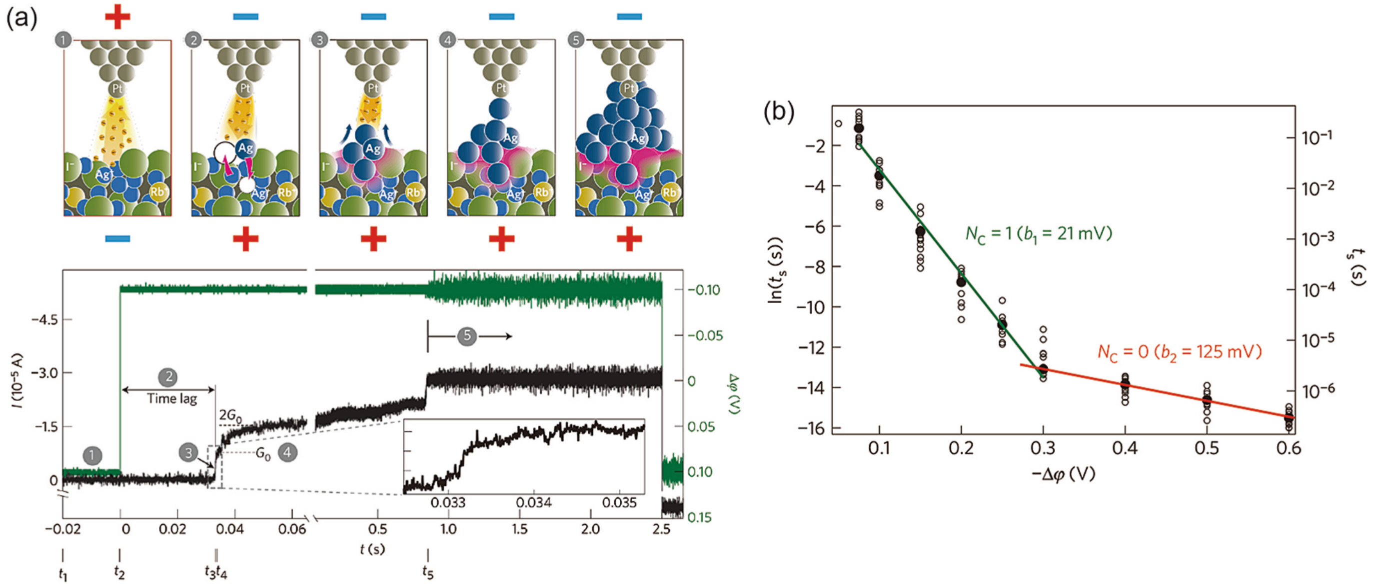

Fig. 6. (a) Relationship between filament formation process and current response in an experiment on Fe-doped $RbAg_4I_5$ film evaporated on a Ag substrate under application of a constant voltage by STM. The numbers (1–5) define five time domains in the current-time characteristic corresponding to the microscopic processes illustrated in the upper part of the figure. t_i denotes the starting time of the ith process. The inset shows the current increase in time domain (3), where the current reached the value of a single atomic point contact. (b) Switching time plotted as a function of bias voltage. The measurement was carried out at room temperature on a STM Pt tip and $RbAg_4I_5$ surface. Reprinted with permission from Ref. 30. Copyright (2012) Springer Nature.

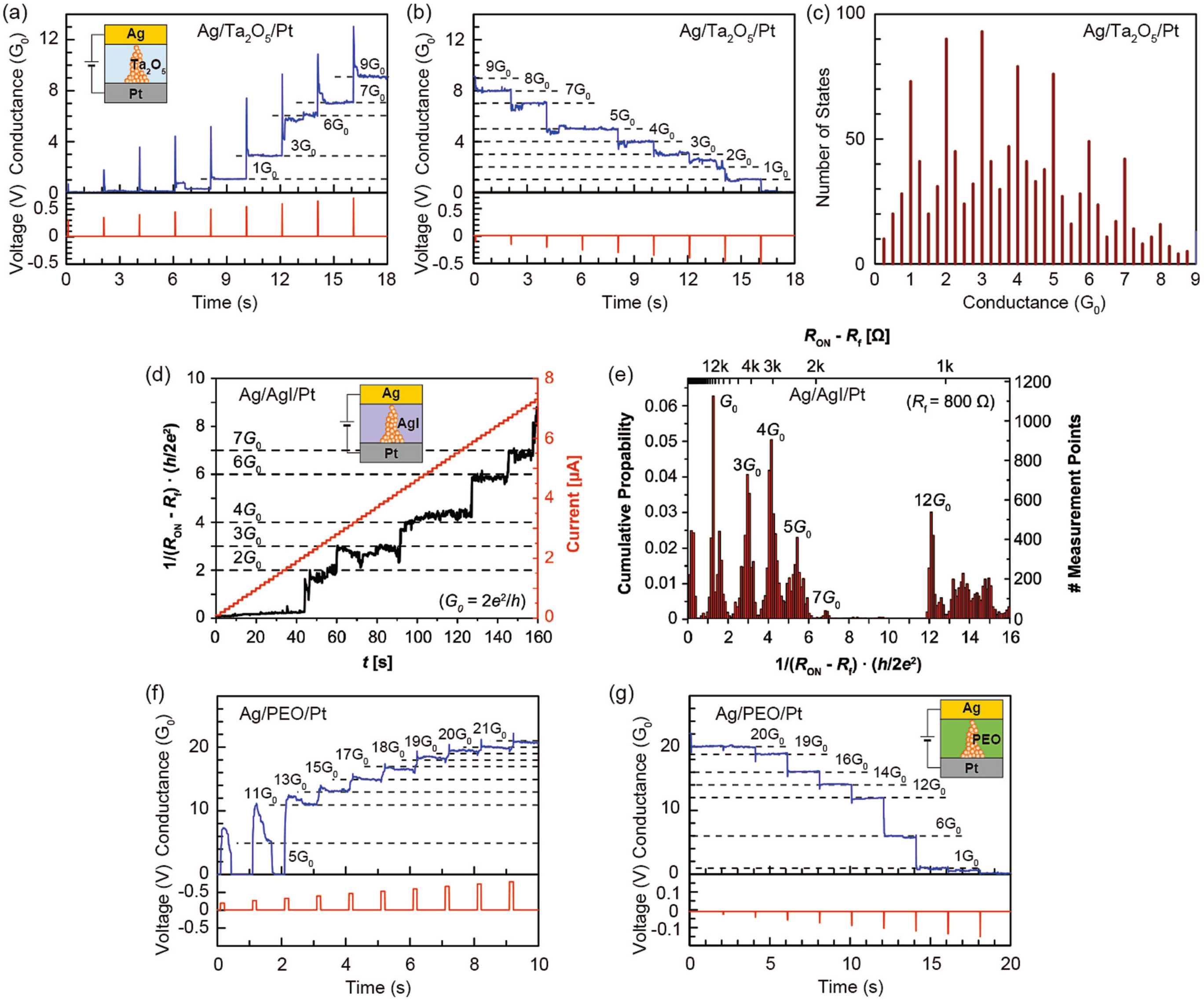

Fig. 7. QC of gapless-type atomic switches based on various solid electrolytes. Stepwise increase (a) and decrease (b) in QC observed in a Ag/Ta_2O_5/Pt device under application of positive and negative voltage pulses. (c) Conductance-state histogram created from the measured data. (d) Stepwise increase in QC observed in a Ag/AgI/Pt device under current sweep. (e) Conductance-state histogram created from the measured data. Stepwise increase (f) and decrease (g) in QC observed in a Ag/Ag-PEO/Pt device under application of positive and negative voltage pulses. Reprinted with permission from Ref. 18, 33, 40, and. Copyright (2012) Institute of Physics and (2022) Wiley-VCH GmbH.

show the QC behavior in a device with a Ag/Ta_2O_5/Pt structure under consecutive applications of positive and negative voltage pulses [33]. First, the device conductance increased in a stepwise fashion from $0G_0$ to $9G_0$ by gradually increasing the amplitude of the positive pulses. During a voltage pulse was applied, a temporary increase in conductance was observed due to the formation of a relative thick filament. Due to the structural instability of the filament formed, some Ag atoms in the filament dissolved after pulse application and a thinner filament is stabilized maintaining some G_0. By subsequently applying negative voltage pulses with gradually increased amplitudes, the device conductance decreased in a stepwise fashion from $9G_0$ to $0G_0$. Fig. 7 (c) shows a conductance-state histogram constructed from the conductance-time data. Here, the device conductance exhibits peaks at integer multiples of G_0 with a small distribution around each integer, which indicates that an atomic point contact can be controlled within a thin oxide film.

The QC state can be controlled by applying a bias current [40]. Fig. 7b (d) shows QC behavior observed for a Ag/AgI/Pt device under a current sweep. The device conductance increased in a stepwise fashion from $0G_0$ to $7G_0$ with linearly increasing current amplitude. Fig. 7 (e) plots cumulative probability and the corresponding number of conductance states obtained from the conductance-time data; it has peaks at integer multiples of G_0, similar to the case of oxide-based atomic switches.

QC has also been observed in gapless atomic switches using organic solid electrolytes [42]. Figs. 7 (f) and 7 (g) show typical QC behavior measured in a switch based on poly (ethylene oxide) (PEO) under consecutive applications of positive and negative voltage pulses [18]. Although it was difficult to control the QC below $10G_0$, the conductance increased in a stepwise fashion, in units of G_0, with increasing pulse amplitude. After reaching a certain QC value, applying negative voltage pulses with increased amplitudes resulted in a decrease in device conductance in a stepwise fashion back to $0G_0$. These experiments show that the formation of atomic point contacts is affected by ion transport in the matrix electrolytes and electrochemical reactions at metal/electrolyte interfaces. Therefore, in order to control QC states precisely, it is important to find the optimal conditions for constructing atomic point contacts. This can be done by investigating combinations of aspects, such as the voltage-current application process, type of conducting ion, ion concentration and conductivity, composition and crystal structure of ion conductors, and impurities such as residual water molecules. Similar QC behaviors to those summarized above have been observed in various organic materials, including poly(3-hexylthiophene):[6,6]-phenyl-C61-butyric acid methyl ester [43], poly(1,3,5-trivinyl-1,3,5-trimethl cyclotrisiloxane (pV3D3) [44], Ag salt-included polyvinylimidazole (PVI) [45], Ag or Cu salt-included polyaniline (PANI) [46], and triptycene-based azo polymer (TBAP) [47].

The relationship between QC and the atomic structure of the point contact of a Ag filament in an organic electrolyte (PEO) was investigated [48]. Fig. 8 (a) shows a typical I-V (black) curve and a corresponding conductance-voltage (red) curve for a Ag/PEO/Pt device with a 40-nm-thick PEO film. Under positive bias sweeping, the conductance curve increased in a stepwise fashion, as indicated by the dotted lines in the plot and reached a QC state that depends on the voltage sweep range. When the bias voltage was subsequently swept back, the device conductance showed a stepwise decrease. The stability of the QC states was investigated by measuring the retention times of different conductance values, as shown in Fig. 8 (b). When the QC state was ≤1G_0, the device conductance dropped to zero immediately and thus did not show any retention characteristics. In contrast, when the device conductance exceeded 2G_0, the retention time became longer for higher conductance values, as shown in Fig. 8 (b). As conductance-state histogram was created by counting the conductance states appearing as plateaus in the conductance-voltage curves. As summarized in Fig. 8 (c), the devices exhibited large peaks at integer multiples of G_0, clearly demonstrating QC behavior. In addition, distinct peaks appeared at half-integer multiples of G_0 with small fractional conductance variations.

Controllability of QC states is essential for designing and optimizing the characteristics of atomic-scale devices. Here, ab initio simulations were performed in an attempt to understand the correlation between QC states and the atomic point contact structure. QC originates from the narrowest region of a metal filament, i.e., region including the atoms (numbered $n = 1, 2, 3, \ldots$) participating in the atomic point contact. It was observed that the metal filament is composed of small Ag clusters that precipitate through the PEO matrix [49]. Therefore, we modeled the atomic point contact structure as a chain consisting of Ag atoms attached to two Ag blocks, each with a face consisting of nine Ag atoms, as illustrated in Fig. 8 (d). The conductance states and their transmission eigenvalues and eigenstates of the entire structure were evaluated using first-principles density functional theory simulations. The Ag atoms in the blocks on both sides of the atomic chain were fixed, while Ag atoms in the atomic chain were relaxed so that their total energy was minimized. Fig. 8 (d) illustrates geometrically relaxed structures with 10-, 11-, and 12-Ag atom chains in the center region. The 10-atom chain forms a single-atom point contact with a conductance of almost 1G_0 at E_F, while the 11- and 12-atom chains form approximately two-atom point contacts with conductance lower and higher than 2G_0 at E_F, respectively, as shown in Fig. 8 (e). Transmission channel analysis revealed that the 11-atom chain possesses eight conducting channels at

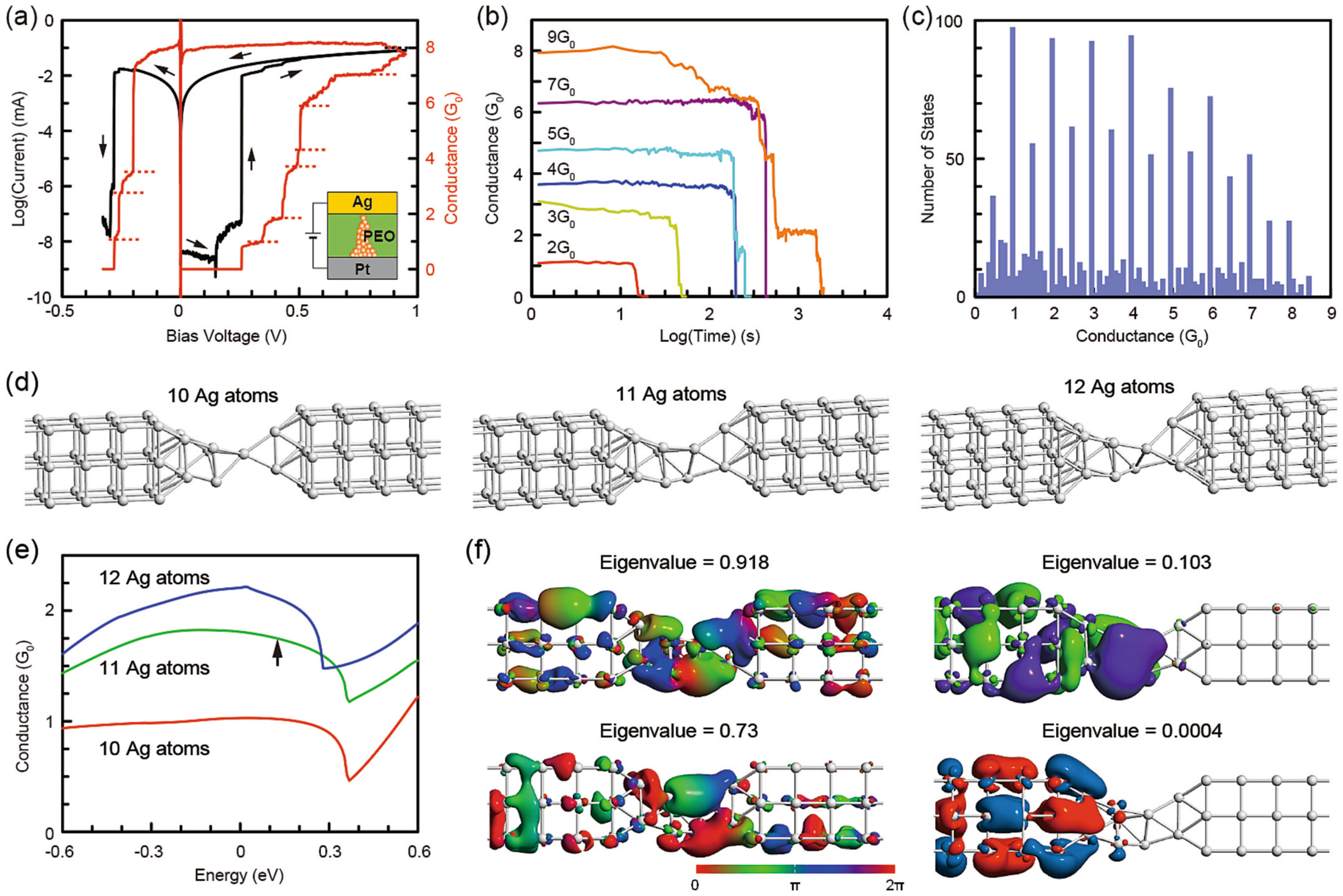

Fig. 8. (a) I-V and corresponding conductance curves of a Ag/PEO/Pt device. (b) Spontaneous conductance decay behavior, measured as a function of time, after realizing each conductance value. (c) Conductance-state histogram evaluated from the conductance curves. (d) Geometrically optimized (relaxed) structures consisting of 10-, 11-, and 12-Ag atom chains linking two blocks with faces consisting of nine Ag atoms. (e) Energy-dependent conductance plot for structures with different numbers of Ag atoms in the center region shown in (d). (f) Transmission eigenstates of 11 Ag atom chains forming a two-atom contact, calculated for the four higher eigenstates at 0.12 eV, as indicated by the arrow in (e). Reprinted with permission from Ref. 48. Copyright (2017) Wiley-VCH GmbH.

0.12 eV above E_F (indicated by the arrow in Fig. 8 (e)). Of these channels, three with eigenvalues higher than 0.1 display continuous wave functions between two blocks, whereas the remaining five with eigenvalues lower than 0.001 do not span the two blocks, as shown in Fig. 8 (f). This means that three partial transmission channels dominate the total conductance. Overall, these simulations showed that the conductance of an atomic point contact is significantly altered by the atomic configuration, resulting in half-integer multiples and fractional variations of the conductance state. They also predicted that the atomic point contact is significantly affected by the presence of hydroxyl ions.

4. Neuromorphic devices

4.1. Synapse devices

With the rapid development of AI in recent years, there has been growing interest in using solid-state ionic devices as building blocks of neuromorphic computing such as artificial synapses [50–52] and physical reservoirs. Neuromorphic devices are expected to be the basic elements of next-generation AI hardware that operates with low power consumption, inspired by the functions of the human brain [53]. The latest supercomputers require 1000 kW·h of electricity to train natural language models. However, as the brain can only use the energy obtained and stored by living organisms, it can classify, predict, and think using very little electricity (about 20 W) [54].

The neural network in the human brain exhibits plasticity; it is constantly undergoing functional and structural changes in response to external stimuli, showing dendrite growth and enhanced chemical transmission at synapses involved in memory and learning. This synapse's plasticity can be mimicked using conventional semiconductor devices, but a circuit containing ten or more transistors is required [55]. In contrast, synaptic plasticity can be realized with just one solid-state ionic device, such as an atomic switch or a resistive change device.

The operating principle of a gap type of atomic switch shown in Fig. 9 involves forming and growing a conductive filament and its subsequent bridging of electrodes. These features are similar to the plasticity observed in the human nervous system. One of the models of human memory distinguishes between short-term and long-term memory. An artificial synapse based on an atomic switch has been proposed that mimics these short-term and long-term memory functions of the human brain. Fig. 9 (a) shows the structural changes caused by short-term plasticity (STP) and long-term plasticity (LTP) in the atomic switch when a pulsed voltage (learning signal) is applied. By repeatedly applying pulse voltages, Ag ions accumulate on the surface of the mixed conductor Ag_2S and a supersaturated state is reached, leading to Ag nucleation and growth. As this growth continues, the Ag cluster forms a bridge between the Ag electrode and the Ag_2S. By exploiting the conductance changes in the atomic switch associated with these structural changes, short-term and long-term memory functions can be achieved. The properties of the short-term memory induced by STP are shown in Fig. 9 (b). When relatively short pulse voltages are applied, the Ag nucleus forms and grows on the Ag_2S surface with continued pulse repetition, but the nucleus stay below the critical size required for thermodynamic stability. That is, once the pulse voltage stops, the Ag cluster contracts and disappears, causing the conductance to decay. However, this decay becomes less pronounced as the number of pulses increases. This phenomenon is similar to the nature of short-term memory, where information is quickly forgotten after a short period of time, but the time required to forget gradually increases with repeated learning.

The long-term memory induced by LTP is shown in Fig. 9 (c). Here, when a pulse voltage of relatively long duration is applied, a Ag nucleus forms and grows on the Ag_2S surface as the number of pulses increases, and the stable Ag cluster form a bridge once they exceed a critical size.

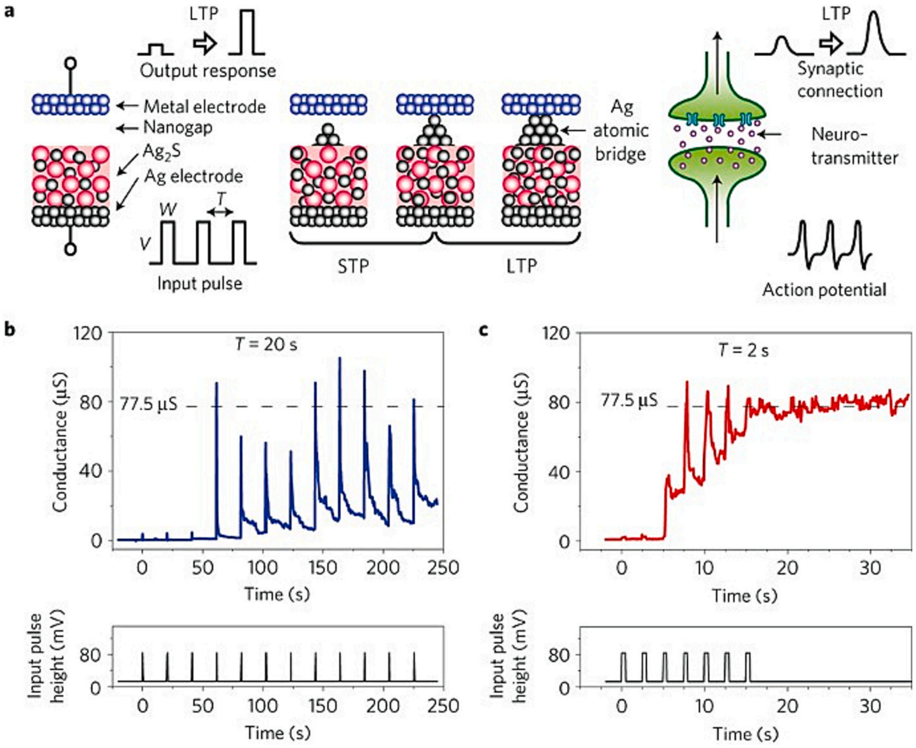

Fig. 9. Mimicking synaptic properties by using a gap-type atomic switch based on Ag_2S. (a) When an input pulse is applied, Ag atoms precipitate from the Ag_2S electrode, forming an atom bridge between the Ag_2S electrode and the opposing metal electrode. If the precipitated Ag atoms do not form a bridge, the system functions as an inorganic synapse with a short-term memory (STP). When a bridge is formed, it functions as a long-term memory (LTP). (b), (c), Changes in the conductivity of inorganic synapses when input pulses ($V = 80$ mV, $W = 0.5$ s) are applied at intervals of $T = 20$ s (b) and 2 s (c). Reprinted with permission from Ref. 52. Copyright (2011) Springer Nature.

Therefore, increased conductance is maintained even after the pulse voltage stops. This phenomenon is similar to the property of long-term memory, where information is retained for a long time after repeated learning. Thus, by taking advantage of these properties of the atomic switch, artificial synaptic devices can potentially mimic synaptic functions.

The synaptic behavior can also be demonstrated with three-terminal ion-gated transistors (IGTs), in which the channel conductance is controlled by insertion and extraction of mobile ions between a mixed conductor channel and an electrolyte gate, as shown in Fig. 2(e). An ideal weight update in such synaptic transistors, in which conductance changes linearly with the gate voltage, is essential for applications in analog computing systems [56]. Protons with an ionic radius of 0.04 Å have a higher diffusion rate than other ions, which means that IGTs operating by proton insertion and extraction can operate faster without affecting the stability of the channel material [57,58]. Several research groups have reported IGTs that exhibit various synaptic behaviors, including a chitosan-based IGT with an ITO or an indium-zinc-oxide (IZO) channel [57,59], Nafion-based IGT with a poly(3,4-ethylenedioxythiophene):polystyrenesulfonate (PEDOT:PSS) or a WO_3 channel [58,60,61], and a mesoporous silica-based IGT with an ITO channel [62].

A proton-gated transistor with an IZO channel and electron-beam lithography (EBL) patterned Nafion electrolytes is illustrated in Fig. 10 (a) [63]. EBL patterning of a spin-coated Nafion is potentially a versatile way to make proton-based neuromorphic devices [64]. The transistor illustrated in Fig. 10 (a) is analogous to a biological synapse; the gate electrode and the IZO channel correspond to the pre-synapse and post-synapse, respectively, as illustrated in Fig. 10 (b). The channel conductance is modulated by applying gate voltage in controlled way based on the insertion and extraction of protons between the IZO channel and the Nafion electrolyte. By applying gate voltage pulses, the device exhibited various short-term plasticities including paired-pulse facilitation/depression (PPF/PPD) and spike-timing-dependent plasticity (STDP) as well as long-term potentiation/depression (LTP/LTD). Fig. 10 (c) shows the change in the channel conductance when 10 gate voltage pulses with a fixed pulse amplitude and varied pulse widths and interval times were applied. The device exhibited short-term memory for shorter pulse widths, wherein the channel conductance decayed back to the initial state. As the pulse width became longer, the channel conductance decreased initially but maintained a constant level for more than 10 min., which is analogous to a long-term memory. It was found that the short-term memory behavior is mainly determined by proton diffusion in the IZO channel, whereas the long-term memory behavior is dominated by proton diffusion in the Nafion electrolyte.

Fig. 10 (d) shows typical PPF and PPD (inset) behaviors measured under application of two successive positive and negative voltage pulses. The PPF/PPD index was calculated from the ratio of the amplitude to the second peak to that of the first peaks and are plotted as a function of the time interval between pulses in Figs. 10 (e) and (f). Both indices increase with decreasing time interval, mimicking the human brain's facilitation/depression of the second synaptic transmission relative to the first when the pre-synapse is successively stimulated.

Of the various IGTs available, those based on Li^+ ions have emerged as promising candidates for making hardware neural networks for analog computing [65]. Several research groups have reported similar transistors, including a lithium phosphorus oxynitride (LiPON)-based IGT with a lithium cobalt oxide (LCO) channel [56], Li_3PO_4-based IGT with a WO_x channel [66], $Li_3PO_xSe_y$-based IGT with an LCO channel [67], and lithium silicate-based IGT with a MoS_2 channel [68]. In general, LCO has shown high working potential, high volumetric capacity, and good endurance in electrochemical cycling in solid-state Li^+ ion batteries [69]. Many cations have been investigated as substitutes for Co that could improve the reversibility and enhance the capacity of electrochemical Li/LCO cells. Among them, Mg^{2+} can substitute Co sites and replace Co^{3+}, which significantly increases the electronic conductivity

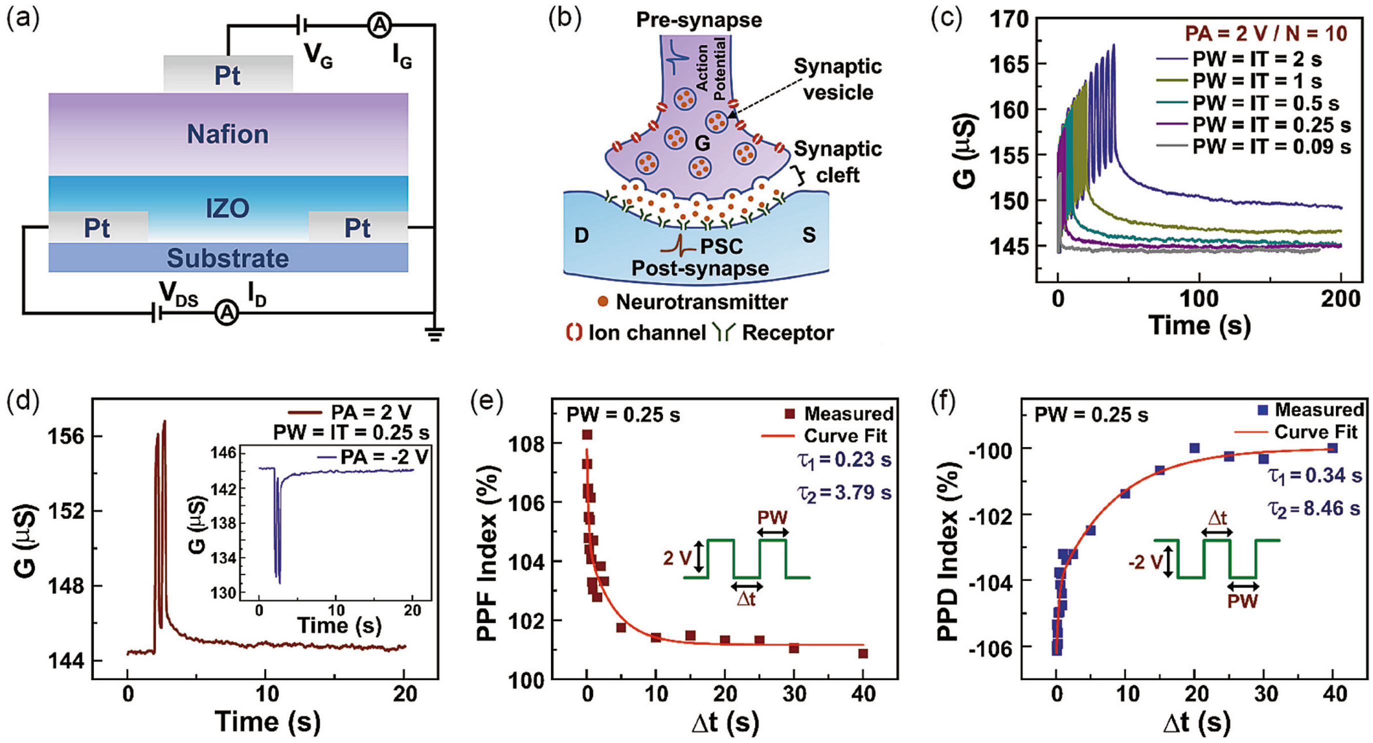

Fig. 10. Synaptic plasticity demonstrated in a Nafion-based IGT with IZO channel. (a) Schematic cross section of the device. (b) Signal transmission in a biological synapse explaining its similarity to the IGT. (c) Short-term memory and long-term memory operations in proton-gated transistor for different pulse widths. (d) Typical PPF and PPD behaviors under application of two successive positive and negative voltage pulses. The corresponding PPF (e) and PPD indices are plotted as a function of the interval time (Dt) between the pulses. Reprinted with permission from Ref. 63. Copyright (2023) American Chemical Society.

of the LCO matrix through hole creation [70]. The effects of Mg doping to an LCO channel on the synaptic behavior of Li IGTs with a LiON electrolyte were investigated [71].

Figs. 11 (a) and (b) show the typical LTP/LTD characteristics of transistors with LCO and Mg doped LCO (MLCO) channels when 90 consecutive negative pulses followed by 90 consecutive positive pulses were applied. Comparing these plots, it was found that the conductance level is almost one order of magnitude higher in the MLCO channel. On the other hand, the conductance of the transistor with the LCO channel exhibits saturation as the voltage pulses increase, whereas the one with the MLCO channel shows better linearity. The normalized conductance is plotted against the normalized number of pulses in Fig. 11 (c). It can be seen that the nonlinearity in conductance in the MLCO channel is significantly smaller than that of the LCO channel.

An artificial neural network (ANN) simulation was designed using the above experimental results. The network was made to perform an image recognition task on handwritten digits from the Modified National Institute of Standards and Technology (MNIST) data set. Fig. 11 (d) illustrates this fully connected neural network based on a multilayer perceptron model, consisting input, hidden, and output layers. The input consisted of 20 × 20 pixel images, and the NeuroSim+ program classified the output into digits from 0 to 9 [72]. The simulation included cycle-to-cycle and device-to-device variations. Figs. 11 (e) and (f) plot the image recognition accuracy as a function of epoch number for the transistors with LCO and MLCO channels. The transistor with the LCO channel showed a relatively low accuracy, ~65 %, with large fluctuations, while the transistor with the MLCO channel exhibited a higher accuracy, ~80 %, with less fluctuations. It also found that Mg doping improves other synaptic plasticities, such as PPF/PPD and STDP. These results indicate that elemental doping of the channel of Li^+ ion-gated synaptic transistors has great potential for the development of robust neuromorphic systems.

4.2. Physical reservoir computing

A reservoir network is a computational model designed to mimic the structure of biological neural networks. It comprises three layers: an input layer, a reservoir layer, and an output layer. (Fig. 12 (a)). The

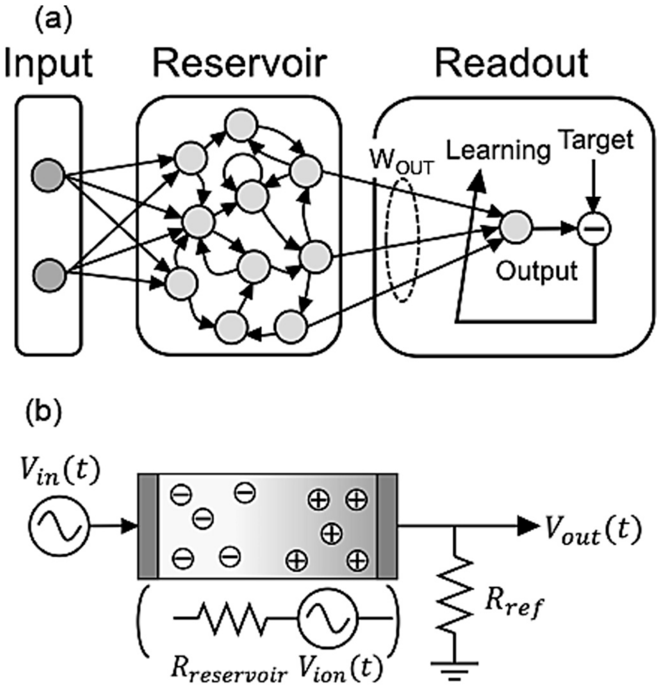

Fig. 12. (a) Artificial neural network (ANN) for reservoir computing. (b) Reservoir operations based on movements of ions in an electrolyte.

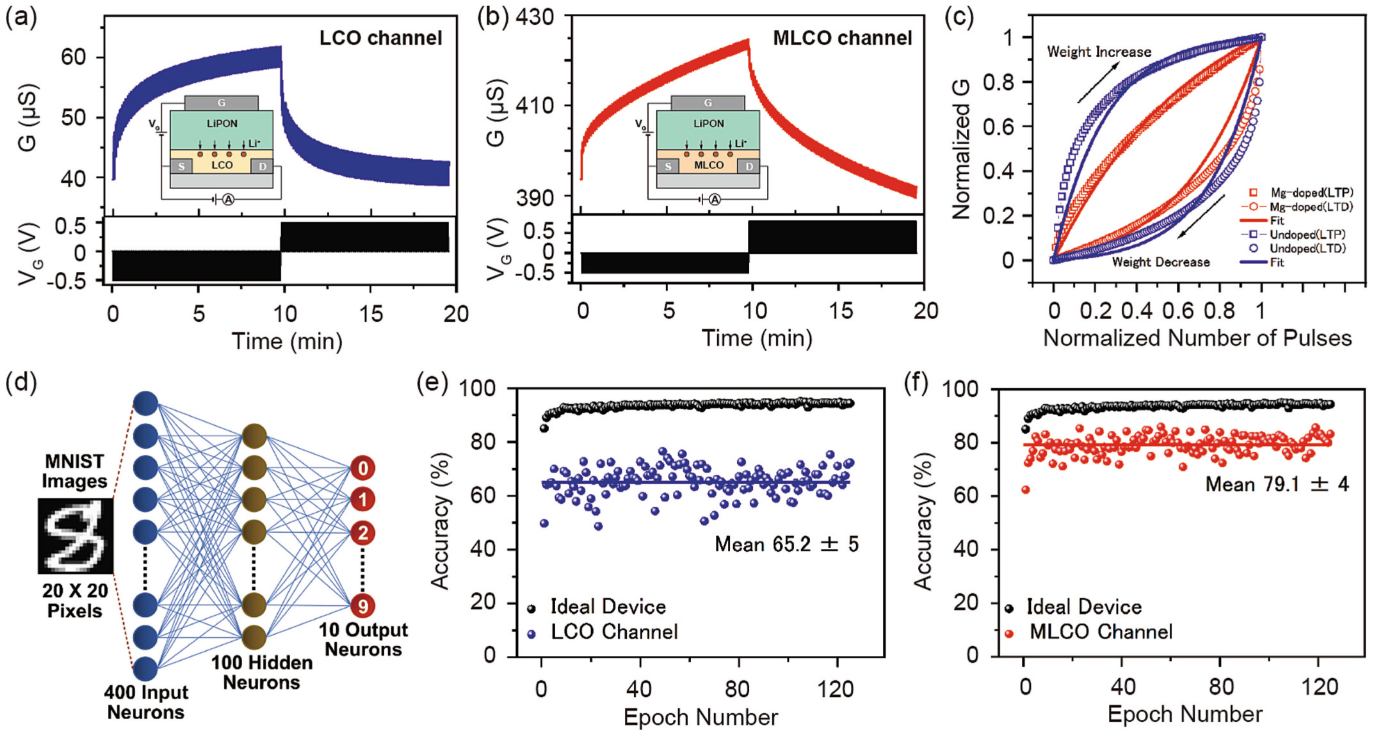

Fig. 11. Conductance of (a) LCO and (b) Mg-doped LCO (MLCO) channels under 90 consecutive negative and 90 consecutive positive gate voltage pulses. The insets illustrate the cross sections of the transistors. (c) Plots of normalized conductance versus normalized number of pulses. (d) Schematic diagram of ANN based on a multilayer perceptron model for recognizing handwritten digits in images. Image recognition accuracy of simulation models based on measured data from IGTs with (e) LCO and (f) MLCO channels. Reprinted with permission from Ref. 71. Copyright (2023) American Chemical Society.

reservoir layer performs nonlinear transformation and short-term memorization of the input signals, while the readout layer optimizes the synaptic weights between the reservoir layer and the output layer by learning. *Physical reservoir* realizes the function of the reservoir layer such as by using solid-state devices [73] and materials exhibiting various physical [74] and chemical phenomena [75]. Using hardware for physical reservoir computing enables much faster data processing than using software for conventional reservoir computing and reduces power consumption [76].

4.2.1. Reservoir devices using nanowire- and nanoparticle-aggregates and polycrystalline film

Here, we focus on an ionic physical reservoir that can perform both of a nonlinear transformation and short-term memorization just by diffusing ions in a solid electrolyte. Applying a bias of $V_{in}(t)$ moves the ions and their distribution in the solid electrolyte becomes non-uniform (Fig. 12 (b)). This biased distribution of ions gives rise to an internal electric field in a direction that cancels the electric field of the applied bias $V_{in}(t)$. The output of the reservoir layer $V_{out}(t)$ is expressed as follows.

$$V_{out}(t) = \frac{R_{ref}(V_{in}(t) - V_{ion}(t))}{R_{reservoir} + R_{ref}} \tag{2}$$

Here, $V_{ion}(t)$ is the potential difference between the electrodes due to the internal electric field made by moved ions, $R_{reservoir}$ is the resistance of the reservoir layer, R_{ref} is the resistance of a reference resistor, and t is time. The reservoir output $V_{out}(t)$ due to the potential made by ions $V_{ion}(t)$ is different from the input voltage $V_{in}(t)$. Since the ions diffuse much more slowly than electrons, the distribution of ions depends on the past voltage input history much more than that of electrons. These characteristics enable a nonlinear transformation and a short-term memory to be realized.

Nonlinear transformation and short-term memory operations based on the above principle have been demonstrated in physical reservoirs based on ionic liquids [77]. These systems show good reproducibility, which is a key performance metric in reservoir computing, because a statistically large number of ions are involved in the operation. By utilizing redox reactions occurring at electrodes and grain boundaries, the resistance of the reservoir layer ($R_{reservoir}$) itself can be changed depending not only on the applied bias at the time but also on the history of the voltage inputs. This change in resistance can enlarge the nonlinear transformation and the short-term memory capacity larger than that of exploiting only ionic diffusion [78,79].

A reservoir layer formed from Ag_2S can have various network structures (Fig. 13). The first such network to be demonstrated consisted of electrochemically grown Ag_2S nanowires (Fig. 13 (a)) [80,81] Here, nonlinear transformation and short-term memory were realized by the growth and shrinkage of Ag clusters at the huge number of intersections between nanowires. Subsequently, similar operations were demonstrated using Ag_2S nanoparticles (Fig. 13(b)) [82–84]. In these networks, the changes in the local electric potential due to the growth and shrinkage of Ag clusters at some intersections induced growth and shrinkage of Ag clusters at other intersections. Thanks to this chain reaction, the nanowire and nanoparticle networks worked as recurrent ANNs.

As same with the conventional computers, reproducibility is a necessary requirement also for a reservoir computing. In Ag_2S crystals, Ag atoms precipitate and dissolve in accordance with the difference in electrochemical potential between the silver ions inside the Ag_2S and the Ag atoms on the surface. Since the electrochemical potential is a logarithmic function of the ions' concentration, when small crystals, i.e., nanowires and nanoparticles, containing only a small number of Ag ions are used, the electrochemical potential significantly changes even when only a few Ag atoms are precipitated [85]. As a result, the precipitation and dissolution process of Ag atoms in response to changes in the electric potential is highly reproducible. Because of this mechanism and the large number of junctions, the computations performed with the above described networks had high reproducibility.

On the other hand, as the size of the Ag_2S crystal increases, the reproducibility of the growth and shrinkage of the clusters decreases. This effect was demonstrated in a network of Ag_2S islands [86]. Here, it was found that in islands 100 nm in size, which contains a large number of Ag ions, only the movements of ions had high enough reproducibility to be used as a basis for a device. On the other hand, it was found that a recurrent ANN could be realized from a polycrystalline Ag_2S thin film [87]; in this case, the grain boundaries act as barriers to ion diffusion, and each grain of the film functions as an independent node of a network (Fig. 13 (c)). To make each grian act as an indenepned node, the voltage conditions for inhibiting diffusion across the grain boundaries must be kept.

Fig. 14 illustrates a nonlinear transformation performed in a physical reservoir made from polycrystalline Ag_2S thin film [88]. For a rectangular wave voltage input, output voltage decays as a result of an internal electric field made by ions diffusing (Fig. 14 (a)). The time constant of this decay is 0.17 ms. As the input voltage is increased, precipitation and dissolution of silver atoms begin to occur. As the number of silver ions in the Ag_2S crystal decreases due to precipitation, $V_{ion}(t)$ in eq. (2), eventually cannot be large enough to cancel the electric field caused by the input voltage and the output increases (Fig. 14 (b)). When a voltage of opposite polarity is applied, the Ag ions return to the crystal and the output decays back to zero. The experimental results described below were obtained with a Ag_2S polycrystalline film under voltage conditions

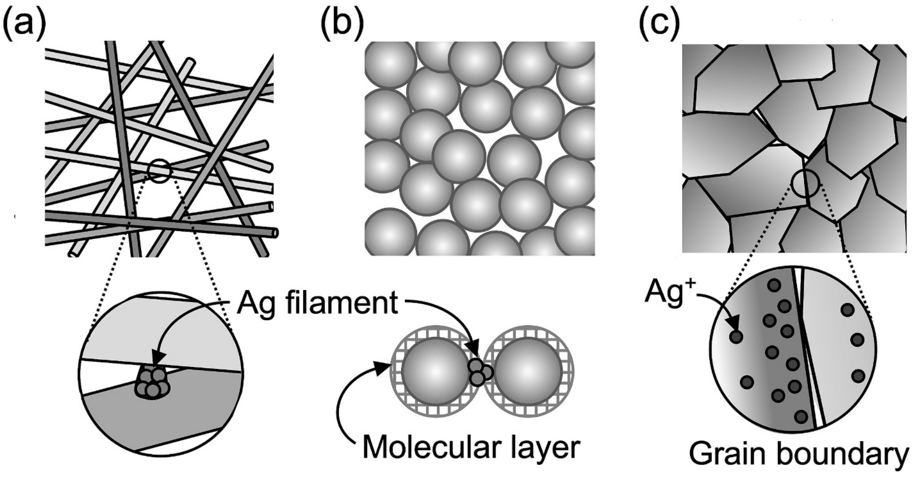

Fig. 13. Various physical reservoirs made of (a) nanowires, (b) nanoparticles, and (c) polycrystalline film.

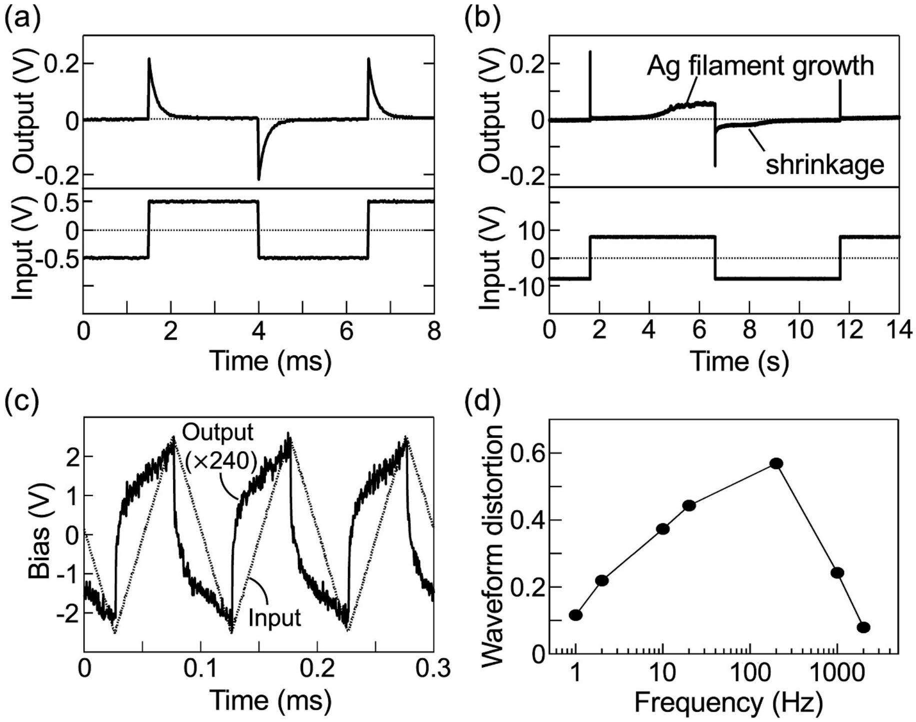

Fig. 14. Nonlinear transformation using a Ag_2S-based reservoir. Output measured with rectangular pulse input with an amplitude and period of (a) 0.5 V and 2.5 ms and (b) 7.5 V and 5 s. (c) Measured output for triangular pulse input (2.5 V, 0.05 ms). (d) Degree of nonlinear transformation of triangular pulse input. Reprinted with permission from Ref. [89]. Copyright 2024 The Japan Society of Vacuum and Surface Science.

that do not cause the precipitation and dissolution of Ag atoms observed in Fig. 14 (b).

Fig. 14 (c) shows an example of the output when a triangular wave is input. The triangular wave is nonlinearly transformed with a certain delay by the internal electric field made by moving Ag ions. The distortion of the output waveform from the triangular wave was largest at 200 Hz (Fig. 14 (d)). Similar behavior was observed in a copper sulfide polycrystalline thin film [89] and co-evaporated amorphous thin films of Ag and tantalum oxide and copper and tantalum oxide [90].

Fig. 15 (a) shows the change in output voltage when a 4-bit pulse train (pulse width 0.1 ms) is input to a reservoir layer of a polycrystalline Ag_2S thin film. In this measurement, a positive voltage triangular pulse was used as the input “1”, and a negative voltage triangular pulse was used as the input “0”. The output voltage was read out when half the pulse width had elapsed after the pulse of the final bit was input. The readout voltage was widely and discretely distributed depending on the input bit pulse train (Fig. 15 (b)). On the other hand, when the pulse width was set to 1 ms, the readout voltage was distributed only into two groups. This is because, when the pulse width is sufficiently larger than the time constant, the ions' distribution depends only on the final input pulse.

Next, the experiment of the short-term memory task is introduced. In this measurement, 10 different bit-trains consisting of 1000 bits for each train generated by random numbers were prepared, and these were converted into positive and negative triangular voltage pulse trains to be used the input waveforms. The output voltage was measured at the time when the amplitude of the input triangular wave was at its maximum. In addition, the short-term memory task used the output voltage values before and after the maximum as output from virtual nodes [91].

Fig. 16 shows the results of a short-term memory task performed with a polycrystalline Ag_2S thin film. The short-term memory capacity, calculated by summing the determination coefficients for each delay, was highest at a pulse width of 1 ms (Fig. 16 (a)). The dependence of the determination coefficient on the delay (Fig. 16 (b)) suggests that the

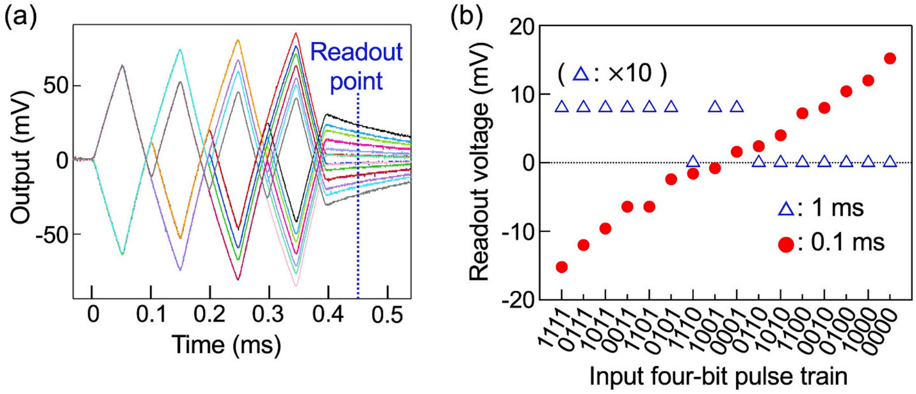

Fig. 15. Experimental result on 4-bit pulse classification. (a) Change in output measured for an input consisting of a four-bit pulse train. The readout point is indicated. (b) Readout voltages for each four-bit pulse train. Reprinted from Ref. [98]. Copyright 2024 The Japan Society of Vacuum and Surface Science.

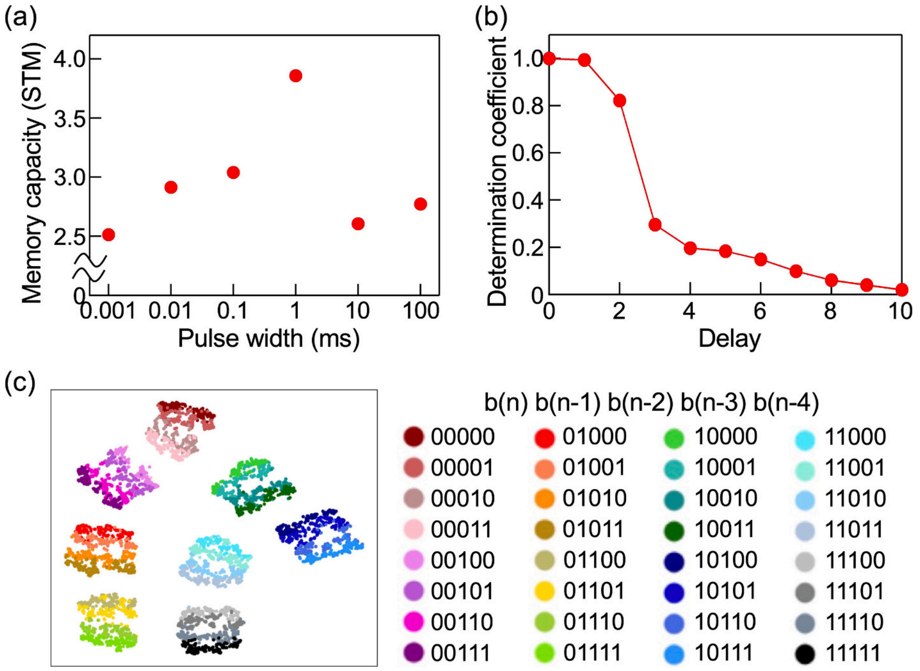

Fig. 16. Results of short-term memory task with Ag_2S-based reservoir. (a) Memory capacity measured as a function of pulse width. (b) Determination coefficient measured for a pulse width of 1 ms. (c) Distribution of output vectors visualized by t-distributed stochastic neighbor embedding (t-SNE). Reprinted with permission from Ref. [95]. Copyright 2024 The Japan Society of Vacuum and Surface Science.

input waveform for the last four pulses can be reproduced by the reservoir. The experimental result using a 4-bit pulse train as input (Fig. 15) suggests that the physical reservoir should be able to reproduce the input waveform, i.e., the determination coefficient can be 1, up to a delay of 3. However, it was found that the reservoir could not do so, possibly because the short-term memory task requires the reproduction of a randomly arranged bit sequence. When focusing on the distribution of output vectors (600 dimensions: 3 output electrodes × 200 nodes in this measurement), they were clearly separated depending on the values of the four consecutive bits (Fig. 16 (c)). Moreover, physical reservoirs made of co-evaporated film consisting of copper and tantalum oxide have shown clearly separated distributions of output vectors depending on six consecutive bits [89].

Solid-electrolyte physical reservoirs have several potential applications. In particular, demonstrations have been carried out for edge-AI applications including voice recognition [92] and object recognition [93] because reservoir computing is suited to processing time-series data. Most of these studies used cameras or microphones to collect light and sound information and then converted that information into voltage signals to be input to the physical reservoir. Such a process can be a bottleneck to high-speed processing, so a physical reservoir that can accept input signals directly from the environment is considered to be a better approach. This approach, called “in-sensor computing”, has been taken in developing physical reservoirs that have a pressure sensing function [94].

Moreover, solid-electrolyte reservoirs have been used for in-sensor computing with directly input light [91,95]. For example, silver sulfide is an n-type semiconductor with a band gap of about 1 eV [96] and has been used in optical sensing devices [97]. Fig. 17 (a) shows a schematic diagram of direct irradiation of light to a reservoir layer made of polycrystalline Ag_2S thin film, where white light passes through a slit in the shape of an alphabetical character. At the same time, a sinusoidal voltage is input to one electrode to read the output as a voltage signal, and the output signals are measured with the remaining electrodes. Localized light irradiation changes the electrical conductivity of the irradiated area, which induces a different output change at each measuring output electrode. An example of such a change is shown in Fig. 17 (b). Interestingly, in this experiment, some electrodes showed an increase in their output upon irradiation, while others showed a decrease. In contrast, light irradiation causes only a decrease in the local resistance when conventional photoconductive material, resulting in an increase in output for all electrodes, following eq. (2). However, when using a solid electrolyte, both an increase and decrease happen, as can be seen in Figs. 17 (c) and (d). These various changes occurred because a local change in the electronic conductivity modified the electric potential over the whole reservoir layer, which in turn induced additional movement of the ions in the grains of other areas (Fig. 17 (d)). In this way, a solid electrolyte offers the large diversity of outputs required for a reservoir computing through the collaborative effects of photoconductivity and ionic conductivity. This is the major advantage of using a solid electrolyte for classification of directly irradiated optical patterns.

A classification task was performed on patterns produced by irradiating three slits shaped as the alphabetical characters “H”, “E”, and “Y”. Even though each pattern was irradiated at three different positions on the reservoir layer, the three letters were recognized with an accuracy of 96.6 % (Fig. 18 (a)). The output vectors obtained for “H” are distributed in separate groups for each irradiation position (Fig. 18 (b)). This means that the synaptic weights in the output layer had been optimized through learning to make them be recognizable as “H”. Although a clear dependence on the irradiated position cannot be seen for “E” and “Y”, they too could be classified like “H”. Directly irradiated optical patterns have also been classified with other solid electrolytes [90]. Moreover, a reservoir layer in a three-dimensional structure was used to classify two optical patterns irradiated simultaneously but on different sides of the structure, i.e., front and back sides [98]. Using short-term memory more effectively, sequentially input optical patterns can be classified simply by measuring outputs once all of the patterns have been input [90].

4.2.2. *Reservoir devices using thin-film layer structures*

The electrical double layer transistor (EDLT) shown in Fig. 2 (c) has been applied to physical reservoir computing (PRC) [99]. Fig. 19 (a) schematically illustrates an EDL ion-gating reservoir (IGR) utilizing Li^+-ion conducting Li-Si-Zr-O (LSZO) amorphous thin film as the electrolyte layer and hydrogen-terminated diamond single crystal (100) as the

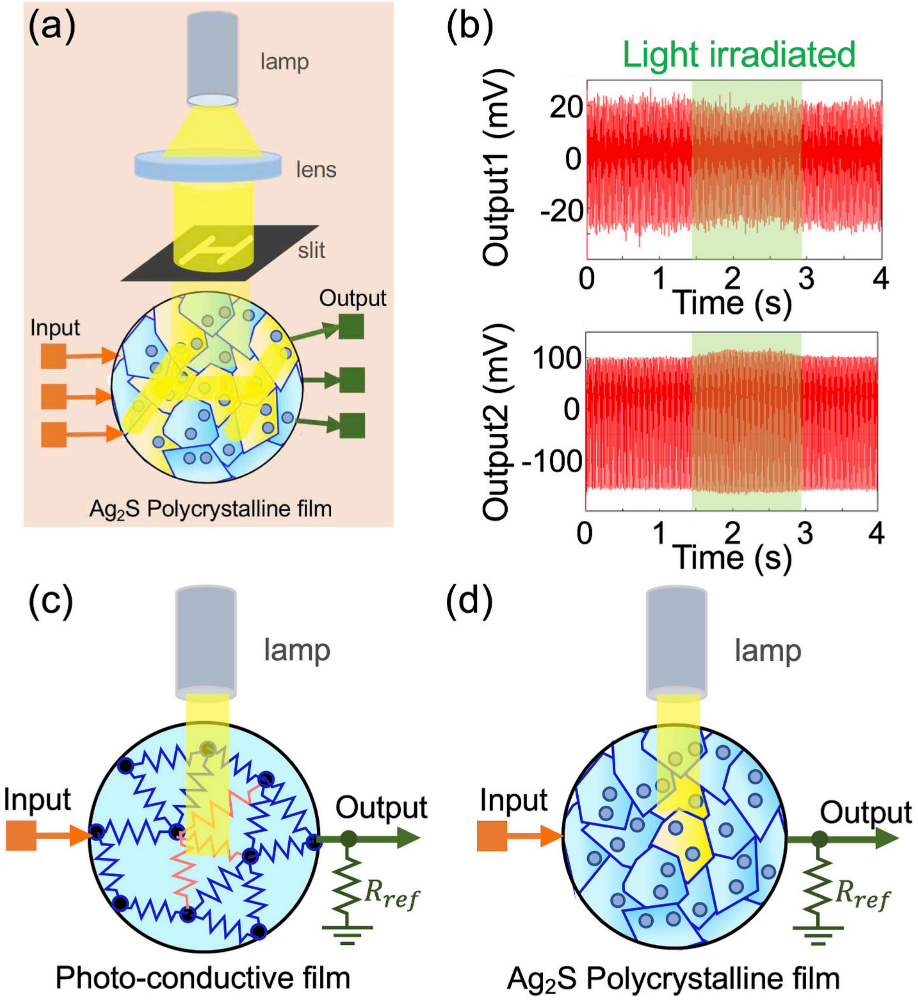

Fig. 17. (a) Schematic diagram of experiment on direct optical signal input. (b) Change in output due to light irradiation. Schematic diagram of reservoir layer made of (c) photo-conductive film and (d) Ag_2S polycrystalline film. Reprinted with permission from Ref. [95]. Copyright (2024) The Japan Society of Applied Physics.

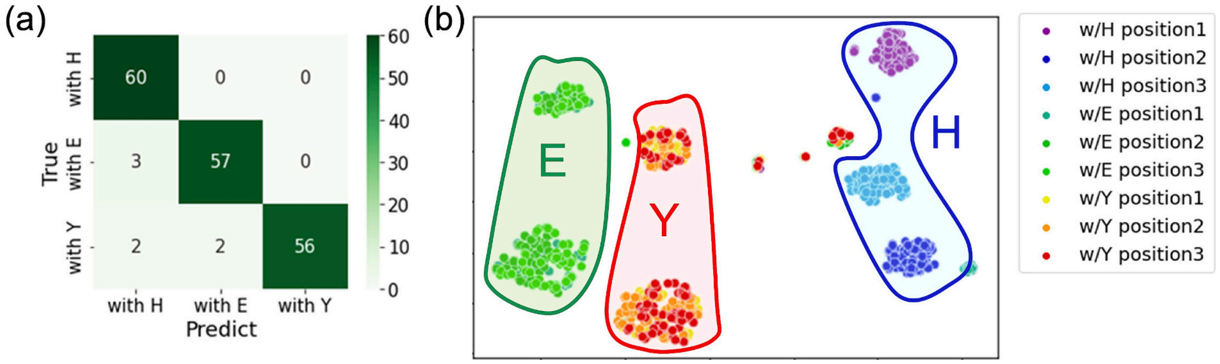

Fig. 18. Classification of irradiated slit patterns in the shapes of alphabetical characters. (a) Confusion matrix of the results. (b) Distribution of output vectors visualized by t-SNE. Reprinted with permission from Ref. [95]. Copyright (2024) The Japan Society of Applied Physics.

semiconducting channel. This EDLT has a two-dimensional hole gas (which has high hole mobility) on the hydrogen-terminated surface, enabling the electrical resistance to be tuned over four orders of magnitude through reversible EDL charging/discharging at the interface of the LSZO and the hydrogen-terminated surface. The surface p-type conduction of the diamond channel strongly affects Li^+ ion transport because the channel resistance is in addition the electrical resistance of the LSZO thin film. Hence, the electrical response of EDL charging/discharging is sensitive to the EDL charge at the location. This phenomenon, called ion-electron coupled dynamics, is responsible for the IGR having drain current outputs with various relaxation times and spike intensities (Fig. 19 (b)). The reservoir states obtained from such diverse drain currents have been used for hand-written digit recognition. As shown in Fig. 19 (c), the EDL-based IGR showed excellent performance in spite of its network size being much smaller than a three-layer neural network. Furthermore, it was used to perform a second-

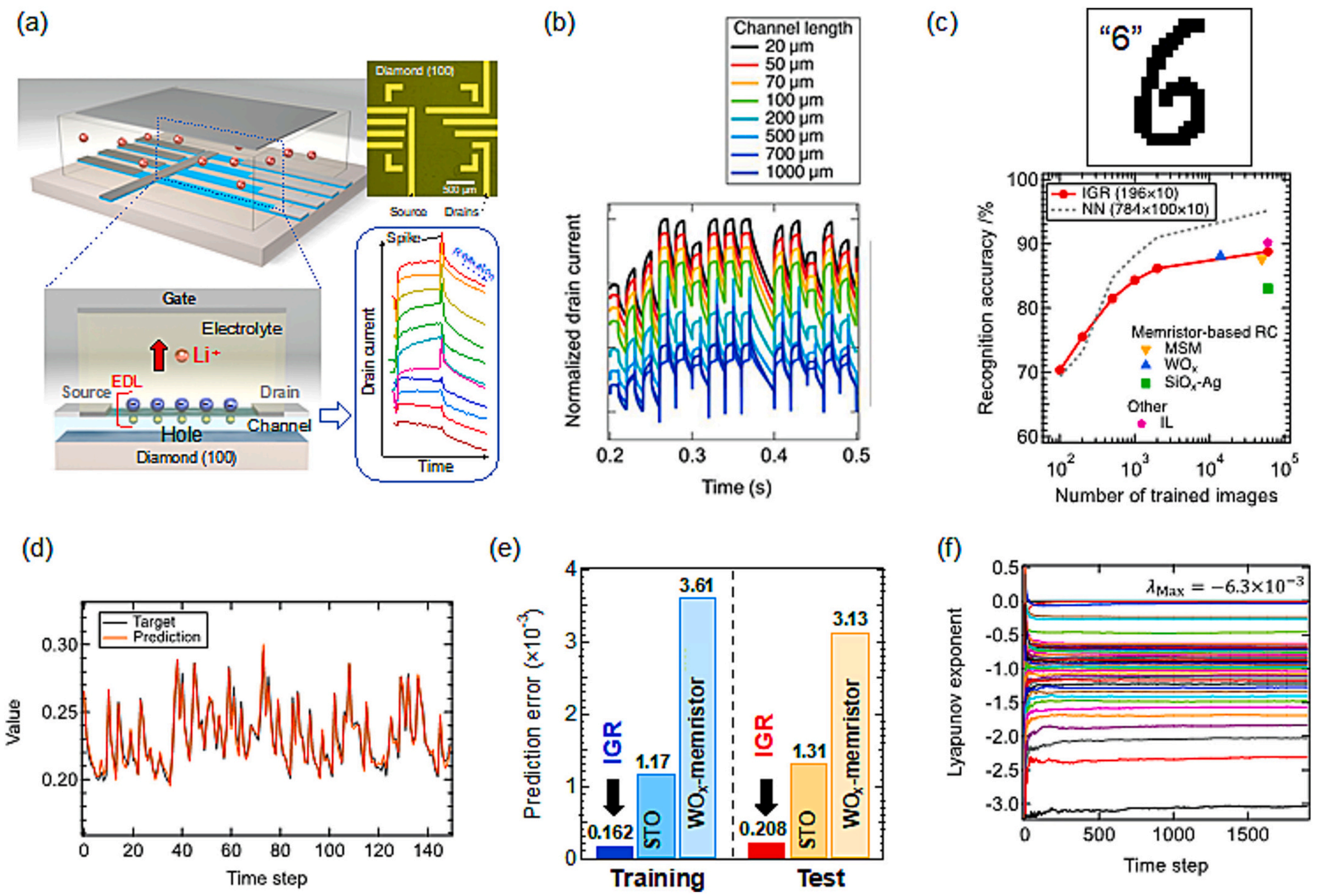

Fig. 19. (a) Illustration of ion-gating reservoir (IGR) operating in an electric double layer mechanism. (b) Drain current responses of the IGR for different channel lengths. (c) Image recognition accuracy achieved by IGR as a function of the number of training images. The dotted line shows the accuracy of a typical three-layer neural network (NN). (d) Target waveform and waveform predicted by 2nd-order nonlinear dynamic equation in the test phase. (e) Prediction errors of IGR and other physical reservoirs. (f) Lyapunov spectrum of the IGR, as calculated by the Jacobi matrix method. Reprinted with permission from Ref. [99]. Copyright (2024) the American Association for the Advancement of Science.

order nonlinear dynamic equation task, a more difficult benchmark than hand-written digit recognition. Fig. 19 (d) compares the target waveform generated by the second-order nonlinear dynamic equation and the predicted waveform generated from the EDLT drain output. The prediction is obviously low in error. Fig. 19 (e) highlights the outstanding prediction accuracy of the EDL-IGR in comparison with other PRC devices (spin torque oscillator and memristor). Such a high level of computational performance is due to the EDL-IGR's ability to exploit the complex and diverse features inherent in the ion-electron–coupled dynamics of the IGR that can be exploited as reservoir states. Theoretical studies have predicted that dynamical systems in the edge-of-chaos state between order and chaos can function as high-performance physical reservoirs [100,101]. Fig. 19 (f) shows the Lyapunov spectrum of the IGR, which was obtained by the Jacobi matrix method. The maximum Lyapunov exponent (λ_{Max}) has a very low and negative value (-6.3×10^{-3}), which evidences that the IGR is in an edge of chaos state. Other types of electrolytes (Li^+, H^+, O^{2-},) and semiconductors/semimetals (graphene, InGaZnO) have also been used to implement an EDL-IGR [102–107].

While EDLTs show relatively highspeed responses with time constants ranging from microseconds to seconds, redox transistors consisting of ion-electron mixed conducting channels tend to have much slower responses. Redox transistors would thus be useful for PRC of time-series data exhibiting slow dynamics. The Li_xWO_3-based redox-IGR transistor illustrated in Fig. 20 (a) consists of Li^+-ion and electron mixed conducting Li_xWO_3 thin film as a semiconductor channel and a lithium-ion conducting glass ceramic (LICGC) substrate as an electrolyte [108]. The redox reaction occurring through Li^+ ion and electron insertion and desertion enables reversible tuning of the channel conductance with a time constant of several tens of seconds. The Li_xWO_3-based redox transistor has a gate current that is comparable to the drain current. Here, the specific capacitance of the redox reaction is far larger than that of EDL charging because the reaction is a bulk one in the whole mixed conductor channel. Fig. 20 (b) shows a gate voltage pulse stream and the corresponding drain and gate responses of the redox-based IGR. The waveform drain current response is different from that of the gate voltage pulse stream, which is evidence that the redox transistor nonlinearly transformed the pulse stream (i.e., the time series). These different behaviors mean that the IGR can provide reservoir states not only from the drain current response but also from the gate current response, as shown in Fig. 20 (c). The double reservoir states are helpful to gain high-dimensionality as a dynamical system of the redox transistor since the number of physical nodes of transistors or any other electric devices.

PRC based on redox transistors was also demonstrated with $LiCoO_2$, which is a typical channel material for ion-gating transistors [109,110]. Fig. 20 (d) includes a schematic illustration of the redox transistor consisting of a $LiCoO_2$ channel and Li^+-ion conducting Li_3PO_4 thin film electrolyte. In that study, a physical masking method was developed to enhance PRC performance, as shown in Fig. 20 (e). Usually, masking is used to sequentialize the input and maximize the system's effective dimensionality. It is generally done by adding a mask waveform to the

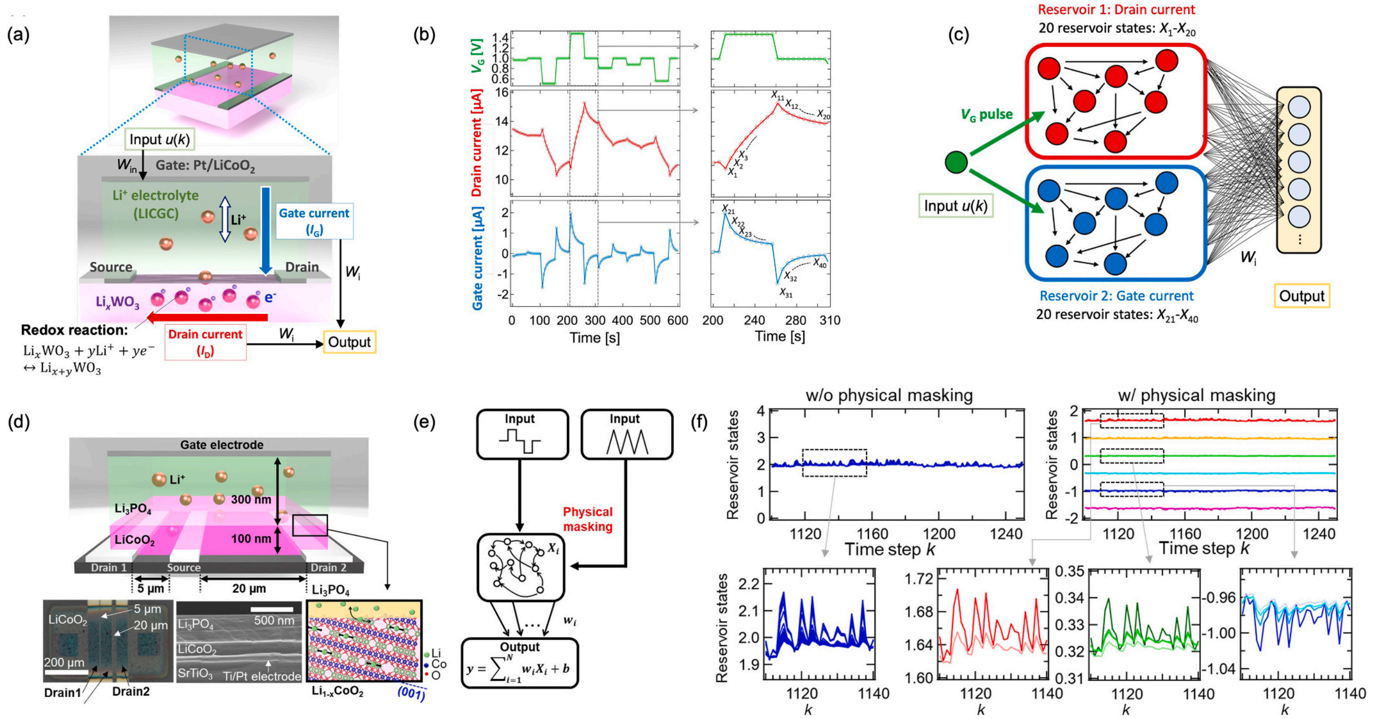

Fig. 20. (a) Schematic image of a Li_xWO_3-based redox-IGR. (b) Gate voltage pulse stream, drain current response, and gate current response during operation of the redox-IGR. Forty reservoir states X_i ($i = 1, \ldots, 40$) are obtained as shown in the panels on the right. (c) General concept of a reservoir computing system with redox-IGRs. W_i denotes the readout weight. Reprinted with permission from Ref. [108]. Copyright (2023) Wiley-VCH GmbH. (d) Schematic and optical images of $LiCoO_2$-based redox-ion gating reservoir (IGR), cross-sectional SEM micrograph of a $LiCoO_2$ redox-IGR, and depiction of insertion (desertion) of Li^+ ions in (104) oriented $LiCoO_2$. (e) Reservoir computing with physical masking. (f) Reservoir state waveforms ($X_1, X_2\ldots, X_{20}$) w/o and w/ physical masking. Reprinted with permission from Ref. [110]. Copyright (2023) Springer Nature.

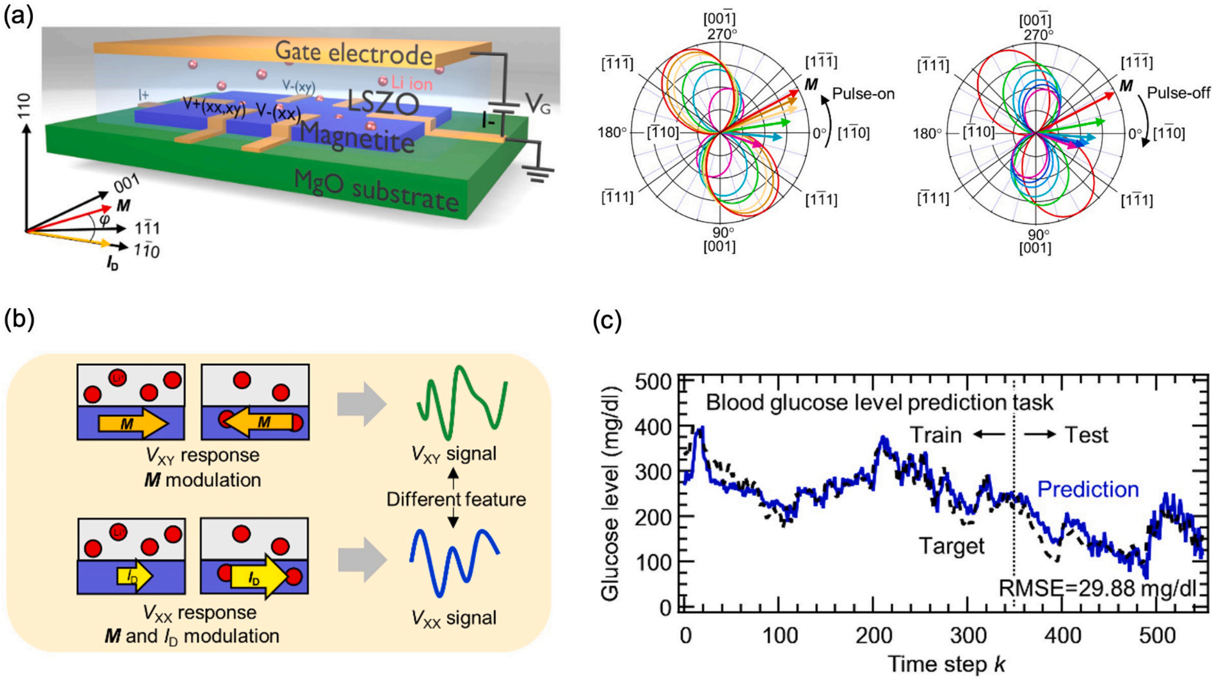

Fig. 21. (a) Schematic illustrations of (left) magnetization angle rotation ion-gating reservoir and (right) magnetic anisotropy and magnetization angle. φ is defined as the relative angle between the electric current I_D and magnetization M. (b) Schematic illustration of V_{XY} (magnetization) and V_{XX} (drain conductance) responses to a pulsed voltage. (c) Target waveform of blood glucose level and waveform predicted with a magnetization angle rotation ion-gating reservoir. Black and blue solid lines denote target and predicted waveforms, respectively. Reprinted with permission from [114]. Copyright (2024) American Chemical Society. (For interpretation of the references to colour in this figure legend, the reader is referred to the web version of this article.)

original input waveform to make a masked input waveform [111]. Although it can improve PRC performance, generating masked input requires the input waveform to be processed with computation resources. In contrast, as illustrated in Fig. 20 (e), the mask waveform is directly applied to the drain electrode as the drain voltage in the physical masking, and additional information processing becomes unnecessary. Fig. 20 (f) compares reservoir states with and without physical masking. As evidenced in the right panels which show measurements made under physical masking conditions, the method provides diverse outputs in spite of its simplicity. The normalized mean square error for the second-order dynamic equation was reduced by as much as 60 % from that without physical masking.

Redox-based ion-gating transistors with Li^+ ion and electron mixed conducting Fe_3O_4 can manipulate magnetic properties, including the magnetization angle [112,113]. In particular, a redox transistor consisting of electron and Li^+ ion mixed conducting Fe_3O_4 ferrimagnet and Li^+ ion conducting Li-Si-Zr-O amorphous electrolyte thin film was applied to PRC. The transistor is schematically shown in Fig. 21 (a) [114]. Fe_3O_4 has an inverse spinel structure with two Fe sites (16d octahedral site and 8a tetrahedral site), of which the oxidation state is electrochemically reduced by Li^+ ion and electron insertion through a topotactic reaction. It modulates magnetic anisotropy energy in Fe_3O_4, thereby manipulating the magnetic angle of Fe_3O_4, as shown in the right panels of Fig. 21 (a). The two dynamic behaviors were utilized as computing resources to obtain reservoir states since electric conductivity modulation in Fe_3O_4 occurs in addition to the magnetic angle rotation, as shown in Fig. 21 (b). The transistor was used to predict blood glucose level fluctuations for a diabetic patient [114]. Fig. 21 (c) compares target and predicted 15-min-ahead fluctuations in blood glucose level; here, the redox transistor-based PRC accurately predicted blood glucose fluctuations with a root mean square error (RMSE) of 29.88 mg/dl, which is lower than that of PRC based on carbon nanotubes (47.0 mg/dl) [115]. Since nanoionic phenomena have diverse and complex dynamics, they have been used in combination with various physical and chemical systems for PRC [116–119].

4.3. Artificial vision device

Optical illusions caused by lateral inhibition play an important role in human visual information processing. The human eye can naturally correct the brightness, colour, and shape of the images it captures, which in turn helps the brain to process visual information efficiently [120]. Its ability to increase the edge contrast between darker and lighter areas is particularly important, because it facilitates clearer recognition of colors and shapes. Visual lateral inhibition takes place in the retina [121]. The retina is a multilayered structure containing hundreds of millions of neurons. Photoreceptors convert the incident light into electrical signals, which are passed on to ganglion cells in the third retinal layer before traveling through the optic nerve to the brain. During this process, horizontal cells and bipolar cells in the second retinal layer produce lateral inhibition [122]. The horizontal cells strengthen or weaken the electrical signals received from the photoreceptors and transmit them to bipolar cells.

An artificial-vision device has been developed based on solid-state ionics that was capable of creating the optical illusion of enhanced edges and contrast [123]. The device consisted of a LiPON electrolyte with a series of LCO channels arranged on it at regular intervals, with the sides of each channel connected to Pt electrodes, as illustrated in Fig. 22 (a). This device structure mimics the structure of connections between photoreceptors, horizontal cells, and bipolar cells in the second retinal layer, as illustrated in Fig. 22 (b). A voltage pulse was applied to one electrode and the current was measured at the opposite electrode. The input voltage corresponded to the electrical signal from the photoreceptors, and the output current corresponded to the response of the

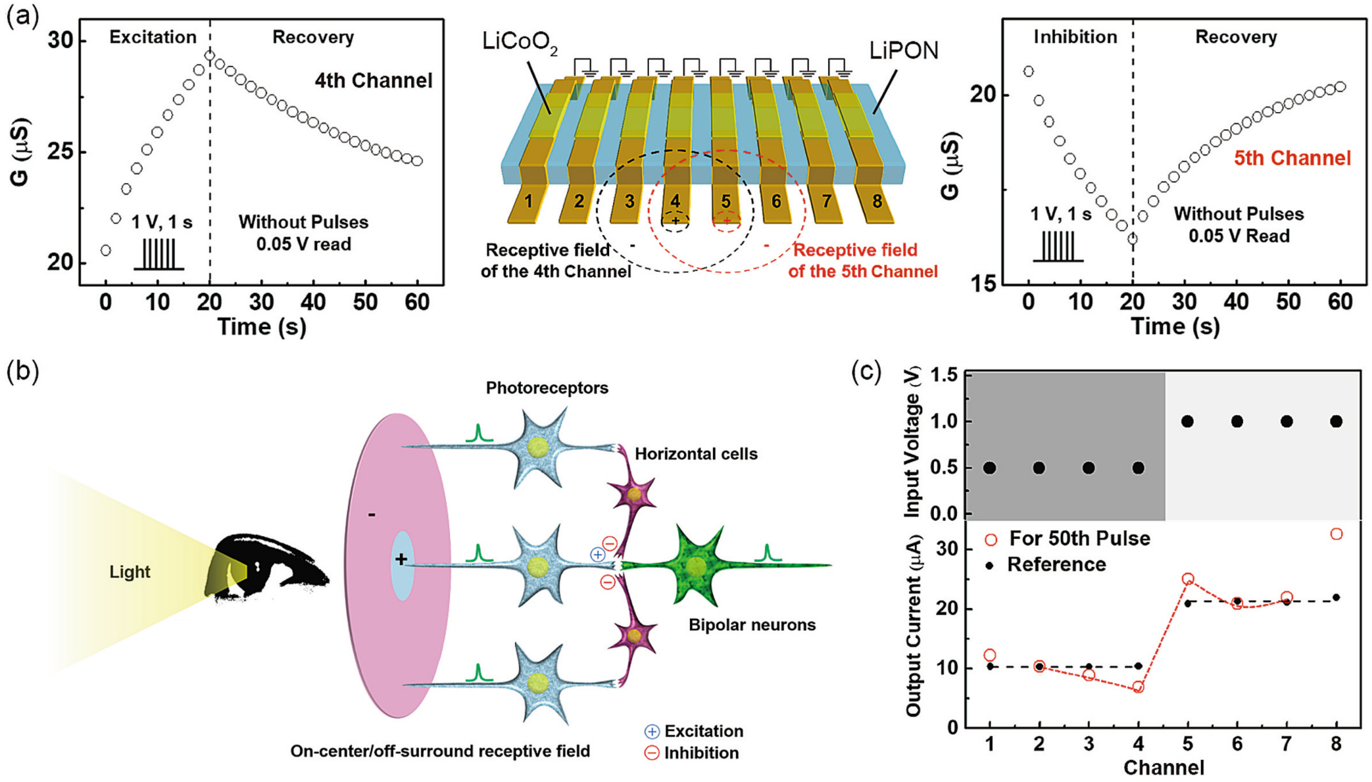

Fig. 22. Lateral inhibition in multi $LiCoO_2$ channels arranged on a common LiPON electrolyte film. (a) Excitation of one channel and inhibition of a neighboring channel by applying voltage pulses. (b) Schematic diagram of an on-center/off-surround receptive field in the retina consisting of photoreceptors directly and indirectly connected via horizontal cells to a bipolar cell. (c) Implementation of the Mach band effect by a device with eight channels. Reprinted with permission from Ref. 123. Copyright (2021) American Chemical Society.

bipolar cells. When positive voltage pulses were applied to one channel, they drove the positively charged Li^+ ions out of the stimulated LCO channel, resulting in a decrease in the Li^+ ion concentration in the channel and an increase in the channel conductance, as shown in the left graph of Fig. 22 (a). The increased conductance emulated the excitation of a bipolar cell when light illuminates the directly connected photoreceptor. On the other hand, the conductance of a neighboring channel decreased because Li^+ ions were driven into the channel. This decreased conductance mimicked the inhibition of a bipolar cell when light illuminates an indirectly connected photoreceptor, as shown in the right graph of Fig. 22 (a). After inputting voltage pulses, the conductance of the excited and inhibited channels returned slowly to the initial state in accordance with the chemical potential gradient. This action corresponded to the recovery process of cells after excitation and inhibition.

Fig. 22 (c) shows the results of applying 50 low voltage pulses to channels 1 to 4 and high voltage pulses to channels 5 to 8 of the device with eight channels shown in Fig. 22 (a). After the pulse applications, the channel current ratio increased at the boundary between channels 4 and 5, giving rise to an enhancement of the edge contrast. Since the spatial response when the voltage pulses were input to each channel corresponds to the overlap of the on-center/off-surround receptive fields, the difference in channel current was large at the edge of the input voltage pattern. This contrast enhancement reproduces the Mach band effect, in which the boundary appears to be emphasized by a difference in brightness [124]. This result indicates that the developed ionic device created an optical illusion in the same way as the human eye does.

To verify the image processing capability of this artificial vision device, an image edge detection simulation was performed on a two-dimensional (2D) array of LCO channels embedded vertically in a LiPON film with individual channels sandwiched between Pt electrodes, as illustrated in Fig. 23. The input image was divided into N × N pixels, and the gray intensity of each pixel was mapped proportionally to the amplitudes of the voltage pulses that were input to the corresponding electrodes at one side of the 2D channel array. Then, the amplitude of the output current from the electrodes on the other side of each channel was mapped proportionally to the gray intensity of the corresponding pixel in the output image. The image on the left in Fig. 23 shows an input grayscale image, while image on the right is the output image obtained after inputting five voltage pulses into the 2D array. To better understand this result, the output image was binarized. The output image (right image) shows that the contours were clearly extracted. In particular, the contours of the woman's hair, which are difficult to distinguish in the input image, are clearly visible. This result was obtained simply by using the characteristics of the solid-state ionics devices and without the use of software and/or complicated circuits like a silicon retina [125,126]. Moreover, intensification of stimuli caused by lateral inhibition is known to occur in the other human senses, i.e., hearing, touch, smell, and taste. This means that the above-described device concept can be applied to hardware implementations of not only visual processes, but also auditory, olfactory, and tactile processes.

5. The wide range of properties and functions of solid-state ionic devices

Physical properties and electronic functions are inherent to the electronic structures of materials, particularly those near the Fermi level. In particular, defect chemistry using chemical doping or tuning of nonstoichiometry properties has been used to manipulate the properties of materials for various purposes. While such defect chemistry is useful on bulk materials, the resulting properties are not tunable, which restricts their applications. On the other hand, dynamic (in situ) tuning of physical properties by using nanoionic phenomena, such as the electric double layer and redox mechanisms, and the device structure shown in Fig. 2 is a novel way of electronic control carriers and develop devices with tunable properties and functions [16,18,127].

5.1. Variable resistance

The all-solid-state electric double-layer transistor (EDLT) shown in Fig. 24 (a) is composed of an oxygen ion-conducting Gd-doped CeO_2 (GDC) solid electrolyte and a $SrTiO_3$ single crystal [128]. $SrTiO_3$ is an insulator that can become a superconductor by injecting electron carriers in an EDLT using liquid electrolytes (ionic liquids) [129]. It is known that divalent positively charged oxygen vacancies conduct inside GDC and generate an oxide ion current [130–132]. By applying of a positive gate voltage to the EDLT, the $SrTiO_3$ is doped with a high density of electron carriers through the formation of an electric double layer of oxygen vacancies and electrons at the $SrTiO_3$/GDC interface. As shown in the I_D-V_G characteristics in Fig. 24 (b), a rapid decrease in electrical resistance with significant hysteresis occurs when charging and discharging the electric double layer, while the pinch-off characteristics similar to those of MOS transistors appear in the I_D-V_D characteristics. Although this device operated well only at high temperatures (473 K) due to the low ion conductivity of GDC at room temperature, it proved that EDLT operation is possible even with solid electrolytes. Moreover, as room-temperature (RT) operation was challenging for oxygen ion conductors, an EDLT was made using a lithium-ion conducting $LiSi_4O_4$ (LSO) amorphous solid electrolyte and $SrTiO_3$ single

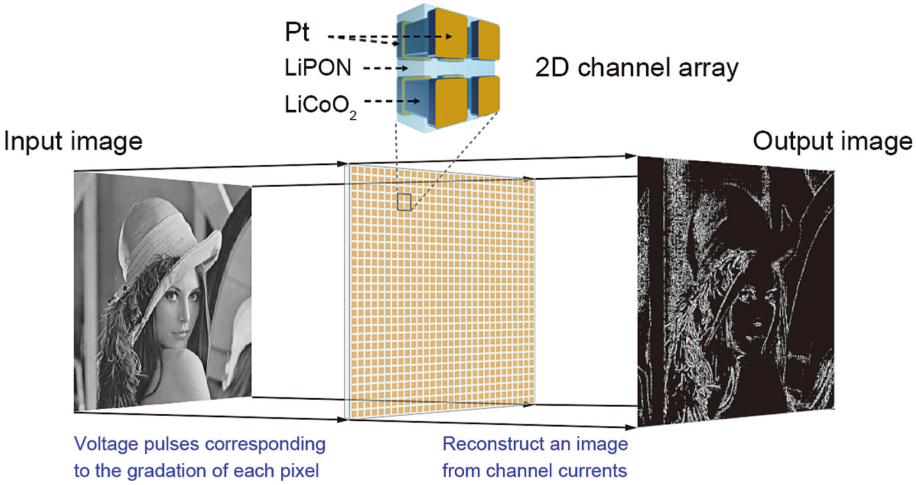

Fig. 23. Schematic illustration of edge detection in an image simulated using the characteristics of a 2D channel array of ionic devices. Excitation and inhibition of each channel are modeled on the basis of the characteristics shown in Fig. 22(a).

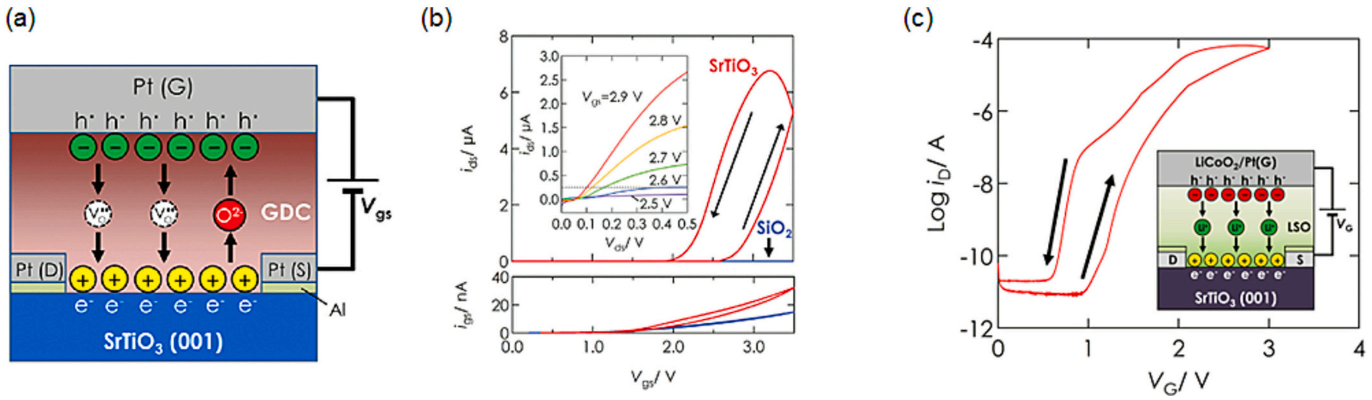

Fig. 24. (a) Schematic illustration of STO-based EDLT using GDC oxide ion conductor and STO single crystal. Yellow and green circles indicate positive and negative charges accumulated at interfaces through oxide ion and vacancy migration. O^{2-} and Vö show negative oxide ion and the positive vacancy, respectively. (b) i_{ds} vs. V_{gs} (upper panel) and i_{gs} vs. V_{gs} (lower panel) characteristics of STO-based EDLT measured at 473 K in air (red lines). For comparison are shown results for a SiO_2-based EDLT consisting of a SiO_2 substrate and GDC oxide ion conductor (blue lines). The inset depicts i_{ds} vs. V_{ds} characteristics for various V_{gs}. Reproduced with permission. [128] Copyright 2013, AIP Publishing. (c) Electrical conduction characteristic (i_D vs. V_G) of STO-based EDLT with $LiSi_4O_4$ electrolyte measured at RT in vacuum. Reprinted with permission. [133] Copyright (2015), AIP Publishing. (For interpretation of the references to colour in this figure legend, the reader is referred to the web version of this article.)

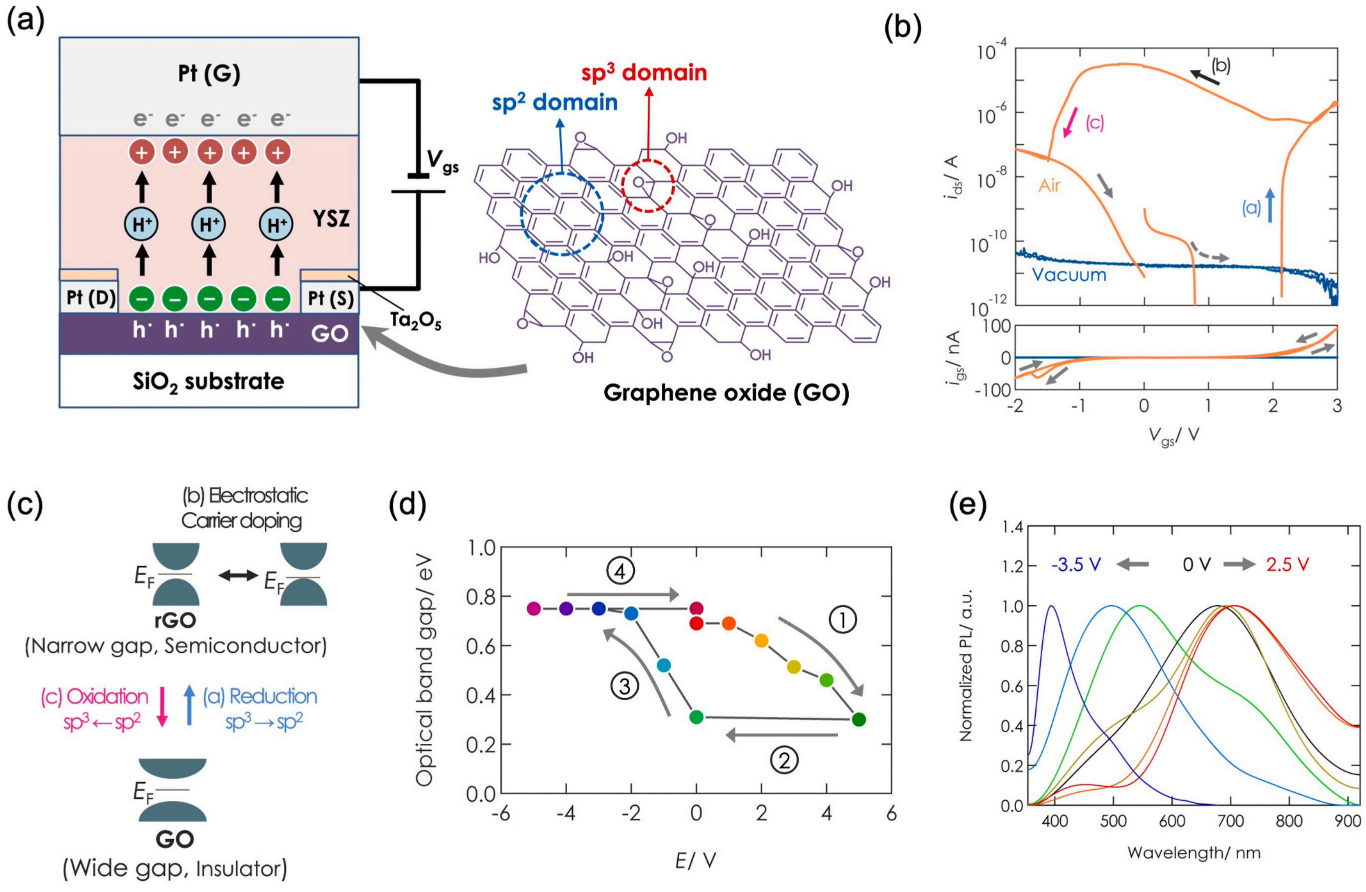

Fig. 25. (a) Schematic illustration of GO-based EDLT with YSZ proton conductor. Brown and green circles represent positive and negative charges accumulated at interfaces due to proton migration. H^+ symbols represent positively charged protons. (b) Electrical conduction characteristics of GO-based EDLT measured in air and vacuum: i_{ds} vs. V_{gs} (upper panel) and i_{gs} vs. V_{gs} (lower panel). Sweep rate of V_{gs} was 4 mV/s; V_{ds} was 0.5 V. (c) Illustration of electrostatic carrier doping (ECD) by EDL charging/discharging and bandgap tuning (BGT), corresponding to a redox reaction, of GO. (d) DC bias dependence of optical band gap tuned by the device. Reprinted with permission from Ref. [134] by The Author(s) licensed under CC BY 4.0, published by Wiley. (e) DC bias dependence of normalized photoluminescence (PL) spectra tuned by application of various DC bias voltages. Reprinted with permission from Ref. [139]. Copyright (2015) American Chemical Society. (For interpretation of the references to colour in this figure legend, the reader is referred to the web version of this article.)

crystal [133]. As shown in Fig. 24 (c), wide tuning of electronic conduction was demonstrated in the $SrTiO_3$ channel at RT because of the relatively high conductivity of the lithium ion conducting solid electrolytes.

5.2. Band gap and fluorescence wavelength tuning

An EDLT using nanoparticle-type Y-stabilized ZrO_2 (YSZ) thin films as the electrolyte was developed for demonstrating proton-conducting solid-electrolyte nanoionic transistors [134]. Fig. 25 (a) shows a schematic diagram of this EDLT. While bulk-crystalline YSZ is an excellent oxygen ion conductor at high temperatures [1], the nanoparticle-type YSZ exhibits extremely high proton conductivity even at room temperature because it can utilize adsorbed water on the nanoparticle surface as a proton source and conduction path [135–138]. By using this thin film, a nanoionics-based transistor that operates at room temperature can be fabricated. In particular, graphene oxide is used as its semiconductor channel. Graphene has the advantage of having a Dirac cone-type electronic structure and high electron mobility, but its lack of a bandgap results in an ON/OFF ratio that is only a few times higher than that of the off state. In contrast, by using graphene oxide, an ON/OFF ratio that is several orders of magnitude higher can be achieved. As shown in Fig. 25 (b), the electric double layer effect near the YSZ/graphene oxide interface enabled continuous drain current changes of approximately two orders of magnitude through electrostatic carrier injection. Furthermore, the band gap of graphene oxide is affected by the ratio of sp^2 regions and sp^3 regions formed by bonding with oxygen (the sp^2/sp^3 fraction). By converting the sp^2 regions and sp^3 regions in graphene oxide through redox reactions driven by the application of a high voltage, the band gap could be controlled in situ (Fig. 25 (c)). The optical bandgap observed by UV–Vis-NIR reflectance measurements varied widely between 0.30 and 0.75 eV over the applied voltage range of −5 to 5 V (Fig. 25 (d)). Furthermore, it was possible to control the wavelength of the fluorescence emitted by oxidized graphene over a wide range from 712 to 393 nm (Fig. 25 (e)) [139]. These results show that, by utilizing electrolytes with high ion conductivity at room temperature, it is possible to control material properties in situ through the use of electric double layers or redox reactions at room temperature.

5.3. Variable superconducting transition temperature

Nanoionics-based transistors can control the electronic properties of not only semiconductors but also metals by doping material with electronic carriers at a high density. Fig. 26 (a) shows a schematic diagram of an EDLT composed of a lithium-ion-conductive LSO amorphous thin film and metallic Nb (110) film behaving as a strong coupling superconductor, in which its superconducting transition temperature T_c increases with carrier density in accordance with standard BCS theory [133]:

$$T_c = 1.14\frac{h\omega_D}{2\pi k_B}\exp\left(-\frac{1}{D(0)V}\right) \tag{3}$$

Here, D (0) and V are the density of states (DOS) near the Fermi level and the electron-phonon interaction, respectively. By applying a gate voltage, it is possible to dope Nb with a high charge density of electrons or holes through the electric double layer formed at the Nb/LSO interface. Therefore, it is considered possible to control the critical temperature of superconductivity T_c by using carrier doping from the electric double layer. Fig. 26 (b) shows the gate voltage dependence of T_c in the EDLT. T_c increased from 8.33 to 8.39 K when the gate voltage was reduced from 2.5 to −2.5 V. The T_c variation was almost three orders of magnitude larger than the values reported for electrostatic carrier doping using conventional solid dielectrics, indicating that the EDLT could modulate a much higher carrier density. The specific difference in $T_{c,\ onset}$ for the applied gate voltage was 12 mK/V, which is 33 % larger than the value reported for an ionic-liquid-based EDLT [140]. This result indicates that the same electric double layer effect as with liquid electrolytes can be achieved with solid electrolytes.

5.4. Tuning magnetic properties

Devices having an ion-electron mixed conducting host matrix can use topotactic reactions for high-density ion insertion and desertion (Fig. 2 (e)). This property has been used to tune the magnetic properties of electron-Li^+ ion mixed conducting ferrimagnet Fe_3O_4 thin film. Fig. 27 (a) illustrates an all-solid-state redox transistor consisting of (100) oriented Fe_3O_4 thin film grown on MgO (100) single crystal and Li^+ ion conducting Li_4SiO_4 (LSO) amorphous thin film [112]. By applying a positive gate voltage, many Li^+ ions and electrons are injected into the Fe_3O_4 through a topotactic reaction. The Fe_3O_4 has an inverse spinel structure with two Fe^{3+} sites: tetrahedral (A) and octahedral (B). Li^+ ion and electron insertion cause electrochemical reduction of the Fe^{3+} at the B sites to Fe^{2+} with minority down spins. This in turn decreases the total spin and enables tuning of the magnetization of Fe_3O_4 over a wide range, as shown in Fig. 27 (b). Since the variation in down spins tunes the spin polarization (P) in Fe_3O_4, the device can tune the magnetoresistance

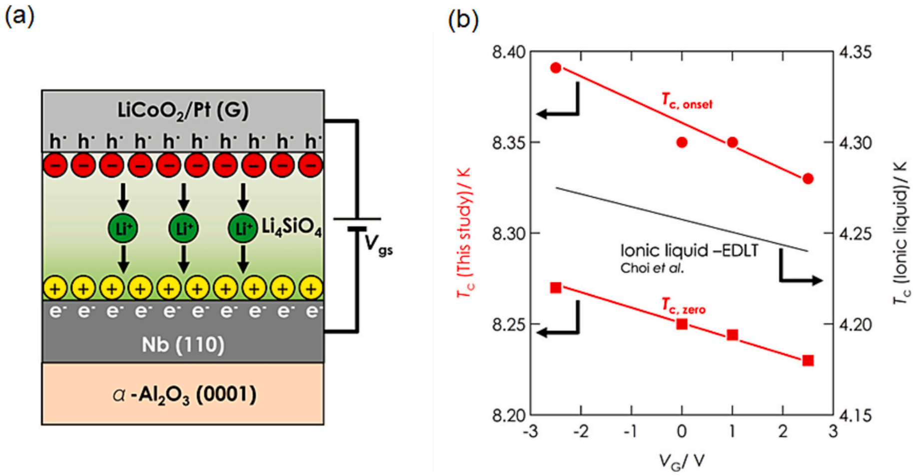

Fig. 26. (a) Schematic illustration of Nb-based EDLT composed of LSO Li^+ ion conductor and LCO gate electrode. Yellow and red circles represent positive and negative charges accumulated at interfaces due to Li^+ ion migration. (b) Variation in superconducting transition temperatures ($T_{c,onset}$ and $T_{c,\ zero}$) plotted with respect to V_G. Reprinted with permission from Ref. [133] Copyright (2015), AIP Publishing. (For interpretation of the references to colour in this figure legend, the reader is referred to the web version of this article.)

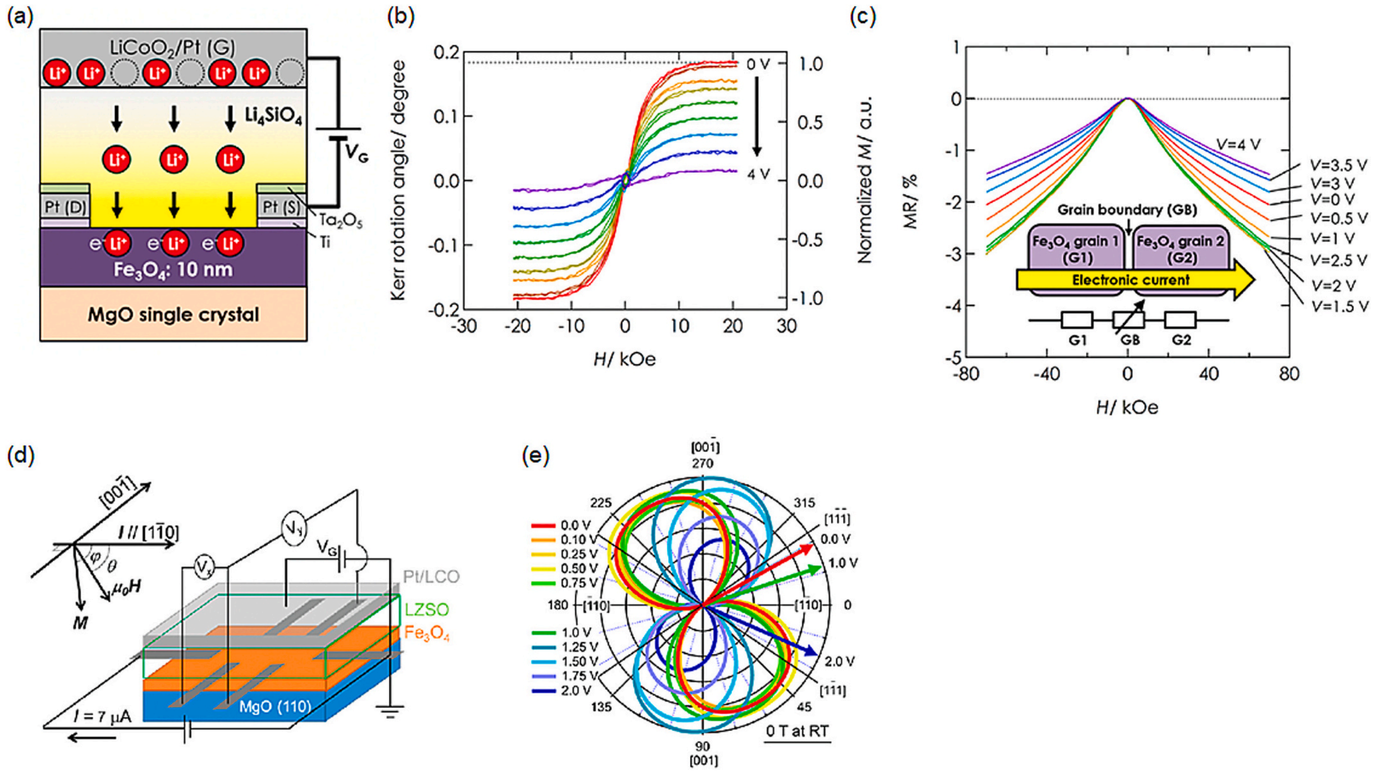

Fig. 27. (a) Schematic illustration of all-solid-state redox transistor with Fe_3O_4 and LSO lithium ion conductor. Li^+ symbol represents positively charged lithium ions. Dotted circles in $LiCoO_2$ represent Li^+ ion vacancies. (b) *M-H* loops measured at various DC voltages. (c) DC voltage dependence of MR in Fe_3O_4 thin film as a function of magnetic field (−70 to 70 kOe) at 250 K. Reprinted with permission from [112]. Copyright 2016 American Chemical Society. (d) Schematic illustration of an all-solid-state redox transistor and its configuration in a planar Hall measurement. V_x and V_y denote nano-volt meters for measuring longitudinal and transverse resistance. (e) Polar graph of MAF (magnetic anisotropy field) at various V_G. The red, yellow-green, and blue arrows show the magnetization directions at $V_G = 0.0$, 1.0, and 2.0 V, respectively. Reprinted with permission from Ref. [113]. Copyright (2020) American Chemical Society. (For interpretation of the references to colour in this figure legend, the reader is referred to the web version of this article.)

(MR) of Fe_3O_4. Here, MR is defined as $(R(H)-R(0))/R(0)$, where $R(H)$ and $R(0)$ are the resistance with a magnetic field, H, and the resistance without a magnetic field, respectively. MR in Fe_3O_4 thin film is attributed to spin-dependent tunneling or scattering through the Fe_3O_4 grain boundaries. As shown in Fig. 27 (c), tuning of the spin polarization enabled tuning of the magnetoresistance, which is a process that can be applied to spintronics-based resistive switching.

The topotactic reaction mechanism can be also used to tune the magnetization angle of magnetic materials, which is difficult to control at RT. Fig. 27 (d) shows a schematic illustration of an all-solid-state redox transistor consisting of electron-Li^+ ion mixed conducting and ferrimagnetic Fe_3O_4 (110) thin film and Li^+-ion conducting Li-Zr-Si-O (LZSO) amorphous film. To detect the magnetization angle, the transistor was designed to utilize the planar Hall (pH) effect [113]. A polar graph of the magnetic anisotropy field (MAF) measured under various gate voltage conditions is shown in Fig. 27 (e). Here, by inserting Li^+ ions and an electrons into the Fe_3O_4 thin film, the magnetization angle rotated by 56° at maximum. The combination of excellent tunability with low operating power (10^{-3} J/cm^2) is a great advantage of the nanoionics approach [113].

5.5. *Learning and decision making*

Ionic devices have been used to mimic the ability to learn and make decisions. These devices are called ionic decision-makers because they make decisions by utilizing nanoionics phenomena caused by ion transport in a solid electrolyte [141]. An ionic decision-maker efficiently solved a mathematical problem called the multi-armed bandit problem (MBP), which is the problem of finding the best choice among multiple alternatives (arms) through trial-and-error. The problem is typically illustrated as selecting the slot machine that maximizes profits from among multiple slot machines with different reward probabilities (Fig. 28 (a)). It is a fundamental problem in reinforcement learning and appears in a wide range of modern social activities (information communication, manufacturing, economics, medicine, entertainment, etc.). In the study, MBP in wireless communications was chosen and conducted to make optimal action selections to maximize the communication volume while avoiding losses by adapting to changing conditions in a congested communication network (Fig. 28 (b)).

Fig. 28 (c) is a schematic illustration of the ionic decision-maker; it consists of a solid electrochemical cell with platinum electrodes attached to a polymer solid electrolyte called Nafion, which is a good proton conductor. When sequential pulsed currents are applied to the device, electrochemical phenomena (electric double layer charging, redox reactions, etc.) accompanying transport of protons in Nafion occur near the electrode interface, resulting in temporal modulation of the voltage (electromotive force) of the cell, as shown in Fig. 28 (d). By utilizing this voltage modulation as a computation resource, the ionic decision-maker can quickly learn and make appropriate decisions. Furthermore, the experimenters skillfully utilized the current-voltage characteristics of the solid electrochemical cell to give the device the ability to adapt to changing conditions by emphasizing (weighting) new experiences. The operation principle of the ionic decision-maker is based on a mathematical model called the Tug-of-War principle, which was originally derived from observations of the spatiotemporal dynamics of feeding amoeba under a volume conservation condition [142], as schematically shown in Fig. 28 (e).

The performance of the ionic decision-maker was assessed by

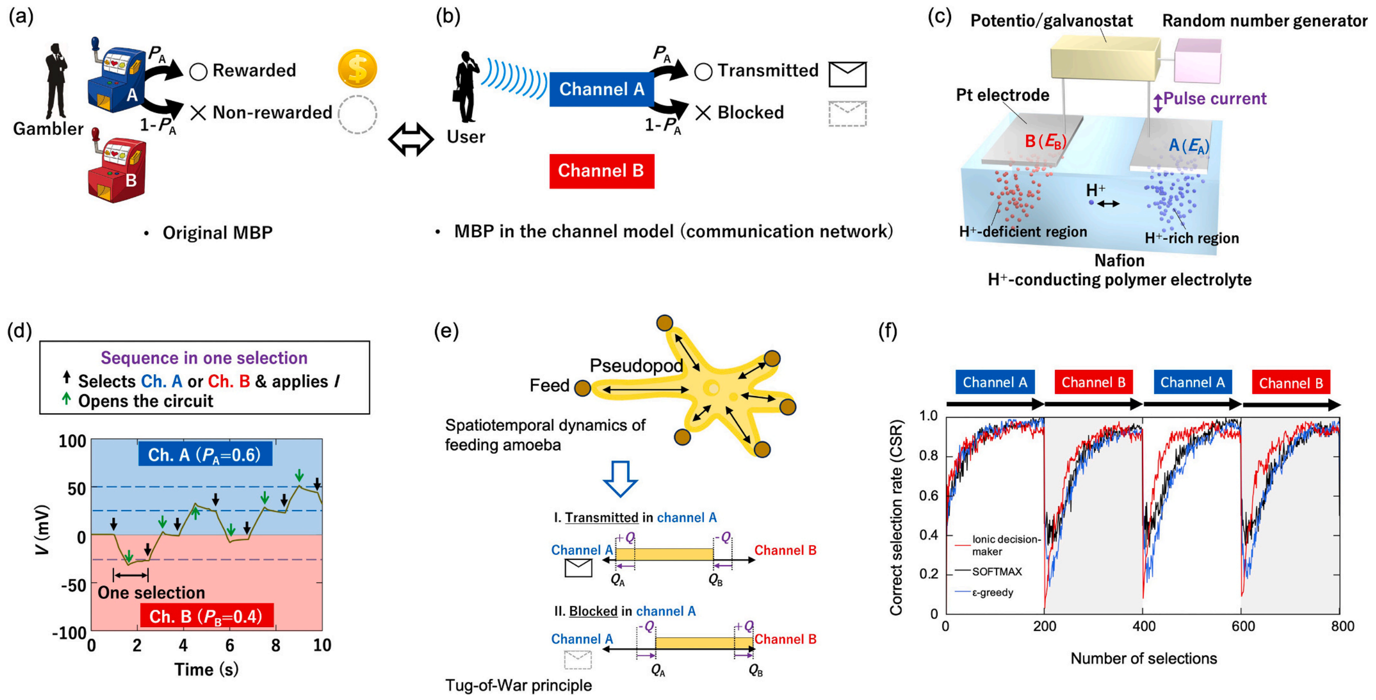

Fig. 28. (a) Original MBP, in which a gambler attempts to select a slot machine. (b) MBP in a channel model in which a communication network user attempts to select an available channel. (c) Illustration of experimental setup using a two-terminal electrochemical cell, potentio/galvanostat, and a random number generator. (d) Variation in cell voltage during the experiment. (e) Schematic illustrations of spatiotemporal dynamics of amoeba and the Tug-of-War principle. (f) Comparison of performance of ionic decision-maker, SOFTMAX, and ε-greedy algorithms in solving a dynamic MBP under the initial condition (P_A, P_B) = (0.6, 0.4). Reproduced with permission from Ref. [141]. Copyright (2018) American Association for the Advancement of Science.

comparing its solutions of the MBP with those conventional computer calculations using the SOFTMAX and ε-greedy algorithms [141]. These conventional algorithms perform complex calculations, but, as shown in Fig. 28 (f), the ionic decision maker performed comparably in terms of the asymptotically increasing correct response rate and adaptive behavior, despite its simple operation consisting of applying a pulse

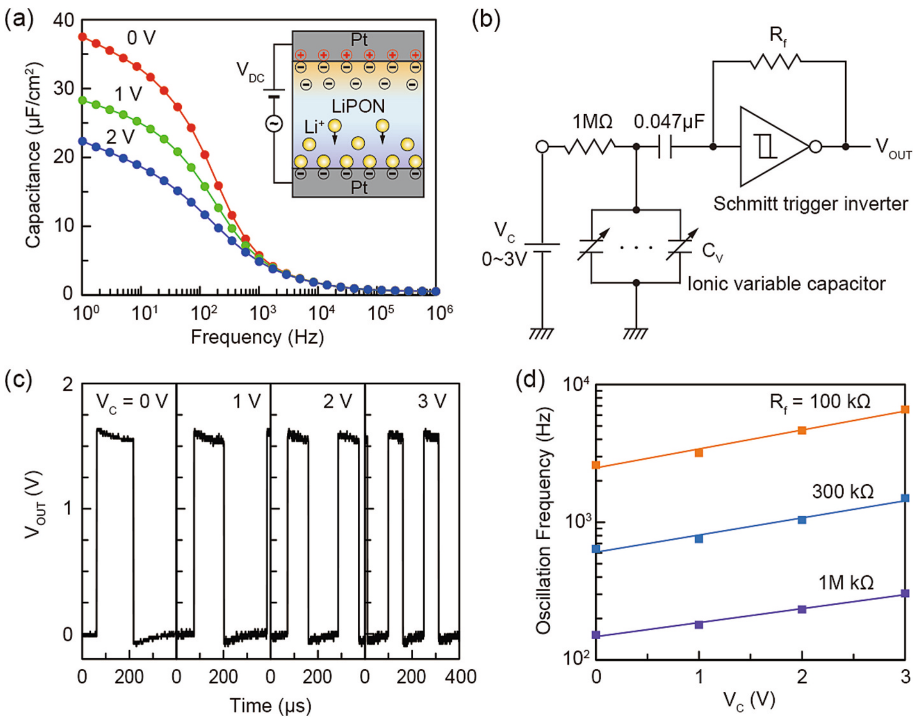

Fig. 29. (a) Variable capacitance demonstrated by a Pt/LiPON/Pt capacitor. The inset illustrates operation under application of V_{DC}. (b) VOC composed of a Schmitt trigger inverter and Pt/LiPON/Pt capacitors. (c) Typical output waveforms V_{OUT} obtained for different V_C at 50 °C with 4 Pt/LiPON/Pt capacitors. (d) Oscillation frequency plotted as a function of V_C with different feedback resistance values of R_f. Reprinted with permission from Ref. 150. Copyright (2020) American Chemical Society.

current and measuring a voltage. The solid-state electrochemical cell of the ionic decision-maker acts as both a memory for storing experiences and an arithmetic unit for processing experiences, which is a kind of in-memory computation. Besides the ionic decision-maker, atomic switches and other nanoionic devices have been used to solve problems embodying the Tug-of-War principle [142–146].

5.6. *Variable capacitance*

An EDL formed at an electrode/electrolyte interface can also be used as a variable capacitor, whose capacitance can be changed by applying a bias voltage. An EDL capacitor (called an energy storage device) was first commercialized around 1970 by using Ag^+-ion conducting $RbAg_4I_5$ and Ag and C electrodes [1]. When a voltage of negative polarity was applied to the Ag electrode, the Ag ions in the $RbAg_4I_5$ were transported to and precipitated at the $Ag/RbAg_4I_5$ interface through a reduction reaction. At the interface between the C and $RbAg_4I_5$, Ag ion vacancies (negative charge) formed and positive charges accumulated to form an EDL. Variable capacitance has also been observed in different Na ion conducting glasses sandwiched between Pt electrodes under DC bias voltage. This is attributed to the formation of an EDL at the metal/solid electrolyte interfaces [147,148]. The capacitance of the EDL at a metal/ion conductor interface can be explained by the behavior of discrete ion charges that interact strongly with the metal surface [149].

Variable capacitance in Pt/LiPON/Pt structures, with LiPON thicknesses ranging from 15 to 60 nm, has been demonstrated [150]. Fig. 29 (a) plots typical capacitance variations versus frequency of a capacitor with a 15-nm-thick LiPON film. The measurements were carried out at a V_{DC} of 0, 1, or 2 V at RT. Analyses with an equivalent circuit model revealed that the relatively flat capacitance at low frequencies originates from the formation of an EDL of Li^+ ions at both the Pt/LiPON and LiPON/Pt interfaces. The capacitance decreases with increasing V_{DC}. Applying a voltage drives the Li^+ ions from the positively biased Pt electrode to the negatively biased Pt electrode. At higher voltages, the number of Li^+ ions at the positive electrode decreases to zero (inset of Fig. 29 (a)). This causes the positive electrode's contribution to the total capacitance to vanish at some bias voltage. As a result, similarly to what occurs in a varactor diode, the capacitance decreases as the bias voltage increases.

Voltage-controlled oscillator (VCO) operation was demonstrated using Li^+-ion EDL capacitors made from LiPON film. The VCO circuit was constructed using a Schmitt trigger inverter and a resistance-capacitor (RC) oscillator with LiPON capacitors, as illustrated in Fig. 29 (b). The oscillation frequency of the output waveform V_{OUT} is given by $1/2pR_fC_V$, where C_V is the total capacitance of the LiPON capacitors and R_f is the resistance of the feedback resistor. The parameter for determining the oscillation frequency is C_V, which can be changed by varying the temperature and the number of parallel connections of the LiPON capacitors. Fig. 29 (c) shows V_{OUT} variations obtained with four LiPON capacitors at 50 °C and $R_f = 100$ kΩ under application of a control voltage V_C ranging from 0 to 3 V. Fig. 29 (d) plots oscillation frequency variations as a function of V_C for different values of R_f. The frequency change is exponentially proportional to V_C, which is the same as in a VCO that uses a varactor diode instead of LiPON capacitors. Although the upper limit of the oscillation frequency is much lower than that of the varactor diode-based VCO, it can be extended by using dielectric electrolyte films with higher ion conductivity. The simplicity of the device structure and the ease by which it can be fabricated make the solid electrolyte-based EDL capacitor a good candidate as a building block in analog and mixed signal electronic circuits.

6. Atomic layer deposition for making high-quality ion-conductor thin films

Thin ion conductor films are very important components of ion batteries and fuel cells as well as essential parts of nanoionic electronic and information technology devices. Radio-frequency sputtering and pulsed laser deposition are used to produce solid electrolyte films. However, it is difficult to use these techniques to deposit uniform thin films on three-dimensional (3D) microbatteries and integrated circuits. Recently, atomic layer deposition (ALD) has attracted attention as a technique that can fabricate uniform solid electrolyte films with no pinholes on complex structures with atomic-level precision [151]. The historical development of ALD for Li^+ ion conducting solid electrolytes does not stretch far back in time. The first report on ALD deposition of LiPON was published by a research group from University of Maryland in 2015 [152]. The team succeeded in fabricating ALD films of LiPON by using lithium (tert-butoxide) (LiO^tBu) and trimethyl phosphate (TMP) in a N_2 plasma process. Around the same time, a group from Aalto University reported ALD deposition of LiPON [153]. They used thermal ALD to deposit LiPON films by alternately supplying lithium bis(trimethyl) amide (LiHMDS) and diethylphosphorylamide (DEPA). Meanwhile, a group from Panasonic Corp. fabricated LiPON thin films by using thermal ALD with LiO^tBu and tris(dimethylamino)phosphine (TDMAP) [154]. These ALD films showed ionic conductivities of $1.6–6.6 \times 10^{-7}$ S/cm at room temperature, but required relatively high deposition temperatures of 300–500 °C. In order to apply Li-based solid electrolyte thin films to various applications in the future, it will be necessary to use lower deposition temperatures and at the same time achieve higher ionic conductivities.

Recently, lithium phosphate and LiPON films were successfully fabricated by ALD using LiO^tBu and TDMAP with different plasma reactants at low deposition temperatures (220–300 °C) [155]. The X-ray diffraction patterns illustrated in Fig. 30 (a) show that the deposition with O_2 plasma produced a polycrystalline film, while the deposition with NH_3 plasma produced an amorphous film. The AFM image of the film deposited with NH_3 plasma (Fig. 30 (b)) shows a flat surface characteristic of amorphous films. The cross-sectional SEM image (Fig. 30 (c)) shows that NH_3 plasma deposited film uniformly on the sides and bottom of the trench structure, with good step coverage characteristics. Fig. 30 (d) shows the N 1 s core spectra of these films, measured by hard X-ray photoemission spectroscopy (HAXPES). The spectrum of the film deposited with O_2 plasma has no peaks derived from nitrogen, whereas the spectra of the film deposited with NH_3 plasma has an N 1 s peak is clearly separated into components arising from doubly-bound nitrogen (P=N-P) and triply-bound nitrogen ($P\text{-}N < P_2$) [156]. Quantitative HAXPES analyses estimated the composition of the film deposited with O_2 plasma to be $Li_{3.3}PO_{3.4}$. When NH_3 plasma was used, the amount of nitrogen in the film increased. The composition of the film deposited at an NH_3 flow rate of 20 sccm was estimated to be $Li_{2.5}PO_{1.9}N_{0.8}$, corresponding to a nitrogen content of 13 %. Fourier transform infrared spectroscopy (FTIR) spectra from the lithium phosphate film (Fig. 30 (e)) exhibited a peak corresponding to PO_3^{2-} ions in pyrophosphate (P_2O_7). In addition to that peak, spectrum of the LiPON film showed a vibration mode derived from the N-P-O bond as well as one from the P-N-P bond. These results are consistent with the HAXPES results, suggesting that nitrogen became incorporated in the phosphate framework. Moreover, the peak on the low-frequency side that arises from the Li—O bond was broadened by the introduction of nitrogen, indicating that the bonding state around the Li^+ ion was disordered.

The ionic conductivity of the deposited films was evaluated by electrochemical impedance spectroscopy (EIS). Fig. 30 (f) shows Arrhenius plots of the ionic conductivity obtained from an analysis of the EIS results. The lithium phosphate film deposited using O_2 plasma showed an ionic conductivity of 1.75×10^{-9} S/cm at room temperature. This value is similar to the conductivities of reported ALD films and sputtered films [157,158]. On the other hand, the ionic conductivity increased significantly when the film was deposited with NH_3 plasma. It reached 1.65×10^{-6} S/cm at 20 sccm and room temperature. This is the highest conductivity reported for any ALD LiPON film to date. The activation energy (E_a) decreased from 0.91 eV for the lithium phosphate film to 0.66 eV for the LiPON film. This decrease in activation energy

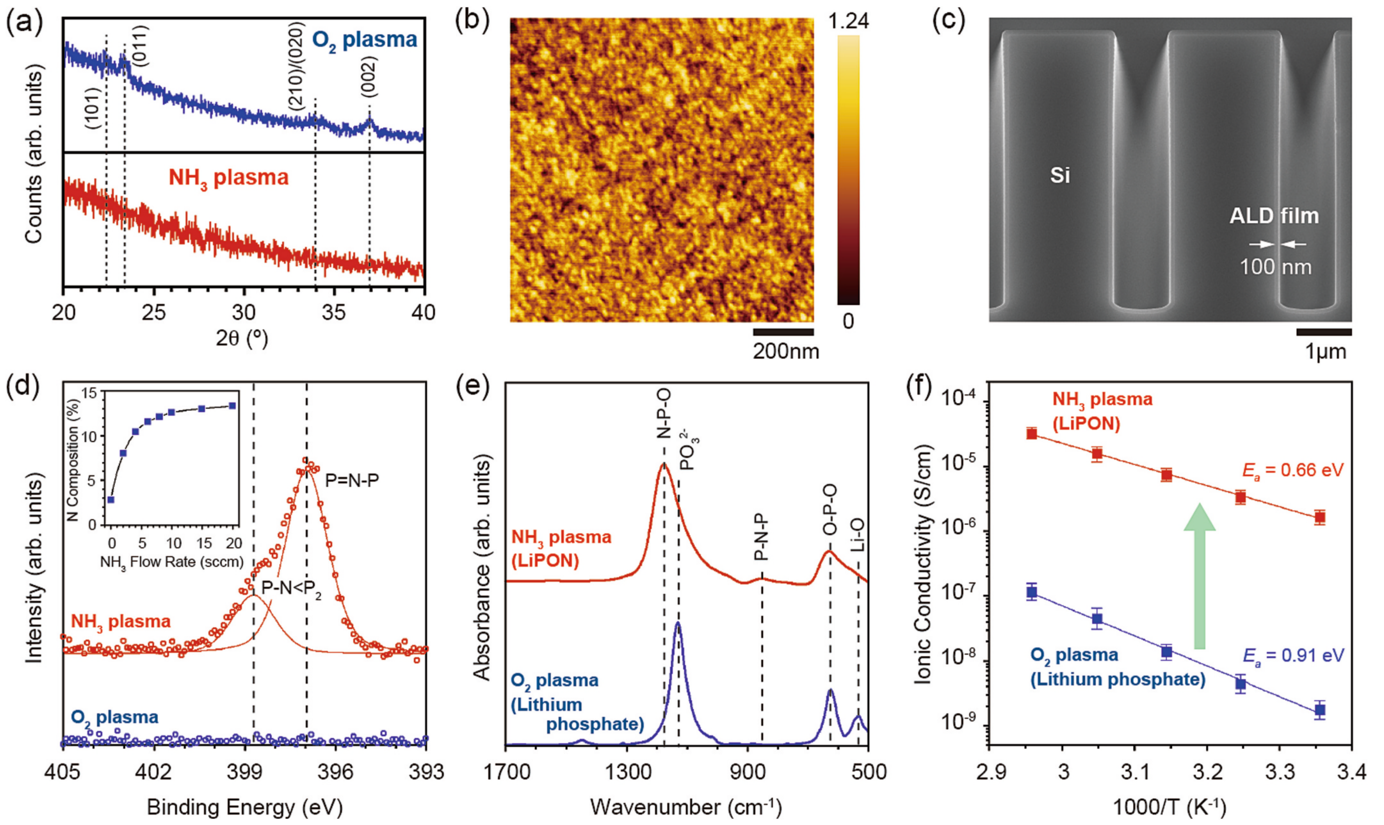

Fig. 30. Structural, morphological and electrical properties of lithium phosphate and LiPON ALD films. (a) XRD patterns of films deposited with O_2 and NH_3 plasma. (b) AFM image of film deposited with NH_3 plasma. (c) Cross-sectional SEM image of film deposited with NH_3 plasma onto a trench structure patterned on a Si substrate. (d) Core-level N 1 s spectra, (e) FTIR spectra, and (f) Arrhenius plots of the ionic conductivity for films deposited with O_2 and NH_3 plasma. Reprinted with permission from Ref. 155. Copyright (2024) American Chemical Society.

indicates that the high Li^+ ion conductivity at room temperature is due to the introduction of nitrogen in the film. On the other hand, a measurement of the direct current polarization indicated that the electronic conductivity of the LiPON film was less than 2×10^{-12} S/cm. Thus, it was concluded that the LiPON film deposited by ALD is an excellent solid electrolyte with high ionic conductivity and low electronic conductivity. The ALD technique has been used to deposit magnesium phosphate and magnesium phosphate nitride and has the potential to be applied to various Li^+ ion solid electrolytes and [159,160]. It is believed that ALD will play an important role in the development of future solid-state nanoionics devices.

7. Conclusion

The development of electronic information devices has so far focused on nanoelectronics that utilize localized electron movements. However, there is growing interest in solid-state ionic devices for their unique capabilities and high performance. Unlike semiconductor devices, ionic devices can manipulate ions and restructure their crystals down to the atomic scale. This ability is inherent to the idea of “ionic nanoarchitectonics,” a field which deals with the development and utilization of ion-based architectures within materials. The techniques of ionic nanoarchitectonics can be used to make ionic devices that exhibit a variety of physical properties and functions, as well as the ability to modify their structure and functionality as needed. This plasticity of device structure is a powerful feature that will encourage the development of diverse devices that push the boundaries of traditional semiconductor technology.

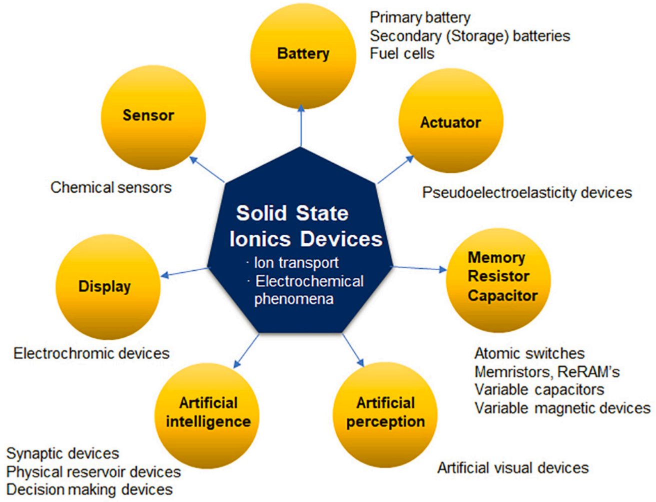

Fig. 31. A variety of functional solid-state ionic devices that operate using ion transport and electrochemical phenomena in solids. Reprinted with permission from Ref. 161. Copyright (2022) American Chemical Society. The Japan Society of Applied Physics.

This review outlined the development of various solid-state ionic devices created through ionic nanoarchitectonics. It highlighted their electrical, magnetic, optical and neuromorphic properties, the latter of which are inspired by the mechanisms of the human brain. Fig. 31 shows representative solid ion devices that have been reported to date, including those that are not covered by this review [161]. Batteries that extract electrical energy fall into two categories: non-rechargeable primary batteries and rechargeable secondary batteries. There are also fuel cells that generate electricity using the chemical energy of fuels and oxidisers. Chemical sensors convert information about changes in substance concentration into electrical signals. Electrochromic displays transmit information by changing colour and brightness. Actuators utilize the force generated by ion transport to create movement. Recently, new ionic electronic information devices have been developed to overcome the performance limitations of conventional semiconductor devices. These include atomic switches, non-volatile memory (ReRAM), variable magnetic devices and variable capacitors. Furthermore, artificial synapses, physical reservoir devices, and artificial visual devices that mimic the functions of brain neurons and decision-making processes have been developed.

We believe that the most interesting challenge in the future application of solid-state ionic devices in electronic information technology will be to create brain-inspired computers using neuromorphic engineering based on the functions of the brain. These small, low-power computers could contribute to the development of high-performance, autonomous humanoid robots. Such robots require various components, including a power source, artificial muscles for movement and artificial senses, such as vision and hearing, to perceive their surroundings. They also require an artificial brain that can learn, make judgements and remember things. We expect these components to be developed using solid-state ionic devices with various functions.

Research in the field of solid-state ionics for electronic information devices is still in its early stages, with many opportunities yet to be explored. For instance, the thickness of ion-conducting membranes used in devices has recently decreased to around 10 nm, resulting in the observation of phenomena that differ from those of conventional ion conduction in solids. However, technologies for repeatedly and consistently controlling ion transport and electrochemical phenomena in nanoscale spaces remain underdeveloped. Additionally, the potential of utilizing fluctuations in analogue electrical signals generated by ionic phenomena at the nanoscale as a new operating principle for devices is a field that is beginning to be investigated. Growing interest among researchers in these unexplored areas indicates anticipated future advancements in electronics and information technology based on solid-state ionics.

CRediT authorship contribution statement

Kazuya Terabe: Writing – review & editing. **Takashi Tsuchiya:** Writing – review & editing. **Tohru Tsuruoka:** Writing – review & editing. **Hirofumi Tanaka:** Writing – review & editing. **Ilia Valov:** Writing – review & editing. **James K. Gimzewski:** Writing – review & editing. **Tsuyoshi Hasegawa:** Writing – review & editing.

Declaration of competing interest

The authors declare that they have no known competing financial interests or personal relationships that could have appeared to influence the work reported in this paper.

Data availability

Data will be made available on request.

References

[1] T. Kudo, K. Fueki, Solid State Ionics, Wilry-VCH Verlag GmbH, Weinhein, 1990.

[2] K. Tada, H. Ikeda, Sanyo's couliodes and memoriodes, in: T. Takahashi, A. Kozawa (Eds.), Applications of Solid Electrolytes, JEC Press, US Office of the Electro-chemical Society of Japan, Cleveland, Ohio, 1980, p. 40.

[3] T. Takahashi, O. Yamamoto, Solid state ionics-the electrochemical analog memory cell with solid electrolyte, J. Appl. Electrochem. 3 (1973) 129–135. https://link.springer.com/article/10.1007/BF00613503.

[4] K. Terabe, T. Hasegawa, C. Liang, M. Aono, Control of local ion transport to create unique functional nanodevices based on ionic conductors, Sci. Tech. Adv. Mater. 8 (2007) 536–542, https://doi.org/10.1016/j.stam.2007.08.002.

[5] R. Waser, M. Aono, Nanoionics-based resistive switching memories, Nat. Mater. 6 (2007) 833–840, https://doi.org/10.1038/nmat2023.

[6] R. Waser, D. Ielmini, H. Akinaga, H. Shima, H.S.P. Wong, J.J. Yang, Introduction to nanoionic elements for information technologyu, in: D. Ielmini, R. Waser (Eds.), Resistive Switching: From Fundamental of Nanoionic Redox Process to Memristice Device Application, Wiley-VCH, Weinheim, Germany, 2016, pp. 1–29, https://doi.org/10.1002/9783527680870.ch1.

[7] T. Hasegawa, K. Terabe, T. Tsuruoka, M. Aono, Atomic switch: atom/ion movement controlled devices for beyond Von-Neumann computers, Adv. Mater. 24 (2012) 252–267, https://doi.org/10.1002/adma.201102597.

[8] K. Terabe, T. Tsuruoka, T. Hasegawa, A. Alpana, T. Ohno, T. Nakayama, M. Aono, Atomic switch, in: D. Ielmini, R. Waser (Eds.), Resistive Switching: From Fundamental of Nanoionic Redox Process to Memristice Device Application, Wiley-VCH, Weinheim, Germany, 2016, pp. 515–545, https://doi.org/10.1002/9783527680870.ch18.

[9] Y. Yang, P. Gao, L. Li, X. Pan, S. Tappertzhofen, S.H. Cho, R. Waser, I. Valov, W. D. Lu, Electrochemical dynamics of nanoscale metallic inclusions in dielectrics, Nat. Commun. 5 (2014) 4232, https://doi.org/10.1038/ncomms5232.

[10] D.H. Kwon, K.M. Kim, J.H. Jang, J.M. Jeon, M.H. Lee, G.H. Kim, X.S. Li, G.S. Park, B. Lee, S. Han, M. Kim, C.S. Hwang, Atomic structure of conducting nanofilaments in TiO_2 resistive switching memory, Nat. Nanotech. 5 (2010) 148–153, https://doi.org/10.1038/nnano.2009.456.

[11] X. Liu, C. Sun, X. Ye, Z. Zhu, C. Hu, H. Tan, S. He, M. Shao, R.W. Ki, Neuromprphic nanoionics for human-machine interaction: from materials to applications, Adv. Mater. 36 (2024) 2311472, https://doi.org/10.1002/adma.202311472.

[12] S.Z. Bisri, S. Shimizu, M. Nakano, Y. Iwasa, Endeavor of iontronics: from fundamentals to applications of ion-controlled electronics, Adv. Mater. 29 (2017) 1607054, https://doi.org/10.1002/adma.201607054.

[13] H. Chun, T.D. Chung, Iontronics, Annu. Rev. Anal. Chem. 8 (2015) 441–462, https://doi.org/10.1146/annurev-anchem-071114-040202.

[14] G. Ding, J. Zhao, K. Zhou, Q. Zheng, S.T. Han, X. Peng, Y. Zhou, Porous crystalline materials for memories and neuromorphic computing systems, Chem. Soc. Rev. 52 (2023) 7071–7136, https://doi.org/10.1039/D3CS00259D.

[15] G. Ding, H. Li, J. Zhao, K. Zhou, Y. Zhai, Z. Ly, M. Zhang, Y. Yan, S.T. Han, Y. Zhou, Nanomaterials for flexible Neuromorphics, Chem. Rev. 124 (2024) 12738–12843, https://doi.org/10.1021/acs.chemrev.4c00369.

[16] K. Terabe, T. Tsuchiya, R. Yang, M. Aono, Nanoionic devices enabling a multitude of new features, Nanoscale 8 (2016) 13873–13879, https://doi.org/10.1039/C6NR00956E.

[17] M. Aono, Y. Bando, K. Ariga, Nanoarchitectonics: pioneering a new paradigm for nanotechnology in materials development, Adv. Mater. 24 (2012) 150–151, https://doi.org/10.1002/adma.201104614.

[18] K. Terabe, T. Tsuchiya, T. Tsuruoka, A variety of functional devices realized by ionic nanoarchitectonics, complementing electronics components, Adv. Electron. Mater. 8 (2022) 2100645, https://doi.org/10.1002/aelm.202100645.

[19] G. Milano, M. Aono, L. Boarino, U. Celano, T. Hasegawa, M. Kozicki, S. Majumdar, M. Menghini, E. Miranda, C. Ricciardi, S. Tappertzhofen, K. Terabe, I. Valov, Quantum conductance in memristive devices: fundamentals, developments, and applications, Adv. Mater. 34 (2022) 2201248, https://doi.org/10.1002/adma.202201248.

[20] R. Gao, X. Ye, C. Hu, Z. Zhang, X. Ji, Y. Zhang, X. Meng, H. Yang, X. Zhu, R.W. Li, Nanoionics enabled atomic point contact construction and quantum conductance effects, Mater. Horiz. 12 (2025) 37–63, https://doi.org/10.1039/d4mh00916a.

[21] K. Terabe, T. Hasegawa, T. Nakayama, M. Aono, Quantum point contact switch realized by solid electrochemical reaction, RIKEN Rev. 37 (2001) 7. https://www.researchgate.net/publication/266452330.

[22] K. Terabe, T. Hasegawa, T. Nakayama, M. Aono, Quantized conductance atomic switch, Nature 433 (2005) 47–50, https://doi.org/10.1038/nature03190.

[23] T. Sakamoto, S.S. Wong, Y.Y. Liauw, Switch application in FPGA, in: D. Ielmini, R. Waser (Eds.), Resistive Switching: From Fundamental of Nanoionic Redox Process to Memristice Device Application, Wiley-VCH, Weinheim, Germany, 2016, pp. 695–713, https://doi.org/10.1002/9783527680870.ch24.

[24] N. Banno, M. Tada, T. Sakamoto, K. Okamoto, M. Miyamura, N. Iguchi, H. Hada, Improved switching voltage variation of cu atom switch for nonvolatile programmable logic, IEEE Trans. Electron Devices 61 (2014) 3827–3832, https://doi.org/10.1109/TED.2014.2355830.

[25] R. Nebashi, N. Banno, M. Miyamura, X. Bai, K. Funahashi, K. Okamoto, N. Iguchi, H. Numata, T. Sugibayashi, A 171k-LUT nonvolatile FPGA using Cu atom-switch technology in 28nm CMOS, in: Proc. International Conf. on Field-Programmable Logic and Applications, 2020, pp. 323–327, https://doi.org/10.1109/FPL50879.2020.00060.

[26] K. Takeuchi, T. Sakamoto, M. Tada, Single-event effects induced on atom switch-based field-programmable gate Array, IEEE T Trans. Nucl. Sci. 66 (2019) 1355–1360, https://doi.org/10.1109/TNS.2019.2923013.

[27] M. Miyamura, T. Sakamoto, X. Bai, Y. Tsuji, A. Morioka, R. Nebashi, Nanobridge-based FPGA in high-temperature Eenvironments, IEEE Micro 5 (2017) 32–42, https://doi.org/10.1109/MM.2017.3711648.

[28] K. Okamoto, T. Tanaka, M. Miyamura, H. Ishikuro, K. Uchida, T. Sakamoto, M. Tada, Cryogenic operation of NanoBridge at 4 K for controlling qubit, Jpn. J. Appl. Phys. 61 (2022) SC1049, https://doi.org/10.35848/1347-4065/ac4303.

[29] X. Bai, R. Nebashi, M. Miyamura, K. Funahashi, K. Okamoto, H. Numata, N. Iguchi, T. Sakamoto, M. Tada, A 0.11pJ/bit read energy embedded NanoBridge non-volatile memory and its integration in a 28 nm 32 bit RISC-V microcontroller units, Jpn, J. Appl. Phys. 63 (2024) 02SP59, https://doi.org/10.35848/1347-4065/ad1775.

[30] I. Valov, I. Sapezanskaia, A. Nayak, T. Tsuruoka, T. Bredow, T. Hasegawa, G. Staikov, M. Aono, R. Waser, Atomically controlled electrochemical nucleation at superionic solid electrolyte surfaces, Nature Mater. 11 (2012) 530–535, https://doi.org/10.1038/NMAT3307.

[31] E. Budevski, G. Staikov, W.J. Lorenz, Electrochemical Phase Formation and Growth, VCH, Wheinhein, 1996.

[32] T. Tsuruoka, T. Hasegawa, K. Terabe, M. Aono, Operating mechanism and resistive switching characteristics of two- and three-terminal atomic switches using thin oxide layers, J. Electroceram. 39 (2017) 143–156, https://doi.org/10.1007/S10832-016-0063-9.

[33] T. Tsuruoka, T. Hasegawa, K. Terabe, M. Aono, Conductance quantization and synaptic behavior in a Ta_2O_5-based atomic switch, Nanotechnology 23 (2012) 435705. https://stacks.iop.org/Nano/23/435705.

[34] V.K. Sahu, P. Misra, A.K. Das, R.S. Ajimsha, B. Singh, Quantized conductance in Ta_2O_5 based resistive random access memory devices, AIP Conf. Proc. 1832 (2017) 120026, https://doi.org/10.1063/1.4980711.

[35] X. Zhu, W. Su, Y. Liu, B. Hu, L. Pan, W. Lu, J. Zhang, R.-W. Li, Observation of conductance quantization in oxide-based resistive switching memory, Adv. Mater. 24 (2012) 3941–3946, https://doi.org/10.1002/adma.201201506.

[36] F.G. Aga, J. Woo, J. Song, J. Park, S. Lim, C. Sung, H. Hwang, Controllable quantized conductance for multilevel data storage applications using conductive bridge random access memory, Nanotechnology 28 (2017) 115707, https://doi.org/10.1088/1361-6528/aa5baf.

[37] W. Banerjee, H. Hwang, Quantized conductance device with 6-bit storage based on electrically controllable break junctions, Adv. Electron. Mater. 5 (2019) 1900744, https://doi.org/10.1002/aelm.201900744.

[38] S.R. Nandakumar, M. Minvieelle, S. Nagar, C. Dubourdieu, B. Rajendran, A 250 mV cu/SiO_2/W memristor with half-integer quantum conductance states, Nano Lett. 16 (2016) 1602–1608, https://doi.org/10.1021/acs.nanolett.5b04296.

[39] J.R. Jameson, N. Gilbert, F. Koushan, J. Saenz, J. Wang, S. Hollmer, Quantized conductance in Ag/GeS_2/W conductive-bridge memory cells, IEEE Electron Device Lett. 33 (2021) 257–259, https://doi.org/10.1109/LED.2011.2177803.

[40] S. Tappertzhofen, I. Valov, R. Waser, Quantum conductance and switching kinetics of AgI-based microcrossbar cells, Nanotechnology 23 (2012) 145703, https://doi.org/10.1088/0957-4484/23/14/145703.

[41] L. Jiang, L. Xu, J.W. Chen, P. Yan, K.H. Xue, H.J. Sun, X.S. Miao, Conductance quantization in an AgInSbTe-based memristor at nanosecond scale, Appl. Phys. Lett. 109 (2016) 153506, https://doi.org/10.1063/1.4963263.

[42] T. Tsuruoka, K. Terabe, Solid polymer electrolyte-based atomic switches: from materials to mechanisms and applications, Sci. Technol. Adv. Mater. 25 (2024) 2342772, https://doi.org/10.1080/14686996.2024.2342772.

[43] S. Gao, F. Zeng, C. Chen, G. Tang, Y. Lin, Z. Zheng, C. Song, F. Pan, Conductance quantization in a Ag filament-based polymer resistive memory, Nanotechnology 24 (2013) 335201, https://doi.org/10.1088/0957-4484/24/33/335201.

[44] B.C. Jang, S. Kim, S.Y. Yang, J. Park, J.-H. Cha, J. Oh, J. Choi, S.G. Im, V. P. Dravid, S.-Y. Choi, Polymer analog memristive synapse with atomic-scale conductive filament for flexible neuromorphic computing system, Nano Lett. 19 (2019) 839–849, https://doi.org/10.1021/acs.nanolett.8b04023.

[45] K. Krishnan, S. Vijayaraghavan, Unraveling the atomic redox process in quantum conductance and synaptic events for neuromorphic computing, Adv. Electron. Mater. 8 (2022) 2200509, https://doi.org/10.1002/aelm.202200509a.

[46] R. Higuchi, S. Lilak, H.O. Sillin, T. Tsuruoka, M. Kunitake, T. Nakayama, J. K. Gimzewski, A.Z. Stieg, Metal doped polyaniline as neuromorphic circuit elements for in-materia computing, Sci. Technol. Adv. Mater. 24 (2023) 2178815, https://doi.org/10.1080/14686996.2023.2178815.

[47] S. Mallik, P.P. Samal, A. Mahapatra, I. Pradhan, M. Ansari, N. Das, P. Mishra, T. Tsuruoka, K. Terabe, A. Nayak, Quantized conductance behaviour observed in an atomic switch using triptycene-based polymers, J. Mater. Chem. C 10 (2022) 13225, https://doi.org/10.1039/d2tc00771a.

[48] K. Krishnan, M. Muruganathan, T. Tsuruoka, H. Mizuta, M. Aono, Highly reproducible and regulated conductance quantization in a polymer-based atomic switch, Adv. Funct. Mater. 27 (2017) 1605104, https://doi.org/10.1002/adfm.201605104.

[49] K. Krishnan, M. Aono, T. Tsuruoka, Kinetic factors determining conducting filament formation in solid polymer electrolyte based planar devices, Nanoscale 8 (2016) 13976, https://doi.org/10.1039/C6NR00569A.

[50] T. Hasegawa, T. Ohno, K. Terabe, T. Tsuruoka, T. Nakayama, J.K. Gimzewski, M. Aono, Learning abilities achieved by a single solid-state atomic switch, Adv. Mater. 22 (2010) 1831–1834, https://doi.org/10.1002/adma.200903680.

[51] S.H. Jo, T. Chang, I. Ebong, B.B. Bhadviya, P. Mazumder, W. Lu, Nanoscale memristor device as synapse in neuromorphic systems, Nano Lett. 10 (2010) 1297–1301, https://doi.org/10.1021/nl904092h.

[52] T. Ohno, T. Hasegawa, T. Tsuruoka, K. Terabe, J.K. Gimzewski, M. Aono, Short-term plasticity and long-term potentiation mimicked in single inorganic synapses, Nat. Mater. 10 (2011) 591–595, https://doi.org/10.1038/nmat3054.

[53] Y. Coo, H. Fu, X. Fan, X. Tian, Z. Zhao, J. Lu, Z. Liang, B. Xu, Advanced design of high performance artificial neuromorphic electronics, Mater. Today 80 (2024) 648–680, https://doi.org/10.1016/j.mattod.2024.08.027.

[54] D. Markovic, A. Mizrahi, D. Querlioz, J. Grollier, Physics for neuromorphic computing, nature, Rev. Phys. 2 (2020) 499–510, https://doi.org/10.1038/s42254-020-0208-2.

[55] G. Indiveri, A VLSI array of low-power spiking neurons and bistable synapse with spike-timing dependent plasticity, IEEE Trans. Neural Netw. 17 (2006) 211–221, https://doi.org/10.1109/TNN.2005.860850.

[56] E.J. Fuller, F.E. Gabaly, F. Léonard, S. Agarwal, S.J. Plimpton, R.B. Jacobs-Gedrim, C.D. James, M.J. Marinella, A.A. Talin, Li-ion synaptic transistor for low power analog computing, Adv. Mater. 29 (2017) 1604310, https://doi.org/10.1002/adma.201604310.

[57] F. Yu, L.Q. Zhu, H. Xiao, W.T. Gao, Y.B. Guo, Restickable oxide neuromorphic transistors with spike-timing-dependent plasticity and Pavlovian associative learning activities, Adv. Funct. Mater. 28 (2018) 1804025, https://doi.org/10.1002/adfm.201804025.

[58] J. Zhou, Y. Liu, Y. Shi, Q. Wan, Solution-processed chitosan-gated IZO-based transistors for mimicking synaptic plasticity, IEEE Electron Device Lett. 35 (2014) 280–282, https://doi.org/10.1109/LED.2013.2295815.

[59] X. Yao, K. Klyukin, W. Lu, M. Onen, S. Ryu, D. Kim, N. Emond, I. Waluyo, A. Hunt, J.A. del Alamo, J. Li, B. Yildiz, Protonic solid-state electrochemical synapse for physical neural networks, Nat. Commun. 11 (2020) 3134, https://doi.org/10.1038/s41467-020-16866-6.

[60] Y. van de Burgt, E. Lubberman, E.J. Fuller, S.T. Keene, G.C. Faria, S. Agarwal, M. J. Marinella, A.A. Talin, A.A. Salleo, A non-volatile organic electrochemical device as a low-voltage artificial synapse for neuromorphic computing, Nature Mater. 16 (2017) 414–418, https://doi.org/10.1038/nmat4856.

[61] T. Tsuchiya, M. Jayavel, K. Kawamura, M. Takayanagi, T. Higuchi, R. Jayavel, K. Terabe, Neuromorphic transistor achieved by redox reaction of WO_3 thin film, Jpn. J. Appl. Phys. 57 (2018) 04FK01, https://doi.org/10.7567/JJAP.57.04FK01.

[62] Z.Y. Ren, L.Q. Zhu, L. Ai, X.Q. Lou, J.C. Cai, Z.Y. Li, H. Xiao, Aqueous solution processed mesoporous silica-gated photo-perception neuromorphic transistor, J. Mater. Sci. 56 (2021) 4316–4327, https://doi.org/10.1007/s10853-020-05560-z.

[63] H.N. Mohanty, T. Tsuruoka, J.R. Mohanty, K. Terabe, Proton-gated synaptic transistors, based on an electron-beam patterned Nafion electrolytes, ACS Appl. Mater. Interfaces 15 (2023) 19279–19289, https://doi.org/10.1021/acsami.3c00756.

[64] J.G. Gluschke, J. Seidl, R.W. Lyttleton, K. Nguyen, M. Lagier, F. Meyer, P. Krogstrup, J. Nygård, S. Lehmann, A.B. Mostert, P. Meredith, A.P. Micolich, Integrated bioelectronic proton-gated logic elements utilizing nanoscale patterned Nafion, Mater. Horiz. 8 (2021) 224–233, https://doi.org/10.1039/D0MH01070G.

[65] R.D. Nikam, M. Kwak, J. Lee, K.G. Rajput, H. Hwang, Controlled ionic tunneling in lithium nanoionic synaptic transistor through atomically thin graphene layer for neuromorphic computing, Adv. Electron. Mater. 6 (2020) 1901100, https://doi.org/10.1002/aelm.201901100.

[66] K. Lee, M. Kwak, W. Choi, C. Lee, J. Lee, S. Noh, J. Lee, H. Lee, H. Hwang, Improved synaptic functionalities of Li-based nano-ionic synaptic transistor with ultralow conductance enabled by Al_2O_3 barrier layer, Nanotechnology 32 (2021) 275201, https://doi.org/10.1088/1361-6528/abf071.

[67] R.D. Nikam, M. Kwak, J. Lee, K.G. Rajput, W. Banerjee, H. Hwang, Near ideal synaptic functionalities in Li ion synaptic transistor using $Li_3PO_xSe_x$ electrolyte with high ionic conductivity, Sci. Rep. 9 (2019) 18883, https://doi.org/10.1038/s41598-019-55310-8.

[68] B. Park, Y. Hwang, O. Kwon, S. Hwang, J.A. Lee, D.-H. Choi, S.-K. Lee, A.R. Kim, B. Cho, J.-D. Kwon, J.I. Lee, Y. Kim, Robust 2D MoS_2 artificial synapse device based on a lithium silicate solid electrolyte for high-precision analogue neuromorphic computing, ACS Appl. Mater. Interfaces 14 (2022) 53038–53047, https://doi.org/10.1021/acsami.2c14080.

[69] J.G. Kim, B. Son, S. Mukherjee, N. Schuppert, A. Bates, O. Kwon, M.J. Choi, H. Y. Chung, S. Park, A review of lithium and non-lithium based solid state batteries, J. Power Sources 282 (2015) 299–322, https://doi.org/10.1016/j.jpowsour.2015.02.054.

[70] H. Tsukamoto, A. West, Electronic conductivity of $LiCoO_2$ and its enhancement by magnesium doping, J. Electrochem. Soc. 144 (1997) 3164–3168, https://doi.org/10.1149/1.1837976.

[71] S. Mallik, T. Tsuruoka, T. Tsuchiya, K. Terabe, Effects of Mg doping to a $LiCoO_2$ channel on the synaptic plasticity of Li ion-gated transistors, ACS Appl. Mater. Interfaces 15 (2023) 47184–47195, https://doi.org/10.1021/acsami.3c07833.

[72] P.Y. Chen, X. Peng, S. Yu, NeuroSim+: An integrated device-to-algorithm framework for benchmarking synaptic devices and array architectures, in: IEEE International Electron Device Meeting (IEDM), 2017, pp. 135–138, https://doi.org/10.1109/IEDM.2017.8268337.

[73] L. Appeltant, M.C. Soriano, G. Van der Sande, J. Danckaert, S. Massar, J. Dambre, B. Schrauwen, C.R. Mirasso, I. Fischer, Information processing using a single dynamical node as complex system, Nat. Commun. 2 (2011) 468, https://doi.org/10.1038/ncomms1476.

[74] K. Nakajima, Physical reservoir computing – an introductory perspective, Jpn. J. Appl. Phys. 59 (2020) 060501, https://doi.org/10.35848/1347-4065/ab8d4f.

[75] S. Kan, K. Nakajima, T. Asai, M. Akai-Kasaya, Physical implementation of reservoir computing through electrochemical reaction, Adv. Sci. 9 (2022) 2104076, https://doi.org/10.1002/advs.202104076.

[76] G. Tanaka, T. Yamane, J.B. Heroux, R. Nakane, N. Kanazawa, S. Takeda, H. Numata, D. Nakano, A. Hirose, Neural Netw. 115 (2019) 100–123, https://doi.org/10.1016/j.neunet.2019.03.005.

[77] S.-G. Koh, H. Shima, Y. Naitoh, H. Akinaga, K. Kinoshita, Reservoir computing with dielectric relaxation at an electrode–ionic liquid interface, Sci. Rep. 12 (2022) 6958, https://doi.org/10.1038/s41598-022-10152-9.

[78] T. Matsuo, D. Sato, S.-G. Koh, H. Shima, Y. Naitoh, H. Akinaga, T. Itoh, T. Nokami, M. Kobayashi, K. Kinoshita, Dynamic nonlinear behavior of ionic liquid-based reservoir computing devices, ACS Appl. Mater. Interfaces 14 (2022) 36890, https://doi.org/10.1021/acsami.2c04167.

[79] M. Nakajima, K. Minegishi, Y. Shimizu, Y. Usami, H. Tanaka, T. Hasegawa, In-materio reservoir working at low frequencies in a Ag_2S-island network, Nanoscale 14 (2022) 7634, https://doi.org/10.1039/D2NR01439D.

[80] A.V. Avizienis, H.O. Sillin, C. Martin-Olmos, H.-H. Shieh, M. Aono, A.Z. Stieg, J. K. Gimzewski, Neuromorphic atomic switch network, PloS One 7 (2012) e42772, https://doi.org/10.1371/journal.pone.0042772.

[81] H.O. Sillin, R. Aguilera, H.-H. Shieh, A.V. Avizienis, M. Aono, A.Z. Stieg, J. K. Gimzewski, A theoretical and experimental study of neuromorphic atomic switch networks for reservoir computing, Nanotechnology 24 (2013) 384004, https://doi.org/10.1088/0957-4484/24/38/384004.

[82] M. Hadiyawarman, H. Eguchi, Tanaka, control of the neuromorphic learning behavior based on the aggregation of thiol-protected ag-Ag_2S core–shell nanoparticles, Jpn. J. Appl. Phys. 59 (2020) 015001, https://doi.org/10.7567/1347-4065/ab5c77.

[83] Y. Hadiyawarman, T. Usami, S. Kotooka, M. Azhari, H. Eguchi, Performance of Ag–Ag_2S core–shell nanoparticle-based random network reservoir computing device, Jpn. J. Appl. Phys. 60 (2021), https://doi.org/10.35848/1347-4065/abe206. SCCF02.

[84] O. Srikimkaew, D. Banerjee, S. Azhari, Y. Usami, H. Tanaka, High performance of an in-material reservoir computing device achieved by complex dynamics in a nanoparticle random network Memristor, ACS Appl. Electron. Mater. 6 (2023) 688–695, https://doi.org/10.1021/acsaelm.3c01046.

[85] A. Nayak, S. Unayama, S. Tai, T. Tsuruoka, R. Waser, M. Aono, I. Valov, T. Hasegawa, Nanoarchitectonics for controlling the number of dopant atoms in solid electrolyte nanodots, Adv. Mater. 30 (2018) 1703261, https://doi.org/10.1002/adma.201703261.

[86] K. Minegishi, Y. Shimizu, T. Hasegawa, Pulse width dependent operations of a Ag_2S island network reservoir, Jpn. J. Appl. Phys. 62 (2023), https://doi.org/10.35848/1347-4065/acb8c0. SG1032.

[87] K. Yoshimura, T. Hasegawa, Research on tactile sensation by physical reservoir computing with a robot arm and a Ag_2S reservoir, Jpn. J. Appl. Phys. 63 (2024) 03SP17, https://doi.org/10.35848/1347-4065/ad21bc.

[88] M. Hayakawa, T. Hasegawa, Development of a physical reservoir that operates by the diffusion of cu cations, Jpn. J. Appl. Phys. 63 (2024) 04SP29, https://doi.org/10.35848/1347-4065/ad2fdd.

[89] T. Hasegawa, H. Tanaka, Solid electrolyte-based physical reservoir, vacuum and surface, Science 67 (2024) 521–526, https://doi.org/10.1380/vss.67.521.

[90] M. Hayakawa, H. Tanaka, T. Hasegawa, In-sensor computing using a cu-doped Ta_2O_5 reservoir for optical pattern classification, Jpn. J. Appl. Phys. 64 (2025) 03SP21, https://doi.org/10.35848/1347-4065/adb6ae.

[91] Y. Shimizu, K. Minegishi, H. Tanaka, T. Hasegawa, Ag_2S island network reservoir that works with direct optical signal inputs, Jpn. J. Appl. Phys. 62 (2023), https://doi.org/10.35848/1347-4065/acab0a. SG1001.

[92] Y. Usami, B. van de Ven, D.G. Mathew, T. Chen, T. Kotooka, Y. Kawashima, Y. Tanaka, Y. Otsuka, H. Ohoyama, H. Tamukoh, H. Tanaka, W.G. van der Wiel, In-Materio reservoir computing in a sulfonated polyaniline network, Adv. Mater. 33 (2021) 2102688, https://doi.org/10.1002/adma.202102688.

[93] D. Banerjee, T. Kotooka, S. Azhari, Y. Usami, T. Ogawa, J.K. Gimzewski, H. Tamukoh, H. Tanaka, Emergence of in-materio intelligence from an incidental structure of a single-walled carbon nanotube–porphyrin polyoxometalate random network, Adv. Intell. Syst. 4 (2022) 2100145, https://doi.org/10.1002/aisy.202100145.

[94] K. Kimizuka, S. Azhari, S. Tokuno, A. Karacali, Y. Usami, S. Ikemoto, H. Tamukoh, H. Tanaka, Haptic in-sensor computing device based on CNT/PDMS nanocomposite physical reservoir, Adv. Intell. Sys. 7 (2025) 2400640, https://doi.org/10.1002/aisy.202400640.

[95] R. Matsuo, T. Hasegawa, Classification of direct optical signal inputs by Ag_2S island network reservoir, Jpn. J. Appl. Phys. 63 (2024) 03SP61, https://doi.org/10.35848/1347-4065/ad21bb.

[96] C. Sugiura, M. Kitamura, S. Muramatsu, S. Shoji, S. Kojima, Y. Tada, I. Umezu, T. Arai, Sulfur-k x-ray spectra and electronic structure of a semiconductor Ag_2S, Jpn. J. Appl. Phys. 27 (1988) 1216–1219, https://doi.org/10.1143/JJAP.27.1216.

[97] H. Roshan, F. Ravanan, M.H. Sheikhi, A. Mirzaei, High-detectivity near-infrared photodetector based on Ag_2S nanocrystals, J. Alloys Compd. 852 (2021) 156948, https://doi.org/10.1016/j.jallcom.2020.156948.

[98] Y. Ohno, H. Tanaka, T. Hasegawa, Recognition of optical patterns directly irradiated to a three-dimensional silver sulfide physical reservoir, Jpn. J. Appl. Phys. 64 (2025) 03SP15, https://doi.org/10.35848/1347-4065/adb759.

[99] D. Nishioka, T. Tsuchiya, W. Namiki, M. Takayanagi, M. Imura, Y. Koide, T. Higuchi, K. Terabe, Edge-of-chaos learning achieved by ion-electron–coupled dynamics in an ion-gating reservoir, Sci. Adv. 8 (2022) eade1156, https://doi.org/10.1126/sciadv.ade1156.

[100] M. Inubushi, K. Yoshimura, Reservoir computing beyond memory-nonlinearity trade-off, Sci. Rep. 7 (2017) 10199, https://doi.org/10.1038/s41598-017-10257-6.

[101] J. Hochstetter, R. Zhu, A. Loeffler, A. Diaz-Alvarez, T. Nakayama, Z. Kuncic, Avalanches and edge-of-chaos learning in neuromorphic nanowire networks, Nat. Commun. 12 (2021) 4008, https://doi.org/10.1038/s41467-021-24260-z.

[102] M. Takayanagi, D. Nishioka, T. Tsuchiya, M. Imura, Y. Koide, T. Higuchi, K. Terabe, Ultrafast-switching of an all-solid-state electric double layer transistor with a porous yttria-stabilized zirconia proton conductor and the application to neuromorphic computing, Mater. Today Adv. 18 (2023) 100393, https://doi.org/10.1016/j.mtadv.2023.100393.

[103] Y. Yang, H. Cui, S. Ke, M. Pei, K. Shi, C. Wan, Q. Wan, Reservoir computing based on electric-double-layer coupled InGaZnO artificial synapse, Appl. Phys. Lett. 122 (2023) 043508, https://doi.org/10.1063/5.0137647.

[104] D. Nishioka, T. Tsuchiya, M. Imura, Y. Koide, T. Higuchi, K. Terabe, A high-performance deep reservoir computer experimentally demonstrated with ion-gating reservoirs, Com. Eng. 3 (2024) 81, https://doi.org/10.1038/s44172-024-00227-y.

[105] Y. Yamaguchi, D. Nishioka, W. Namiki, T. Tsuchiya, M. Imura, Y. Koide, T. Higuchi, K. Terabe, Inverted input method for computing performance enhancement of the ion-gating reservoir, Appl. Phys. Exp. 17 (2024) 024501, https://doi.org/10.35848/1882-0786/ad2906.

[106] H. Kitano, D. Nishioka, K. Terabe, T. Tsuchiya, Physical reservoir computing with graphene-based solid electric double layer transistor and the information processing capacity analysis, Appl. Phys. Exp. 18 (2025) 024501, https://doi.org/10.35848/1882-0786/adb19b.

[107] R. Fang, S. Wang, W. Zhang, K. Ren, W. Sun, F. Wang, J. Lai, P. Zhang, X. Xu, Q. Luo, L. Li, Z. Wang, D. Shang, Oxide-based electrolyte-gated transistors with stable and tunable relaxation responses for deep time-delayed reservoir computing, Adv. Electron. Mater. 10 (2024) 2300652, https://doi.org/10.1002/aelm.202300652.

[108] T. Wada, D. Nishioka, W. Namiki, T. Tsuchiya, T. Higuchi, K. Terabe, A redox-based ion-gating reservoir, utilizing double reservoir states in drain and gate nonlinear responses, Adv. Intel. Sys. 5 (2023) 2300123, https://doi.org/10.1002/aisy.202300123.

[109] E.J. Fuller, et al., Li-ion synaptic transistor for low power analog computing, Adv. Mater. 29 (2017) 1604310, https://doi.org/10.1002/adma.201604310.

[110] K. Shibata, D. Nishioka, W. Namiki, T. Tsuchiya, T. Higuchi, K. Terabe, Redox-based ion-gating reservoir consisting of (104) oriented $LiCoO_2$ film, assisted by physical masking, Sci. Rep. 13 (2023) 21060, https://doi.org/10.1038/s41598-023-48135-z.

[111] L. Appeltant, G. Van der Sande, J. Danckaert, I. Fischer, Constructing optimized binary masks for reservoir computing with delay systems, Sci. Rep. 4 (2014) 3629, https://doi.org/10.1038/srep03629.

[112] T. Tsuchiya, K. Terabe, M. Ochi, T. Higuchi, M. Osada, Y. Yamashita, S. Ueda, M. Aono, In situ tuning of magnetization and magnetoresistance in Fe_3O_4 thin film achieved with all-solid-state redox device, ACS Nano 10 (2016) 1655–1661, https://doi.org/10.1021/acsnano.5b07374.

[113] W. Namiki, T. Tsuchiya, M. Takayanagi, T. Higuchi, K. Terabe, Room-temperature manipulation of magnetization angle achieved with an all-solid-state redox device, ACS Nano 14 (2020) 16065–16072, https://doi.org/10.1021/acsnano.0c07906.

[114] W. Namiki, D. Nishioka, T. Tsuchiya, T. Higuchi, K. Terabe, Magnetization vector rotation reservoir computing operated by redox mechanism, Nano Lett. 24 (2024) 4383–4392, https://doi.org/10.1021/acs.nanolett.3c05029.

[115] T. Shingu, H. Uchiyama, T. Watanabe, Y. Ohno, Electrochemical reservoir computing based on surface-functionalized carbon nanotubes, Carbon 214 (2023) 118344, https://doi.org/10.1016/j.carbon.2023.118344.

[116] W. Namiki, D. Nishioka, Y. Nomura, T. Tsuchiya, K. Yamamoto, K. Terabe, Iono–magnonic reservoir computing with chaotic spin wave interference manipulated by ion-gating, Adv. Sci. 12 (2025) 2411777, https://doi.org/10.1002/advs.202411777.

[117] D. Nishioka, Y. Shingaya, T. Tsuchiya, T. Higuchi, K. Terabe, Few- and single-molecule reservoir computing experimentally demonstrated with surface-enhanced Raman scattering and ion gating, Sci. Adv. 10 (2024) eadk6438, https://doi.org/10.1126/sciadv.adk6438.

[118] T. Tsuchiya, D. Nishioka, W. Namiki, K. Terabe, Physical reservoir computing utilizing ion-gating transistors operating in electric double layer and redox mechanisms, Adv. Electro. Mater. 10 (2024) 2400625, https://doi.org/10.1002/aelm.202400625.

[119] T. Tsuchiya, M. Takayanagi, D. Nishioka, W. Namiki, K. Terabe, Electric double layer effect in the vicinity of solid electrolyte/diamond interfaces and the application to neuromorphic computing, J. Solid State Electrochem. 28 (2024) 4367–4376, https://doi.org/10.1007/s10008-024-05937-z.

[120] S.W. Kuffler, Discharge patterns and functional organization of mammalian retina, J. Neurophysiol. 16 (1953) 37–68, https://doi.org/10.1152/jn.1953.16.1.37.

[121] C. Blakemore, R.H. Carpenter, M.A. Georgeson, Lateral inhibition between orientation detectors in the human visual system, Nature 228 (1970) 37–39, https://doi.org/10.1038/228037a0.

[122] T. Hosoya, S.A. Baccus, M. Meister, Dynamic predictive coding by the retina, Nature 436 (2005) 71–77, https://doi.org/10.1038/nature03689.

[123] X. Wan, T. Tsuruoka, K. Terabe, Neuromorphic system for edge information encoding: emulating retinal center-surround antagonism by Li-ion-mediated highly interactive devices, Nano Lett. 21 (2021) 7938–7945, https://doi.org/10.1021/acs.nanolett.1c01990.

[124] M.C. Morrone, J. Ross, D.C. Burr, R. Owens, Mach bands are phase dependent, Nature 324 (1986) 250–253, https://doi.org/10.1038/324250a0.

[125] C. Mead, M.A. Mahowald, A silicon model of early visual processing, Neural Netw. 1 (1988) 91–97, https://doi.org/10.1016/0893-6080(88)90024-X.

[126] C. Mead, Analog VLSI and Neural Systems, Addison-Wesley, 1989.

[127] T. Tsuchiya, K. Terabe, R. Yang, M. Aono, Nanoionic devices: Interface nanoarchitechtonics for physical property tuning and enhancement, Jpn. J. Appl. Phys. 55 (2016) 1102A4, https://doi.org/10.7567/JJAP.55.1102A4.

[128] T. Tsuchiya, K. Terabe, M. Aono, All-solid-state electric-double-layer transistor based on oxide ion migration in Gd-doped CeO_2on $SrTiO_3$ single crystal, Appl. Phys. Lett. 103 (2013) 073110, https://doi.org/10.1063/1.4818736.

[129] K. Ueno, S. Nakamura, H. Shimotani, A. Ohtomo, N. Kimura, T. Nojima, H. Aoki, Y. Iwasa, M. Kawasaki, Electric-field-induced superconductivity in an insulator, Nature Mater. 7 (2008) 855–858, https://doi.org/10.1038/nmat2298.

[130] Z. Tianshu, P. Hing, H. Huang, J. Kilner, Ionic conductivity in the CeO_2–Gd_2O_3 system (0.05≤Gd/Ce≤0.4) prepared by oxalate coprecipitation, Solid State Ion. 148 (2002) 567–573, https://doi.org/10.1016/S0167-2738(02)00121-2.

[131] T. Tsuchiya, S. Miyoshi, Y. Yamashita, H. Yoshikawa, K. Terabe, K. Kobayashi, S. Yamaguchi, Room temperature redox reaction by oxide ion migration at carbon/Gd-doped CeO_2 heterointerface probed by an *in situ* hard x-ray photoemission and soft x-ray absorption spectroscopies, Sci. Tech. Adv. Mater. 14 (2013) 045001, https://doi.org/10.1088/1468-6996/14/4/045001.

[132] S.H. Choi, C.S. Hwang, H.-W. Lee, J. Kim, Fabrication of Gd_2O_3-doped CeO_2 thin films for single-chamber-type solid oxide fuel cells and their characterization, J. Electrochem. Soc. 156 (2009) B381–B385, https://doi.org/10.1149/1.3056036.

[133] T. Tsuchiya, S. Moriyama, K. Terabe, M. Aono, Modulation of superconducting critical temperature in niobium film by using all-solid-state electric-double-layer transistor, Appl. Phys. Lett. 107 (2015) 013104, https://doi.org/10.1063/1.4926572.

[134] T. Tsuchiya, K. Terabe, M. Aono, In situ and non-volatile bandgap tuning of multilayer graphene oxide in an all-solid-state electric double-layer transistor, Adv. Mater. 26 (2014) 1087–1091, https://doi.org/10.1002/adma.201304770.

[135] M.V. Schlupp, J. Martynczuk, M. Prestat, J. Gauckler, Precursor decomposition, microstructure, and porosity of yttria stabilized zirconia thin films prepared by aerosol-assisted chemical vapor deposition, Adv. Energy Mater. 3 (2013) 375–385, https://doi.org/10.1002/aenm.201200596.

[136] B. Sherrer, M.V.F. Schlupp, D. Stender, J. Martynczuk, J.G. Grolig, H. Ma, P. Kocher, T. Lippert, M. Prestat, L.J. Gauckler, On proton conductivity in porous and dense yttria stabilized zirconia at low temperature, Adv. Funct. Mater. 23 (2013) 1957–1964, https://doi.org/10.1002/adfm.201202020.

[137] M. Takayanagi, T. Tsuchiya, D. Nishioka, T. Higuchi, K. Terabe, Room temperature fabrication of highly proton conductive amorphous zirconia-based thin films achieved through precise nanostructure control, J. Mater. Chem. C 11 (2023) 13311–13323, https://doi.org/10.1039/D3TC02084C.

[138] M. Takayanagi, T. Tsuchiya, K. Kawamura, M. Minohara, K. Horiba, H. Kumigashira, T. Higuchi, Thickness-dependent surface proton conduction in (111) oriented yttria-stabilized zirconia thin film, Solid State Ion. 311 (2017) 46–51, https://doi.org/10.1016/j.ssi.2017.09.003.

[139] T. Tsuchiya, T. Tsuruoka, K. Terabe, M. Aono, In situ and nonvolatile photoluminescence tuning and nanodomain writing demonstrated by all-solid-state devices based on graphene oxide, ACS Nano 9 (2015) 2102–2110, https://doi.org/10.1021/nn507363g.

[140] J. Choi, R. Pradheesh, H. Kim, H. Im, Y. Chong, D.-H. Chae, Electrical modulation of superconducting critical temperature in liquid-gated thin niobium films, Appl. Phys. Lett. 105 (2014) 012601, https://doi.org/10.1063/1.4890085.

[141] T. Tsuchiya, T. Tsuruoka, S.J. Kim, K. Terabe, M. Aono, Ionic decision-maker created as novel, solid-state devices, Sci. Adv. 4 (2018) eaau2057, https://doi.org/10.1126/sciadv.aau2057.

[142] S. Kim, T. Tsuruoka, T. Hasegawa, M. Aono, K. Terabe, M. Aono, Decision maker based on atomic switches, AIMS Mater. Sci. 3 (2016) 245–259, https://doi.org/10.3934/matersci.2016.1.245.

[143] C. Lutz, T. Hasegawa, T. Chikyow, Ag_2S atomic switch-based 'tug of war' for decision making, Nanoscale 8 (2016) 14031–14036, https://doi.org/10.1039/C6NR00690F.

[144] C. Lutz, T. Hasegawa, T. Tsuchiya, C. Adelsberger, R. Hayakawa, T. Chikyow, P-type polymer-based Ag_2S atomic switch for "tug of war" operation, Jpn. J. Appl. Phys. 56 (2017) 06GF03, https://doi.org/10.7567/JJAP.56.06GF03.

[145] Y. Kitagawa, T. Tsuchiya, D. Etoh, M. Takayanagi, W. Namiki, T. Higuchi, K. Terabe, A graphene oxide-based ionic decision-maker for simple fabrication and stable operation, Jpn. J. Appl. Phys. 59 (2020), https://doi.org/10.35848/1347-4065/ab740e. SIIG03.

[146] D. Etoh, T. Tsuchiya, Y. Kitagawa, M. Takayanagi, Y. Itoh, T. Tsuruoka, T. Higuchi, K. Terabe, A mesoporous SiO_2 thin films-based ionic decision-maker for solving multi-armed bandit problems, Jpn. J. Appl. Phys. 59 (2020), https://doi.org/10.35848/1347-4065/ab7437. SIIG01.

[147] C.R. Mariappan, T.P. Heins, B. Roling, Electrode polarization in glassy electrolytes: large interfacial capacitance values and indication for pseudocapacitive charge storage, Solid State Ion. 181 (2010) 859–863, https://doi.org/10.1016/j.ssi.2010.05.011.

[148] J. Kruempelmann, C.R. Mariappan, C. Schober, B. Roling, Electrochemical double layers at the interface between glassy electrolytes and platinum: differentiating between the anode and the cathode capacitance, Phys. Rev. B 82 (2010) 224203, https://doi.org/10.1103/PhysRevB.82.224203.

[149] B. Skinner, M.S. Loth, B.I. Shklovski, Capacitance of the double layer formed at the metal/ionic-conductor interface: how large can it be? Phys. Rev. Lett. 104 (2010) 128302 https://doi.org/10.1103/PhysRevLett.104.128302.

[150] T. Tsuruoka, J. Su, K. Terabe, A voltage-controlled oscillator using variable capacitors with a thin dielectric film, ACS Appl. Electron. Mater. 2 (2020) 2788–2797, https://doi.org/10.1021/acsaelm.0c00481.

[151] L. Han, C.-T. Hsieh, B.C. Mallick, J. Li, Y.A. Gandomi, Recent progress and future prospects of atomic layer deposition to prepare/modify solid-state electrolytes and interfaces between electrodes for next-generation lithium batteries, Nanoscale Adv. 3 (2021) 2728–2740, https://doi.org/10.1039/d0na01072c.

[152] A.C. Kozen, A.J. Pearse, C.-F. Lin, M. Noked, G.W. Rubloff, Atomic layer deposition of the solid electrolyte LiPON, Chem. Mater. 27 (2015) 5324–5331, https://doi.org/10.1021/acs.chemmater.5b01654.

[153] M. Nisula, Y. Shindo, H. Koga, M. Karppinen, Atomic layer deposition of lithium phosphorus oxynitride, Chem. Mater. 27 (2015) 6987–6993, https://doi.org/10.1021/acs.chemmater.5b02199.

[154] S. Shibata, Thermal atomic layer deposition of lithium phosphorus oxynitride as thin-film solid electrolyte, J. Electrochem. Soc. 163 (2016) A2555–A2562, https://doi.org/10.1149/2.0371613jes.

[155] T. Tsuruoka, S. Mallik, T. Tsujita, Y. Inatomi, K. Terabe, Effects of plasma reactants on atomic layer deposition of lithium phosphate and lithium phosphorus oxynitride electrolyte films, Chem. Mater. 36 (2024) 6193–6204, https://doi.org/10.1021/acs.chemmater.4c00960.

[156] S. Jacke, J. Song, G. Cherkashinin, L. Dimesso, W. Jaegermann, Investigation of the solid-state electrolyte/cathode LiPON/LiCoO2 interface by photoelectron spectroscopy, Ionics 16 (2010) 769–775, https://doi.org/10.1007/s11581-010-0479-1.

[157] B. Put, M.J. Mees, N. Hornsveld, S. Hollevoet, A. Sepúlveda, P.M. Vereecken, W. M.M. Kessels, M. Creatore, Plasma-assisted ALD of LiPO(N) for solid state batteries, J. Electrochem. Soc. 166 (2019) A1239–A1242, https://doi.org/10.1149/2.1191906jes.

[158] B. Wang, J. Liu, Q. Sun, R. Li, T.K. Sham, X. Sun, Atomic layer deposition of lithium phosphates as solid-state electrolytes for all-solid-state microbatteries, Nanotechnology 25 (2014) 504007, https://doi.org/10.1088/0957-4484/25/50/504007.

[159] J. Su, T. Tsuruoka, T. Tsujita, Y. Nishitani, K. Nakura, K. Terabe, Atomic layer deposition of a magnesium phosphate solid electrolyte, Chem. Mater. 31 (2019) 5566–5575, https://doi.org/10.1021/acs.chemmater.9b01299.

[160] J. Su, T. Tsuruoka, T. Tsujita, Y. Inatomi, K. Terabe, Nitrogen plasma enhanced low temperature atomic layer deposition of magnesium phosphorus oxynitride (MgPON) solid-state electrolytes, Angew. Chem. Int. Ed. 62 (2023) e202217203, https://doi.org/10.1002/anie.202217203.

[161] K. Terabe, T. Tsuchiya, T. Tsuruoka, Solid state ionics for the development of artificial intelligence components, Jpn. J. Appl. Phys. 61 (2022), https://doi.org/10.35848/1347-4065/ac64e5. SM0803.